Charge-breeding studies for high-precision mass measurements on short-lived nuclides at TITAN and a direct determination of the ^{51}Cr electron-capture Q-value for neutrino physics

by

Tegan Danielle Macdonald

B. Sc., The University of Waterloo, 2011

A THESIS SUBMITTED IN PARTIAL FULFILLMENT
OF THE REQUIREMENTS FOR THE DEGREE OF

Master of Science

in

THE FACULTY OF GRADUATE AND POSTDOCTORAL
STUDIES

(Physics)

The University of British Columbia

(Vancouver)

April 2014

Abstract

Penning-trap mass spectrometry (PTMS) is a well-established technique for performing high-precision mass measurements on both stable and short-lived nuclides. Achieving high precisions with radioactive isotopes is technically challenging due to the limited yields and inherent losses from radioactive decay, but it is a worthwhile pursuit as the mass is a fundamental property unique to each nuclide. Accurate and precise knowledge of the mass plays a critical role in the advancement of both theories and applications of nuclear and particle physics. This work provides the result of a Q-value (mass difference) measurement of the ^{51}Cr$(e^-,\nu_e)^{51}$V reaction. This first direct Q-value measurement confirmed the neutrino energies that were used in calculations for the solar neutrino experiments SAGE and GALLEX and the so-called gallium.

Charge breeding to increase the precision of a PTMS measurement on radioactive ions is a technique that is unique to the TITAN (TRIUMF's Ion Trap for Atomic and Nuclear science) facility; however, this potential increase in precision can be diminished by inefficiencies that are introduced by charge breeding. This thesis describes the simulations and systematic studies that are used to quantify the precision gained in a PTMS measurement made with highly charged, radioactive ions. This novel approach has allowed for the identification of key charge-breeding parameters and the determination of the optimal charge-breeding conditions based solely on the nuclide of interest and its half-life. Furthermore, experimental investigations were performed to determine the compatibility between the simulated findings and experimental observations. These investigations have led to a deeper understanding of the charge-breeding process and apparatus and will improve the predictability and performance of charge breeding at TITAN.

Preface

The TITAN collaboration consists of graduate students, postdocs, technical staff, and professors sharing the goal of performing high-precision mass measurements to advance the field of nuclear science. As a result the work is highly collaborative with a number of people at any given time involved with running the experimental apparatus, collecting data, and sharing and interpreting results. The relative contributions to the work included in this thesis are outlined below.

Chapters 1 through 3: The motivation, theory, and experimental setup are entirely written by me and discussed in the context of previous work. Appropriate references to published work appear throughout.

Chapter 4: The charge breeding program CBSIM, as seen in Section 4.1, is a public domain program maintained by R. Becker [Journal of Physics: Conference Series **58**:443 (2007)]. I performed modifications to the program, including the addition of new elements and exporting of the data from Fortran to C++, with assistance from A. T. Gallant and R. Klawitter. I generated all calculations, plots, and interpretation of the results under the supervision of M. C. Simon and J. Dilling. Portions of the discussion in Section 4.2, including Equation 4.10, have appeared in two publications, both of which I coauthored:

- M. C. Simon, T. D. Macdonald, et al., *Charge breeding rare isotopes for high precision mass measurements: challenges and opportunities*, Physica Scripta, **T156**:014098 (2013).

- S. Ettenauer, M. C. Simon, T. D. Macdonald, and J. Dilling, *Advances in*

precision, resolution, and separation techniques with radioactive, highly charged ions for Penning trap mass measurements, International Journal of Mass Spectrometry, **349-350**:74-80 (2013).

Section 4.3 is based on a proposal for a future experiment at TITAN written by S. Ettenauer and myself:

- T. D. Macdonald and S. Ettenauer, *S1445: High precision mass measurements for the determination of ^{74}Rb's Q-value*, TRIUMF-EEC proposal, https://mis.triumf.ca/science/experiment/view/S1445 (2013).

Chapter 5: The experimental data was collected by M .C. Simon, R. Klawitter, and myself. I designed the experiments, performed the analysis, and prepared the results. Discussion and interpretation of the results were prepared with assistance from M. C. Simon and R. Klawitter. The improvements that were made to the apparatus as discussed in Section 5.3.3, were a collaborative effort led by R. Klawitter, who was responsible for realigning the electron collector assembly.

Chapter 6: The collection of the experimental data was taken during shift work by the TITAN collaboration. All members of the collaboration assisted with the preparation of the apparatus and collection of the data. B. E. Schultz and I performed the analysis with assistance from A. T. Gallant and A. A. Kwiatkowski. I wrote the contents of the chapter, and a version of the work has been accepted for publication in Physical Review C :

- T. D. Macdonald, B. E. Schultz, et al., *A precision Penning-trap measurement to investigate the role of the $^{51}Cr(e^-,\nu_e)^{51}V$ Q-value in the gallium anomaly*, Physical Review C, **CK10395** (accepted for publication Apr-2014).

Table of Contents

List of Tables

List of Figures

Glossary

3D   three-dimensional

BNG   Bradbury-Nielsen gate

CBSIM   Charge Breeding SIMulation

CX   charge exchange

EBIT   electron beam ion trap

EBIS/T   electron beam ion source and trap

EEC   Experiments Evaluation Committee

EC   electron-capture

ECRIS   electron-cyclotron resonance ion source

EI   electron impact ionization

FEBIAD   forced electron beam induced arc discharge

FT-ICR   Fourier-transform ion-cyclotron-resonance

GALLEX   Gallium Experiment

HCI   highly charged ions

IG-LIS   ion-guided laser ion source

ISAC   Isotope Separator and ACcelerator

ISOL isotope separation on-line

LEBT low energy beam transport

MCP micro-channel plate

MPET measurement Penning trap

PTMS Penning-trap mass spectrometry

RFQ radio-frequency quadrupole

RF radio-frequency

RIB radioactive ion beam

RILIS resonant ionization laser ion source

RR radiative recombination

SAGE Soviet-American Gallium Experiment

SCI singly charged ions

SI International System of Units

SIS surface ion source

TITAN TRIUMF's Ion Trap for Atomic and Nuclear science

TOF-ICR time-of-flight ion-cyclotron-resonance

TRIUMF Canada's National Laboratory for Particle and Nuclear Physics

Acknowledgments

Chapter 1

Introduction

1.1 Fundamental Science

There are many open questions in the field of nuclear and particle physics that reveal how little is known about the universe. Consider, for example, that ordinary matter consists of only about 4% of the entire mass of the universe, and the other 96% has not been identified; or that the production of elements heavier than iron is still not understood; or that neutrinos, fundamental particles in the Standard Model, have only recently been described as having a mass, yet their mass remains unknown. These are only a few of the greatest unanswered questions in physics [1]. The research dedicated to addressing these and other outstanding questions in physics will greatly impact the future of research in yet unimaginable ways. TRIUMF, Canada's National Laboratory for Particle and Nuclear Physics, has a mission "to make discoveries that address the most compelling questions in particle physics, nuclear physics, nuclear medicine, and materials science" and increase our fundamental understanding of how nature works.

Accelerator facilities [2], like TRIUMF, offer a unique opportunity to study particle interactions, test and refine new theories, and develop new technologies. Access to radioactive ion beams (RIBS) allows experimenters to perform research on short-lived isotopes and fundamental particles under extreme conditions that are otherwise inaccessible. This research is typically performed by creating increasingly exotic nuclides and by improving the precision of critical measurements [3],

as is done at many of the experiments at TRIUMF. The TITAN (TRIUMF's Ion Trap for Atomic and Nuclear science) collaboration [4] contributes to the precision frontier by measuring the masses [5] and nuclear decay branching ratios [6, 7] of exotic nuclides with high precision and accuracy. These precision measurements make subtle and important contributions to our fundamental knowledge of particle interactions.

1.2   Masses and Motivation

High-precision mass measurements reveal a fundamental property of each nuclide [8]. Lighter than the sum of all the constituent masses, the mass of a nuclide represents the net effect of all the interactions within the nuclide, both atomic and nuclear. This value is of critical importance in the study of nuclear and particle physics as it provides insight into the three primary areas of research: nuclear structure, nuclear astrophysics, and fundamental symmetries and interactions. The required precision of a given mass measurement depends on the science case of interest and typically corresponds to a relative mass uncertainty in the range of $\delta m/m \sim 10^{-6} - 10^{-9}$.

Penning-trap mass spectrometry (PTMS) currently sets the standard for accurate and precise mass measurements [9]. Reaching precisions of up to 10^{11} on stable beam [10], the manipulation of ions for PTMS has been well developed, extensively studied, and is fast enough for use with short-lived isotopes. For these reasons, most RIB facilities are coupled to Penning traps across the world, including TITAN at TRIUMF [5], ISOLTRAP at ISOLDE (CERN) [11], LEBIT at NSCL/MSU [12, 13], JFYLTRAP at the University of Jyväskylä [14], SHIPTRAP at GSI [15], and TRIGA-TRAP at the TRIGA Mainz research reactor [16]. These facilities have different RIB production techniques and preparation methods, making a wide range of isotopes accessible and providing a unique research niche for each facility.

The PTMS technique used to determine the mass of an exotic nuclide results in a relative mass precision [17] given by the magnetic field strength $B_\circ$ used in confining the ions, the excitation time T_{RF} of the ions in the Penning trap, the charge state q of the ions, and a statistical factor depending on the number of ions

2

N measured:

$$\frac{\delta m}{m} \propto \frac{m}{q\, e\, B_\circ\, T_{RF}\, \sqrt{N}} \quad .$$ (1.1)

With the magnetic field strength suffering from technical limitations (currently $B_{max} \sim 9.4$ T at LEBIT [13]), and the excitation time limited by the half-life of the isotope of interest, there are few strategies left for increasing the relative mass precision in a given measurement. TITAN is the only Penning trap setup at a RIB facility to take advantage of the potential precision gained by increasing the charge of the ions prior to a mass measurement. This unique ability becomes more important as the isotopes of interest lie closer to the limits of existence as they typically have very short half-lives (< 100 ms) and are increasingly difficult to produce. The TITAN collaboration specializes in the measurement of highly charged, short-lived isotopes with up to part-per-billion precision.

1.3 Charge Breeding for PTMS with Highly Charged, Radioactive Ions

Any additional stage in beam preparation has to be both fast and efficient in order to benefit mass measurements on short-lived nuclides with low production rates. During the process of charge breeding many charge states become populated, reducing the number of ions available for measurement in any single charge state. However, there are two devices designed for increasing the charge state of ions that have been extensively studied and compared for use at accelerator facilities [18]: the electron-cyclotron resonance ion source (ECRIS) and the electron beam ion source and trap (EBIS/T). These comparisons have shown that EBIS/Ts produce narrower charge-state distributions, are better at accepting low-intensity beams, and have lower amounts of contamination from charge-bred residual gas. For these reasons, the TITAN collaboration has built and commissioned an electron beam ion trap (EBIT) [19, 20] for their mass measurement program. Optimization of this device addresses questions like which charge state to use, how long the charge-breeding process will take, and whether or not the losses due to radioactive decay and efficiencies are worth the precision gained by increasing the charge state for the mass measurement.

Successful measurements on charge-bred RIB have already been made at TITAN. For example, in the study of fundamental interactions, ^{74}Rb was measured in the 8+ charge state and a relative mass precision of 81 ppb was obtained in only 22 hours [21]: an improvement over the 53 ppb measured at ISOLTRAP in three combined measurement campaigns [22–24]. In nuclear astrophysics, extreme environments like neutron star mergers or core-collapsed supernovae result in the production of exotic nuclides that are difficult, if not impossible, to produce at existing RIB facilities. However, the masses of these nuclides are critical for calculations that will help explain the production of elements heavier that iron, and researchers often have to rely on extrapolated mass values. Results from an experiment on neutron rich rubidium isotopes [25] provided accurate mass values which differed from previous measurements by up to 11σ. These results also allowed for additional extrapolated mass values for more exotic nuclides. Most recently, a mass measurement [26] on charge-bred isotopes for neutrino physics studies was able to rule out a potential cause of a calibration discrepancy in the long-standing gallium anomaly [27], and is discussed as a part of this thesis work. Investigations into the efficiency of charge breeding and developing a systematic way to determine how to balance a reduced excitation time and efficiency with an increased charge state will impact and benefit future mass measurements at TITAN.

1.4   Outline of the Thesis

The research described in this thesis investigates how to improve the precision of Penning-trap mass measurements through charge breeding, in particular for nuclides with short half-lives that lie at the limits of the nuclear chart. The need for precision mass measurements and the motivation for charge breeding are presented in Chapter 1, with an emphasis on the importance of charge breeding as the isotopes of interest become increasingly exotic. Chapter 2 provides a background on ion manipulation, Penning traps, and ion processes in an EBIT. The TITAN experimental setup is described in Chapter 3.

The detailed studies unique to this thesis begin in Chapter 4 with simulations of the charge-breeding process. A numerical algorithm that provides a systematic approach to balancing an increase in charge state with a decrease in efficiency and

excitation time is discussed. Applying the procedure to a proposed part-per-billion mass measurement on ^{74}Rb provides context for the simulations. The assumptions that are made in the simulation are discussed in detail and compared to experimental results in Chapter 5. A complementary chapter on a mass measurement for neutrino physics studies is motivated and presented in Chapter 6. In this chapter, the gallium anomaly is considered in the context of a possible calibration discrepancy at solar neutrino experiments SAGE and GALLEX. The thesis is summarized in Chapter 7, and possible future developments are suggested. The result of the presented research will be used in the planning of future mass measurements at TITAN and will enable measurements on isotopes further from stability and to ever increasing precisions.

Chapter 2

Manipulation and Preparation of Radioactive Ions

The 1989 Nobel Prize in Physics [28] was awarded for the development of the ion-trapping technique, which introduced measurement methods that would be used to test fundamental physics principles and theories [29]. Notably, precision measurements in ion traps have lead to the development of the frequency standard [30] and optical clocks [31], allowed for a precise determination of the electron magnetic moment and an improved measurement of the fine structure constant [32], and most recently, a measurement of the atomic mass of the electron to high precision ($\delta m/m \sim 10^{-11}$) [33].

Most applications of ion trapping rely on three-dimensional (3D) confinement of charged particles. Axial trapping can be achieved by creating a potential well for the charged particles, typically done with a series of three or more electrodes of varying bias. Typical electrode configurations are seen in Figure 2.1. Since it is not possible for electrostatic fields to form a 3D potential minimum (Earnshaw's Theorem) in which the ions can be trapped, radial confinement is achieved using different techniques. Standard techniques and applications of charged particle traps are discussed in this chapter in the context of the TITAN facility. These include the bunching and cooling of radioactive ion beams, Penning-trap mass spectrometry (PTMS), and charge breeding, each of which relies on a different technique for ion confinement.
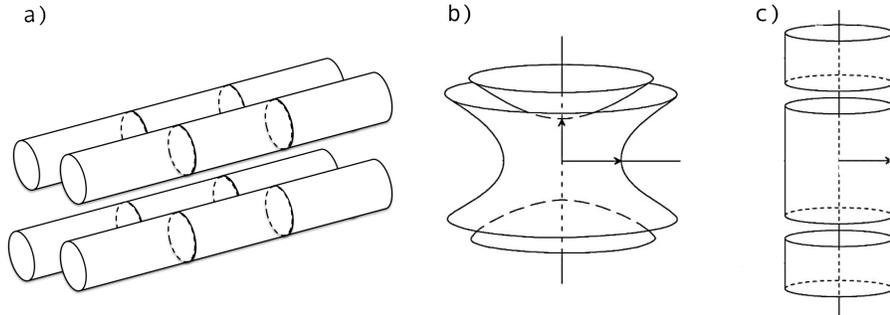
Figure 2.1: Typical ion trap electrode configurations: a) linear trap consisting of four segmented rods; b) hyperbolic trap consisting of two end caps and a ring electrode; and c) cylindrical trap consisting of a series of cylindrical electrodes (drift tubes) (modified figures b) and c) from Ref. [29] ©2010 Taylor & Francis. Reproduced with permission).

2.1 Paul Traps and the Radio-Frequency Quadrupole Trap

A Paul trap [34] uses time-dependent electric fields in the trapping region for 3D ion confinement. In Figure 2.1a), the electrode configuration for a simple linear Paul trap is shown; four rods are segmented into three regions and a potential difference between the end and central electrodes defines the axial trapping region. In this region, an electric quadrupole field is created by applying opposite polarities to neighbouring rods (Figure 2.2). The resulting field focuses the ions in one direction and defocuses in the other. By switching the bias in the trapping region at a radio-frequency, the sign of the quadrupole field alternates and 3D confinement is achieved. The result is the radio-frequency quadrupole (RFQ) linear Paul trap, which has applications in various fields, including at RIB facilities, as discussed below.

The production mechanism of radioactive ions at RIB facilities is not always suited for precision experiments; the resulting ion beam can have too large of an emmitance and some experiments, including the mass-measurement setup at TITAN, require small bunches of ions and not a continuous ion beam. An addi-
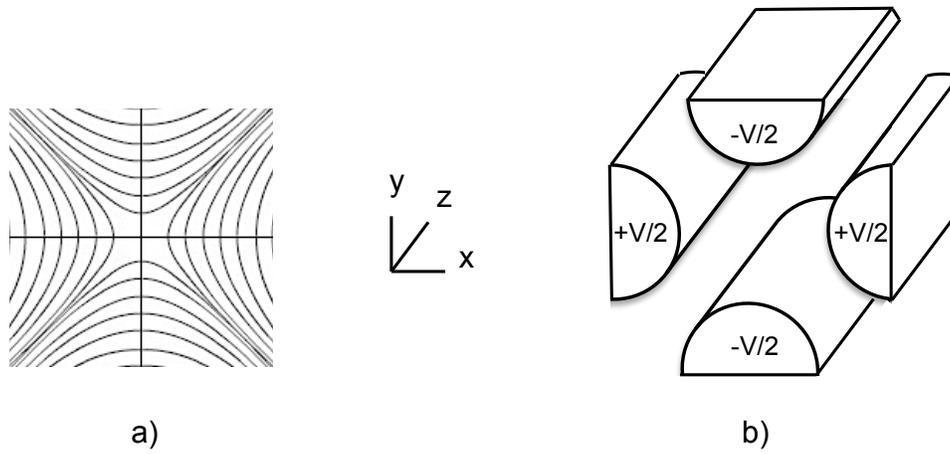
Figure 2.2: Radial cross-section of a linear Paul trap: a) equipotential lines of the quadrupole field, and b) electrode configuration. Neighbouring electrodes are of opposite polarity to generate the quadrupole field, which is switched at a radio-frequency to provide radial ion confinement.

tional stage of beam preparation during the production and delivery of the radioactive ions can thus be beneficial for many experiments at RIB facilities. An RFQ cooler and buncher can be applied for this purpose. In practice, the central trapping region of an RFQ can consist of many segmented electrodes that are used to create a potential gradient and guide the ions into and out of the trap. The rods of the TITAN RFQ consist of 24 segments that are used to create a trapping and extraction potential. These potentials are shown schematically in Figure 2.3. Collisional cooling takes place by injecting a neutral buffer gas (i.e., H or He) into the trapping region, and as the ions loose kinetic energy they accumulate in the axial potential minimum of the trap (Figure 2.3). By switching to the extraction potential, the ions in the extraction region will exit the trap in a well-defined ion bunch. This cooling processes takes place on a sub-millisecond timescale [35], and as a result, many RIB facilities make use of an RFQ cooler and buncher [36] for beam preparation. Details on the TITAN RFQ cooler and buncher can be found in Ref. [37].
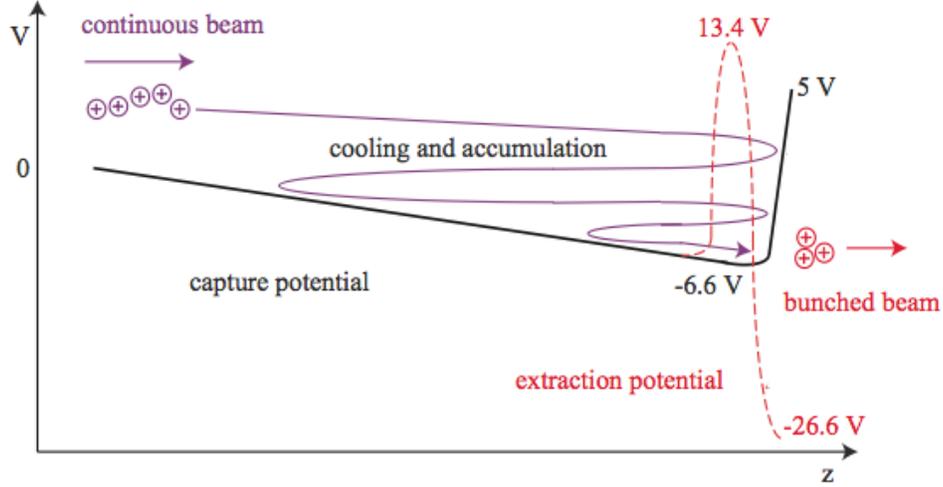
Figure 2.3: Schematic of the axial trapping (black) and extraction (red) potentials for the TITAN RFQ. The extraction potential is used to create an ion bunch separate from the incoming continuous beam (purple) (figure from Ref. [38] ©Maxime Brodeur. Reproduced with Permission).

2.2 Penning Traps for PTMS

Another way to achieve radial confinement is to apply a strong magnetic field along the trap axis, as in a Penning trap [39]. Hyperbolic electrodes, as seen in Figure 2.1b), with a potential difference between the end caps and the ring electrode provide axial confinement of the ions while generating an electric quadrupole field. The superposition of electric and magnetic fields results in harmonic ion motion at three different eigenfrequencies: axial ω_z, magnetron ω_+, and reduced cyclotron ω_-, as depicted in Figure 2.4. The two radial motions are coupled to the true cyclotron frequency ω_c of the ion via:

$$\omega_c = \omega_+ + \omega_- , \tag{2.1}$$

which is directly related to the mass m of the ion by:

$$\omega_c = \frac{qB_\circ}{m} , \tag{2.2}$$

9
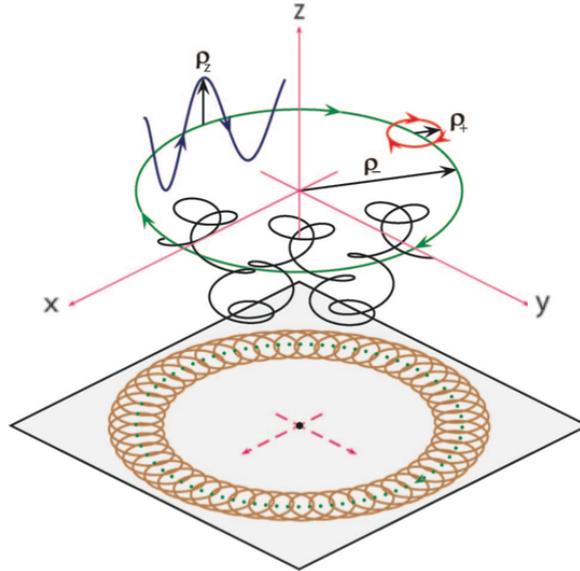
Figure 2.4: Trajectory of an ion in a Penning trap. The combined motion
(black) and independent eigenmotions are shown: harmonic oscillation
in the axial direction (blue); reduced cyclotron motion (green) and mag-
netron motion (red) (figure from Ref. [29] ©2010 Taylor & Francis.
Reproduced with permission).

Here, q is the charge and $B_\circ$ is the magnetic field strength along the trap axis.
Both the classical and quantum mechanical physics principles guiding an ion in
a Penning trap are well understood [39], which makes manipulation of the ion's
motions and measurement of the cyclotron frequency and mass possible.

2.2.1 Measurement Cycle

Details on high-accuracy mass spectrometry with stored ions, including differ-
ent measurement techniques, can be found in Ref. [9]. At TITAN, the cyclotron
frequency is determined by the time-of-flight ion-cyclotron-resonance (TOF-ICR)
technique [40], which requires a prepared bunch of ions for a measurement. Prefer-
ably consisting of only one ion, the bunch is set to specific and reproducible initial
conditions [41] and injected into the Penning trap on a pure magnetron radius. A

Figure 2.5: Schematic of the ion extraction electrodes between the MPET and micro-channel plate (MCP) detector. The time of flight of the extracted ions to reach the detector is recorded for the TOF-ICR technique (details in text) (figure from [38] ©Maxime Brodeur 2010. Reproduced with Permission).

quadrupole excitation of frequency ν_{RF}, amplitude A_{RF}, and duration T_{RF} is then used to excite the radial motion of the ions [42]. For $\nu_{RF} \equiv \nu_c$ a resonance condition is satisfied and for a specifically chosen T_{RF} and amplitude A_{RF}, an excitation will convert pure magnetron motion into reduced cyclotron motion, changing the energy of the ion bunch from a minimum to a maximum. The bunch is extracted onto a micro-channel plate detector (Figure 2.5) and the time of flight of the bunch to reach the detector is recorded. Repeating the cycle while scanning ν_{RF} around the expected cyclotron frequency will produce a resonance spectrum (Figure 2.6) where the true cyclotron frequency corresponds to a minimum in the time of flight (maximum energy after extraction). For a non-destructive technique that does not require extraction of the ions, the Fourier-transform ion-cyclotron-resonance (FT-ICR) [43] technique can be employed; however since the exotic nuclides studied at RIB facilities typically have short half-lives, injection and extraction of new ions would have to occur on a timescale of a few half-lives regardless. As a result most Penning-trap facilities studying short-lived nuclides employ the TOF-ICR technique, with SHIPTRAP being a notable exception [44].

2.2.2 Accuracy and Precision of a Penning-trap Mass Measurement

Mass determination by PTMS is currently accepted as the most precise and accurate method of determining atomic masses [3]. The technique has been extensively studied with stable ions [39], ensuring its accuracy to very high precision; with stable isotopes a relative mass uncertainty of $\delta m/m \sim 10^{-11}$ [10] has been demonstrated. A considerable advantage of PTMS is that the technique is independent of whether it is performed on stable or radioactive ions. All of the systematic inves-
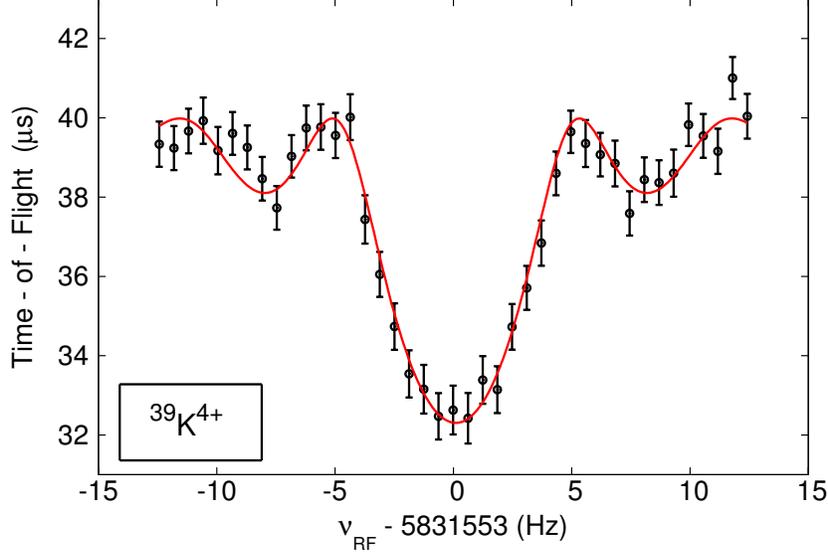
Figure 2.6: A TOF-ICR resonance curve for $^{39}K^{4+}$ with a $T_{RF} = 166$ ms excitation. The average time-of-flight and one standard deviation uncertainties (black) are shown with a theoretical fit [42] to the data (red) as a function of the excitation frequency ν_{RF}.

tigations and calibrations with stable ions can be directly applied to measurements on radioactive ions. The relative uncertainty for a frequency measurement using this technique [17] is approximated by a semi-empirical formula given by:

$$\frac{\delta \nu_c}{\nu_c} \propto \frac{1}{\nu_c T_{RF} \sqrt{N_{ions}}} \; , \tag{2.3}$$

where $\delta \nu_c$ is the uncertainty obtained from the determination of the cyclotron frequency ν_c, T_{RF} is the excitation time of the ions in the Penning trap, and $\sqrt{N_{ions}}$ is a statistical factor depending on the number of detected ions N_{ions}. When discussing the precision of a measurement, the convention taken is that precision is the inverse of the relative uncertainty, and either term may be found in the discussion[1].

There are a few limitations when dealing with exotic nuclides that reduces

---

[1]For example, a relative mass uncertainty of 10^{-11} corresponds to a measurement made to 1 part in 10^{11} or a measurement precision of 10^{11}.

the attainable precision. With either stable or radioactive ions, the excitation time is limited by the maximum storage time that ions can be trapped; however, with radioactive ions there is a fundamental limit caused by the ion's half-life. Thus, as the nuclides become increasingly exotic with shorter half-lives, the maximum storage time decreases, as does the attainable precision. Another limiting factor is the number of ions that can be measured during an experiment, which relies on the yield of isotopes and the total allotted measurement time. As the production of exotic nuclides becomes more difficult, the yield decreases and puts an additional constraint on the statistical factor. If this cannot be compensated for by longer measurement times, the resulting precision will suffer.

One way to compensate for these losses in precision is to increase the charge state of the ion. Since the cyclotron frequency scales linearly with the charge state (Equation 2.2), performing the measurement on a highly charged ion will reduce the relative uncertainty (increase the precision). It is this relationship that motivates charge breeding, particularly when the science case demands a certain precision and the aforementioned limitations make the measurement otherwise impossible. Coupling a charge breeder to a Penning-trap facility thus creates opportunities to perform high-precision measurements on nuclides further from stability with shorter-half lives and limited yields.

2.3   Electron Beam Ion Traps

An electron beam ion trap (EBIT) [45] consists of a series of cylindrical electrodes (drift tubes, Figure 2.1c)) through which a dense electron beam, compressed by a strong magnetic field, passes. The negative space charge of the electron beam is responsible for the radial confinement, whereas the drift tubes at the end of the trapping region create an axial potential barrier. The main components of an EBIT are the electron gun, the drift tubes, the magnet chamber, and the collector assembly, all shown in Figure 2.7. For external injection and extraction, additional beam line elements are required, as seen in the schematic of the TITAN EBIT in Figure 2.8.

In the case of external injection, ions are injected into the trapping region and confined axially by raising the potential on the end drift tubes. The electron beam
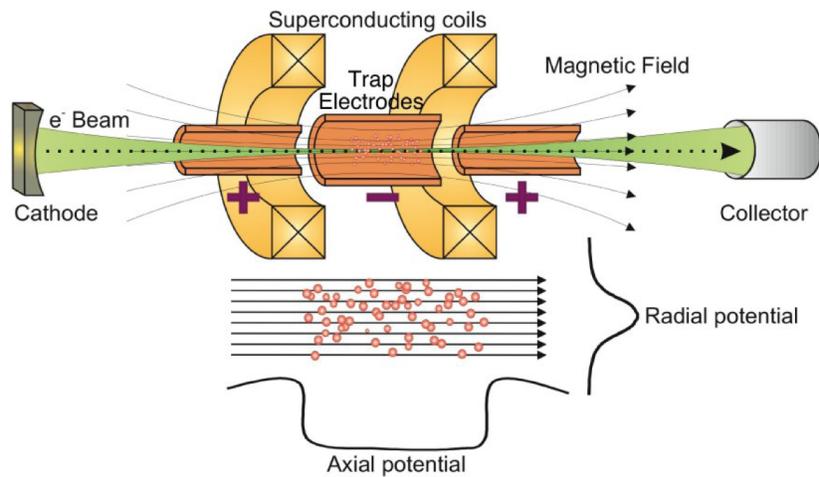
Figure 2.7: Illustration of an EBIT. From left to right: the electron gun assembly, the magnet coils and drift tube assembly, and the collector assembly. Typical trapping potentials are shown. (figure from Ref. [38] ©Maxime Brodeur. Reproduced with permission).
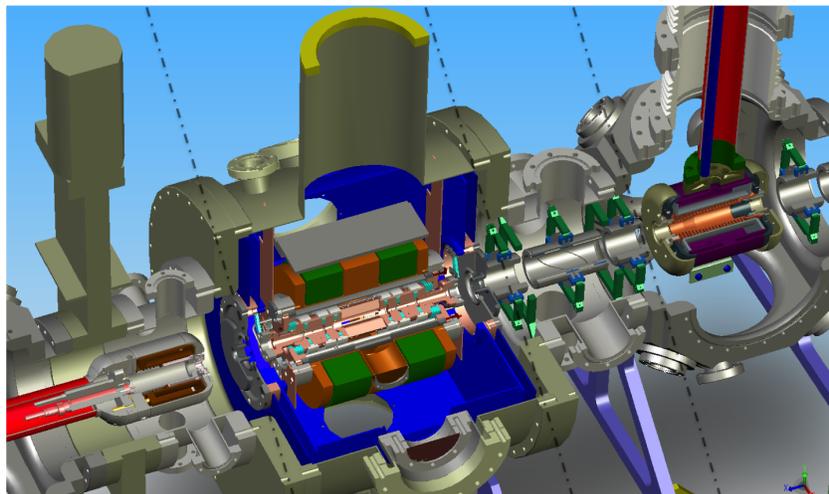
Figure 2.8: Schematic of the TITAN EBIT. From left to right: the electron gun assembly, the magnet chamber and drift tube assembly, the injection optics, and the collector assembly (Credit: Image Courtesy of TITAN).

originates at the cathode, passes through the trapping region reaching a focus at the trap centre, and diverges onto the collector assembly. In the region of electron-ion overlap charge-changing interactions occur, where the ions lose electrons to the beam (ionization), and recombine with electrons from the beam (recombination); these and additional processes are discussed below. After allowing charge breeding to take place, the highly charged ions can either be studied in trap (e.g. [46–49]), or extracted by switching to an extraction potential on the drift tubes. Various applications for the study of highly charged ions are possible [50], and an EBIT offers advantages in beam preparation, including the rapid production of narrow charge-state distributions.

2.3.1 Processes in an EBIT

Optimization of the EBIT settings for use with radioactive ions requires a qualitative understanding of the charge-changing processes that occur in the trapping region. An overview of the relevant processes and charge-breeding parameters are discussed below. The notation follows the convention used in Ref. [51], and a more quantitative discussion of the cross-sections and rate equations can be found in Ref. [52].

Ionization

The transition from a singly charged ion A^+ to a highly charged ion A^{q+} in an electron beam occurs through successive electron impact ionization. Each electron impact ionization (EI) depends on the energy of the electron beam E and the ionization potential $I_p(q+)$ of the $q+$ ion. The likelihood of an interaction occuring is determined by the cross-section $\sigma_{EI}(E, I_p(\mathrm{q}+))$, which follows the semi-empirical Lotz formula [53]. For the ionization of a given charge state, the cross-section has three main features: it is zero while $E < I_p$; it peaks for $2I_p < E < 3I_p$; and it falls asymptotically back to zero as $E \to \infty$. As the ion reaches higher charge states, the magnitude of the cross-section decreases, although the trends remain the same. The resulting ionization occurs in a step-wise fashion until the ionization potential exceeds the electron-beam energy. Given an infinite amount of time, successive electron impact ionization would result in all of the ions accumulating

in the highest possible charge state; however, as electron impact ionization competes with recombination processes, an equilibrium charge-state distribution will comprise many charge states.

Recombination

The relevant recombination processes in an EBIT are radiative recombination (RR) and charge exchange (CX) [51]. In the former, a free electron recombines with an ion resulting in the emission of a photon (reverse photoionization). Qualitatively, the cross-section for radiative recombination increases with the charge state and decreases with the electron-beam energy: lower energies and higher charge states favour recombination. In the latter, an electron bound to one ion or atom is transferred to another. Due to the strong Coulomb repulsion between interacting ions, the only relevant charge exchange interaction in an EBIT is between ions and neutral gas atoms or molecules. The recombination formed by charge exchange is independent of the electron-beam properties, as such it can be reduced to a negligible level by charge breeding in ultra-high vacuum conditions and using short storage times. For these reasons, charge exchange is considered to be a negligible process for the remainder of the text.

Charge-Changing Rates for Ions in an Electron Beam

The charge-state distribution evolves according to the coupled rate equations of all possible charge states:

$$\frac{dN_q}{dt} = R_{q-1}^{EI} - R_q^{EI} - R_q^{RR} + R_{q+1}^{RR} + R^{other} \quad . \tag{2.4}$$

where $\frac{dN_q}{dt}$ is the rate of change of the number of ions in charge state q and R represents the rates for electron impact ionization and radiative recombination that contribute to the number of ions in charge state q. The rates R_q are summarized in Table 2.1, where J is the current density of the electron beam, N_q is the number of ions in charge state q, and σ_q represent the respective cross-sections. An additional factor $f_{e;q}$ that describes the overlap of the electron beam with the ion bunch has been included to account for the fact that not all ions will be contained within

the electron beam at all times. Lower-order processes, such as charge exchange, resonant processes, and non-charge changing processes, including escape from the trapping region, are grouped in the term R^{other}.

Table 2.1: Relevant charge-changing processes in an EBIT.

Reaction	Process	Rate
EI	$A^q + e^- \rightarrow A^{q+1} + 2e^-$	$R_q^{EI} = J\, N_q\, \sigma_q^{EI}\, f_{e;q}$
RR	$A^q + e^- \rightarrow A^{q-1} + \gamma$	$R_q^{RR} = J\, N_q\, \sigma_q^{RR}\, f_{e;q}$

Substituting the information in Table 2.1 into Equation 2.4 and neglecting the term R^{other} gives:

$$\frac{dN_q}{dt} = J\, f_{e;q} \left(\sigma_{q-1}^{EI}\, N_{q-1} - \sigma_q^{EI}\, N_q - \sigma_q^{RR}\, N_q + \sigma_{q+1}^{RR}\, N_{q+1} \right) \ . \tag{2.5}$$

This equation brings important features of charge breeding in an EBIT to attention:

1. The rate of ions entering and leaving the charge state q scales with the electron-beam current density and the electron-ion-overlap factor.

   - Since the electron-beam current density, electron-ion-overlap factor, and interaction time all play the same role in the charge-state evolution, changing the electron-beam current density or electron-ion overlap factor will either speed up or slow down the charge-breeding process.

2. The cross-sections couple the evolution of the charge states $q - 1$, q, and $q + 1$:

   - Since the cross-section depends on the electron-beam energy, changing the electron-beam energy will change the charge-state abundance at any given time.

In terms of optimizing the EBIT for PTMS with radioactive ions, these two features suggest that appropriate tuning of the electron-beam properties can reduce radioac-
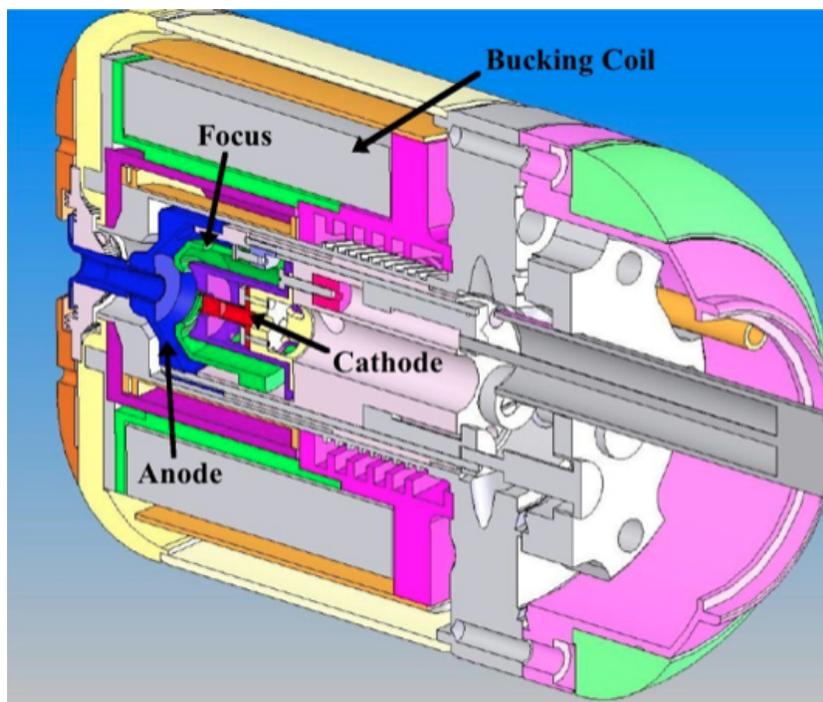
Figure 2.9: Cross-section view of the EBIT gun assembly at TITAN. The cathode (red) emits the electrons, which are pulled by the focus (dark green) and accelerated towards the left through the anode (blue). The bucking coils (grey) are used to reduce the residual magnetic field at the cathode (Credit: Image Courtesy of TITAN).

tive decay losses and maximize the abundance of ions in the desired charge state. A detailed discussion of the electron-beam properties follows.

2.3.2 Properties of the Electron Beam

The properties of the electron beam in the trapping region are determined by a number of factors, including elements in the electron gun assembly, the trap electrodes, and the magnetic field. The gun assembly, which consists of a cathode, anode and focus electrodes, and bucking coils, is shown in Figure 2.9 for the TITAN EBIT. The cathode is biased and heated resulting in thermionic emission of the electrons [54] which are pulled off of the cathode by the focus and accelerated towards the

anode. The electron-beam current can thus be controlled by adjusting the bias on the focus electrode. The electron-beam energy at the trap centre is defined by the potential difference between the bias on the cathode and the bias on the central trap drift tube (Figure 2.7). Since the drift tube potential should be fixed to within a few tens of volts of the ion beam transport energy for optimal trapping, the cathode bias can be adjusted to obtain the desired electron-beam energy. Finally, the electron-beam current density will depend on the electron-beam current and the size of the electron beam, which is in part shaped by the bucking coils. The bucking coils are used to reduce the magnetic field at the position of the cathode (discussed below).

The equations and discussion relevant to calculating the electron-beam radius can be found in Ref. [51] and are summarized herein. The smallest possible electron-beam radius would occur if the electrons were pulled off the cathode at zero-temperature and in a magnetic field free region. Under these conditions, the electrons, compressed by the magnetic field B in the trapping region, would form a beam with the Brillouin radius [55]:

$$r_b[\text{m}] = \frac{1.5 \times 10^{-4}}{B[\text{T}]} \sqrt{\frac{I_e[\text{A}]}{\sqrt{E[\text{keV}]}}} \tag{2.6}$$

However, this is an overestimate of the compression achieved since the cathode is heated and not located in a magnetic field free region.

Herrmann theory [56] defines the electron-beam radius through which 80% of the beam passes as:

$$r_H = r_b \sqrt{\frac{1}{2} + \frac{1}{2} \sqrt{1 + 4\left(\frac{8kT_c r_c^2 m_e}{e^2 r_b^4 B^2} + \frac{B_c^2 r_c^4}{B^2 r_b^4}\right)}} \ , \tag{2.7}$$

$$r_H^{min} = \lim_{B_c \to 0} (r_H) \approx 2.50 \cdot 10^{-4} \, T_c^{1/4} \sqrt{\frac{r_c}{B}} \ . \tag{2.8}$$

Here, T_c, is the temperature of the cathode; B_c is the residual magnetic field at the cathode; r_c is the cross-sectional radius of the cathode's emitting surface; k is the Boltzmann constant; m_e is the mass of the electron; e is the charge of the electron; all units are in SI. Making use of the bucking coils in the gun assembly to zero

19
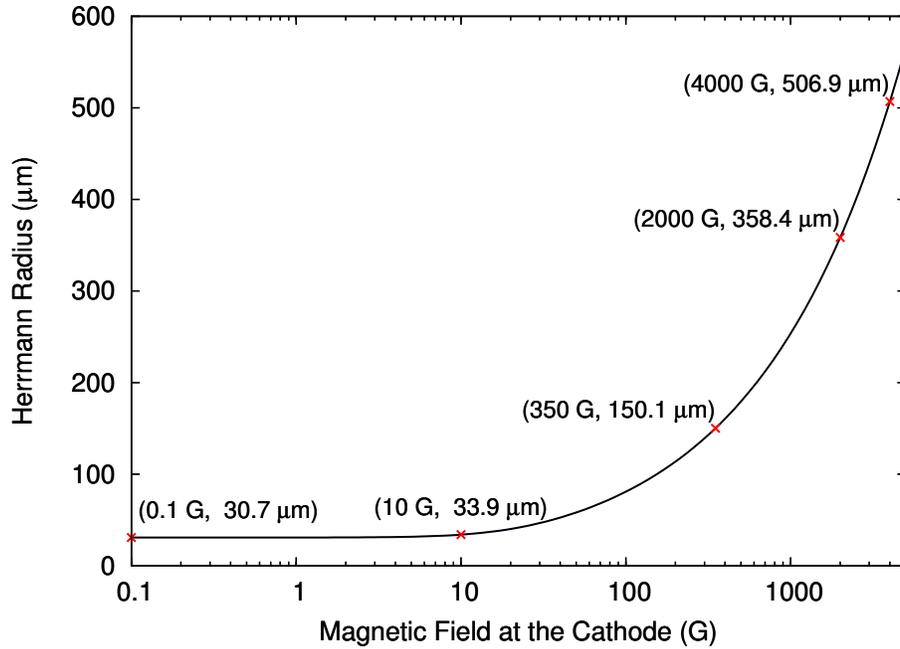
Figure 2.10: Herrmann radius of the electron beam as a function of the residual magnetic field at the cathode for typical values in the TITAN EBIT: $T_c = 1470$ K, $r_c = 0.00170$ mm, $B = 4.5$ T, $E = 2.5$ keV, $I_e = 0.100$ mA.

the magnetic field at the cathode results in the minimum attainable beam radius, shown in Equation 2.8.

At TITAN, the cathode is typically heated to $T_c = 1470$ K and has an emission surface with $r_c = 1.70$ mm [19]. For an electron-beam energy of 2.5 keV and current of 100 mA, the resulting smallest possible electron-beam radius when operating in a 4.5 T magnetic field is 30 μm. However, simulations of the EBIT magnetic field show that the residual magnetic field at the cathode can exceed 0.2 T (2000 G) [57]. The growth of the electron-beam radius as a function of the magnetic field at the cathode for these conditions is shown in Figure 2.10; a factor of 5 increase in the Herrmann radius is possible with a magnetic field of only a few hundred Gauss at the cathode.

The electron-beam radius will affect both the current density and the electron-

20

ion-overlap factor. A beam radius of r_H=30-150 μm corresponds to a current density ranging from 110-2700 A cm^{-2} according to:

$$J = \frac{0.8 \, I_e[\text{A}]}{\pi \, r_H[\text{cm}]^2} \quad .$$ (2.9)

This range of electron-beam current densities has the potential to change the rate of charge evolution by more than an order of magnitude. Thus, correcting for residual magnetic field at the cathode to reduce the electron-beam radius is a critical step in preparing for charge breeding. Despite this, the smallest possible electron-beam radius is not necessarily optimal if it is smaller than the initial radius of the injected ions. In this case, the electron-ion-overlap factor, defined as the ratio of the number of ions inside the electron beam N_q^{in} to the total number of trapped ions N_q:

$$f_{e;i} \equiv \frac{N_q^{in}}{N_q} \quad ,$$ (2.10)

will increase with the electron-beam radius. The so-called effective current density

$$J_{eff} = J f_{e;q} \quad ,$$ (2.11)

takes both the true electron-beam current density and electron-ion overlap factor into account, and a balance needs to be achieved between having a radius that is large enough to overlap with the ions while still maximizing the current density. Procedurally it is best to optimize the ion injection to achieve a small initial radius, minimize the residual magnetic field at the cathode, and provide smaller electron beam compression as needed by reducing the magnetic field at the trap centre until an optimal balance has been obtained.

These theoretical foundations provide the necessary framework for modelling charge breeding in an electron beam (Chapter 4). Furthermore, assuming that these foundations are a good description of the experimental conditions (Chapter 5), they will also provide a guideline for optimizing the electron-beam properties in an EBIT for PTMS with highly charged, radioactive ions. From the cross-sections, it follows that the charge-state distribution depends on the electron-beam energy E and the resulting balance between ionization and recombination processes. Since

the rates for both electron impact ionization and radiative recombination scale with the effective current density, the evolution of charge states depends on the product $J_{eff} \cdot t$, where t is the amount of time the ions interact with the electron beam. By combining Equations 2.8 and 2.9 the charge-state evolution can be written in terms of parameters that can be independently controlled: the electron-beam current, the magnetic field in the trapping region, and the charge-breeding time. Application of the information from this section benefits the goal of optimal charge breeding for PTMS on radioactive ions, creating an efficient stage of beam preparation and allowing for the maximum increase in precision.

2.4 Summary

Standard applications of ion traps have been discussed in context of the TITAN experiment. The three different types of ion traps that were discussed, the Paul trap, Penning trap, and electron beam ion trap, have niche applications that complement each other for precision mass measurements on radioactive ions. For example, the cooling and bunching of ions in an RFQ linear Paul trap occurs on a sub-millisecond time scale, making it a preferred stage in beam preparation at RIB facilities. On the other hand, the extensive work that has been put into developing Penning traps for precision mass measurements have made it the most precise and accurate tool for determining the masses of both stable and exotic nuclides.

Finally, the use of an EBIT for charge breeding is discussed in some detail, specifically in the context of improving the precision of a mass measurement with radioactive ions. The most relevant charge-changing processes in an EBIT have been identified and the rate equation for the evolution of charge states is discussed in detail along with the properties of the electron beam. These foundations have provided the necessary framework for both modelling and optimizing charge breeding for PTMS with radioactive ions.

Chapter 3

Experimental Setup

The Penning-trap mass measurements made at TITAN are the result of a complex and integrated mixture of experimental apparatuses and techniques that have been designed for the production, preparation, and precision manipulation of radioactive ions. An overview of the experimental setup, including the production of exotic nuclides at TRIUMF, is provided in this chapter. Typical operating conditions for the preparation traps at TITAN are given along with a description of a typical mass measurement cycle. The discussion provides context for Chapters 4, 5, and 6.

3.1 Radioactive Beam Production and Delivery at TRIUMF

Exotic nuclides are produced at the Isotope Separator and ACcelerator (ISAC) facility [58] at TRIUMF for study in one of the two experimental halls (Figure 3.1). ISAC is an isotope separation on-line (ISOL) [59] facility, where a proton beam is received from the TRIUMF main cyclotron. With beam energies reaching up to 500 MeV and beam currents of up to 100 μA, this high-power proton beam is incident on a target chosen to optimize production of the desired isotope. The radioactive isotopes are produced inside the target and diffuse out directed towards an ion source. The ion source is either a surface ion source (SIS), resonant ionization laser ion source (RILIS) [60], forced electron beam induced arc discharge (FEBIAD) ion source [61], or the newly developed ion-guided laser ion source (IG-LIS) [62], de-
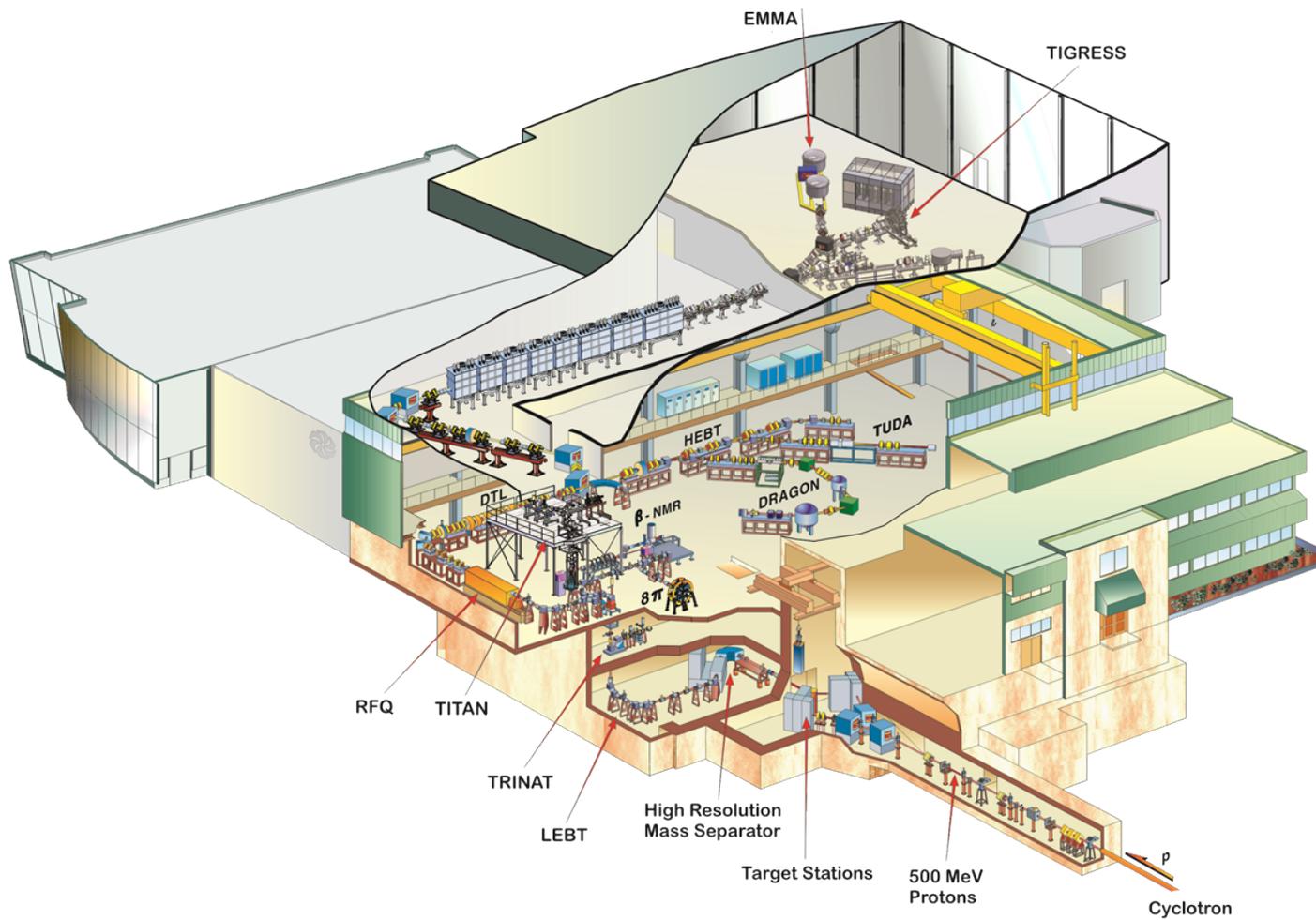
Figure 3.1: The experimental halls at ISAC. The beam line for the ISOL production of radioactive ions at TRIUMF is shown, and includes the proton beam line, target / ion source combination, mass separator, and ion transport system. Various experimental setups, including TITAN, are shown. (Credit: Image Courtesy of TRIUMF).

pending on the isotope of interest and the required suppression of contamination coming out of the target.

The resulting RIB passes through a dipole mass separator with a mass resolving power of $R = \frac{m}{\Delta m} \sim 3000$. All nuclides that have a mass within this resolving power are separated out, leaving only the isotope of interest, excited nuclear states, and isobars that are too close together in mass. A low energy beam transport (LEBT) line is used to transport the ions as a continuous beam into the ISAC experimental hall, where yields can be determined based on measurements of characteristic radiation (i.e., α, β, γ). Subsequently, the beam is delivered as a low-energy beam or reaccelerated for high-energy delivery to the ISAC experimental halls. As seen in Figure 3.1, the ISAC experimental halls hosts a variety of Canadian and international experiments, including TITAN, that are grouped into experimental areas for low-energy experiments (60 keV), medium energy experiments (1.8 MeV/nucleon) and high energy experiments (up to $\sim$12 MeV/nucleon).

3.2 The TITAN Experimental Setup

The TITAN facility is located in the low-energy experimental hall at ISAC and consists of three ion traps that are dedicated to the preparation and manipulation of short-lived ions for high-precision mass measurements [5] and in-trap decay spectroscopy [6, 7]. These ion traps are an RFQ [37] linear Paul trap (the TITAN RFQ, Section 2.1), a precision measurement Penning trap (MPET) [63] (Section 2.2), and an EBIT [20, 64] (Section 2.3); their respective locations in the TITAN setup are shown in Figure 3.2. The RIB delivered from ISAC is received at the TITAN RFQ, accumulated, and the energy spread of the beam is reduced through thermalization with a helium buffer gas. The ions are extracted as a bunch with a transport energy that is typically in the range of 1 to 3 keV. The ion bunch has two possible paths, as seen in Figure 3.2, depending on whether the experiment is to be performed on singly or highly charged ions.

In the case of highly charged ions, the ions are transported from the TITAN RFQ to the EBIT where they undergo charge-changing processes in an electron beam (Section 2.3.1). The EBIT was built in collaboration with the Max Planck Institute for Nuclear Physics in Heidelberg, Germany [65]. The trapping region,
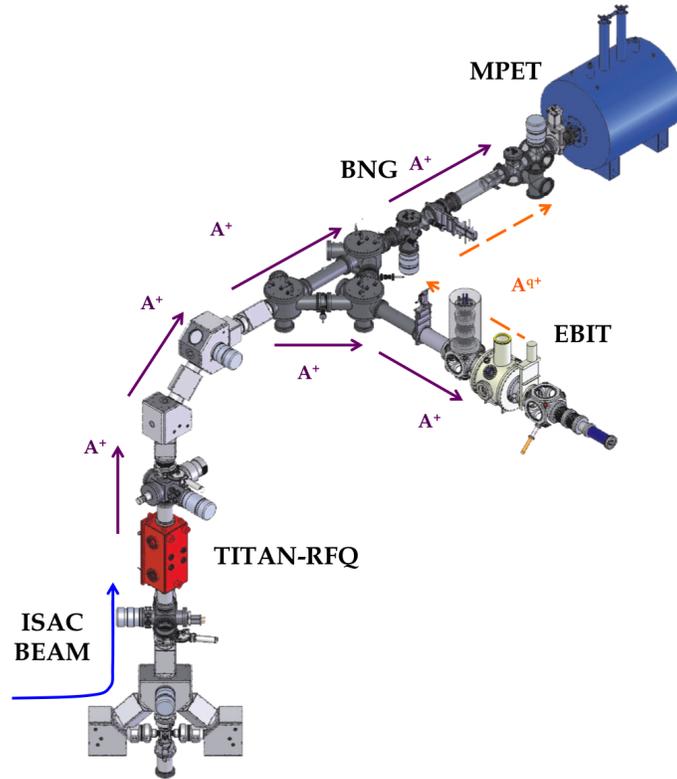
Figure 3.2: The TITAN experiment depicting the location of the TITAN RFQ, the EBIT, the Bradbury-Nielsen gate (BNG), and the MPET. The respective ion paths are shown for SCI A^+ (solid purple) and for HCI A^{q+} (dashed orange) (Credit: Image Courtesy of TITAN).

shown in Figure 3.3, consists of eight cylindrical drift tubes placed symmetrically about the trapping centre, and a central drift tube separated into eight segments to allow radial spectroscopic access to the trapping region for decay-spectroscopy. The central drift tube (Figure 3.3 S1-8), is biased to a voltage near the ion beam transport energy and the small drift tubes on either side (Figure 3.3 C1 and G1) are used to create the axial potential barriers.

The electron gun and collector assembly are designed to allow electron beam currents of up to $I = 5$ A and electron beam energies of up to $E = 70$ keV. Currently, typical operating values are $I = 100$ mA and $E = 1$ to 6 keV. The cryogen-
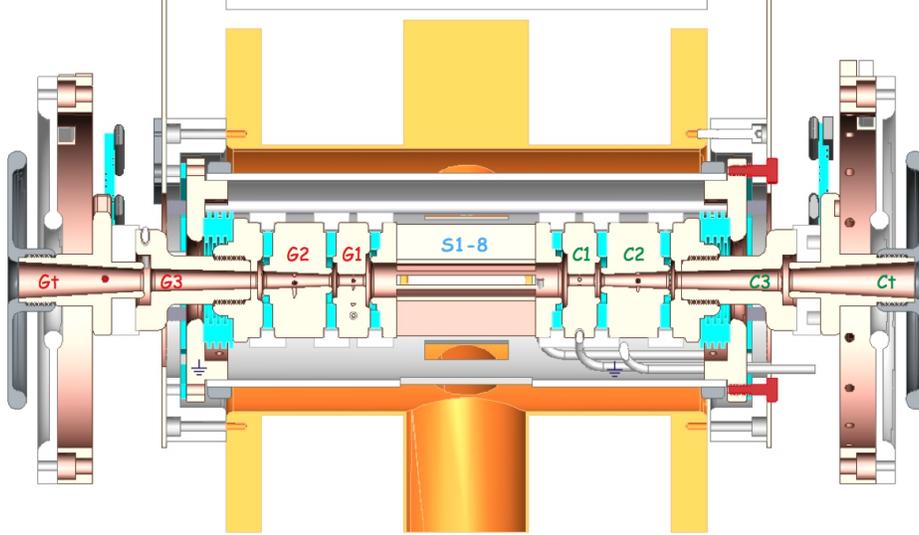
Figure 3.3: The trapping region of the TITAN EBIT. The trap drift tubes are labeled out from the central drift tube (S) towards either the gun (G) or collector (C) assembly, with C1 corresponding to the first drift tube on the collector side and so on. S1 through S8 denotes the eight segments of the central drift tube (Credit: Image Courtesy of TITAN).

free magnet chamber holds two superconducting magnetic coils in a Helmholtz configuration designed to provide magnetic fields of up to $B = 6$ T (typically operated at $B = 4.5$ T). On each side of the collector assembly, additional electrodes (Figure 2.8) allow control of the injection into and extraction from the trapping region. Technical details of the design of the TITAN EBIT and first tests with RIB can be found in Ref. [19, 20]. Many successful measurements for PTMS with highly charged, radioactive ions have already been demonstrated [21, 25, 66, 67].

The ions extracted from the EBIT have velocities that depend on their mass-to-charge ratio, which creates a separation in the time of flight T of different charge states and species according to:

$$T = \sqrt{\left(\frac{m}{q}\right)\frac{d^2}{2U}} \ ,$$

(3.1)
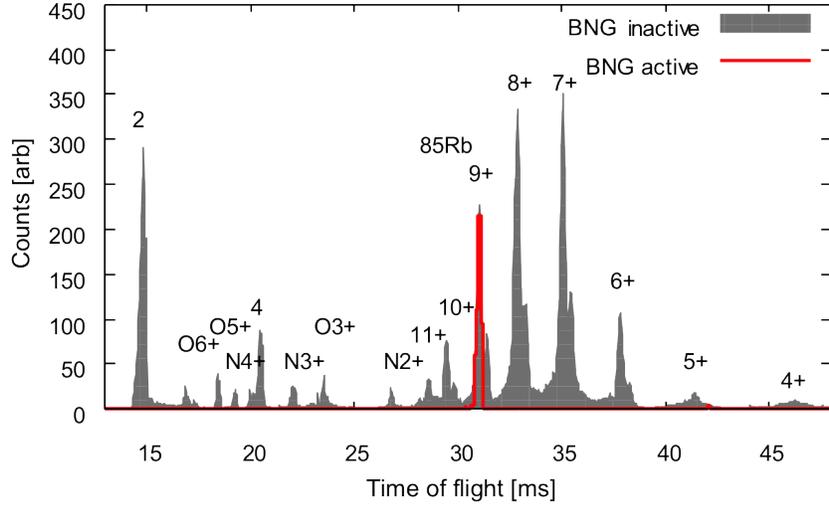
Figure 3.4: Time-of-flight spectra of highly charged ions after being extracted from the EBIT with and without Bradbury-Nielsen gate (BNG) operation. ^{85}Rb charge states 4-11+ are marked, as are peaks of nitrogen, oxygen, and other gas ions (O^{q+}, N^{q+}). The red spectrum identifies the ^{85}Rb^{9+} that has been selected by the BNG for injection into the MPET (details in text).

where d is the distance to the detector and U is the potential on the segmented drift tube in the EBIT. A micro-channel plate detector can be inserted into the beam line to produce a time-of-flight spectrum of the extracted ions; an example is shown in Figure 3.4 for charge-bred ^{85}Rb and residual gas ions. The separation in time of flight allows for charge-state identification, and charge states 4+ through 11+ of ^{85}Rb are marked along with peaks corresponding to various residual gas atoms (e.g., nitrogen and oxygen). Since ions in higher charge states move faster through the beam line, they have a shorter time of flight and appear closer to the y-axis. A specific mass-to-charge ratio is selected for measurement by a BNG [68] before the ions are injected into the MPET. The time-of-flight spectrum of ions after selection by the BNG is also shown in Figure 3.4. For experiments without charge breeding, the ions will bypass the EBIT and be transported directly into the MPET.

Once the ions are inside the MPET, they are manipulated with RF-excitations and extracted to apply the TOF-ICR technique for mass determination (Section

2.2.1). A sample resonance curve taken using the TOF-ICR technique with stable $^{39}K^{4+}$ beam is seen in Figure 2.6. During a mass measurement each experimental resonance is compared to the theoretical resonance curve [42] to determine the best fit for the true cyclotron frequency; in the example resonance curve, $\nu_c = 5.831\ 553\ 105(77)$ MHz. Using precise knowledge of the charge state and magnetic field strength, the mass of the isotope can thus be extracted from:

$$\nu_c = \frac{qB_\circ}{2\pi m} \ .$$ (3.2)

The magnetic field strength at the time of measurement is determined by performing reference measurements on an isotope with a well-known mass before and after each measurements on the isotope of interest, and interpolating the result. This interpolation accounts for linear variations of the magnetic field strength with time [63]. Here, the $^{39}K^{4+}$ cyclotron frequency was used as a reference measurement for a Q-value determination of the $^{51}Cr(e^-, \nu_e)^{51}V$ reaction (Chapter 6).

During an experiment, data are collected for an amount of time that is chosen to minimize the statistical uncertainty while also keeping time-dependent systematic effects [63] at a minimum. More details regarding the analysis procedures and systematic effects for a mass measurement can be found in Ref. [63] and are discussed and applied in more detail in Chapter 6. Future additions to the TITAN beam line will include a multi-reflection time-of-flight spectrometer [69] for beam purification and a cooler Penning trap [70, 71] for reducing the energy spread of highly charged ions prior to injection into the MPET. A detailed overview of the TITAN facility can be found in Ref. [5].

The TITAN collaboration has demonstrated high-precision mass measurements and direct Q-value measurements with both singly and highly charged ions, ranging from studies on the nuclear structure of light halo nuclides $^{6,8}He^+$ [72], $^{11}Li^+$ [73], $^{11}Be^+$ [74], to Standard-Model tests with $^{74}Rb^{8+}$ [21], and neutrino physics studies with $^{71}Ga^{22+}$, $^{71}Ge^{22+}$ [67]. These measurements have covered the shortest half-life and most exotic nuclide measured in a Penning trap as well as new charge-breeding techniques, making TITAN and ISAC a well-established pairing for high-precision mass spectrometry on exotic nuclides.

Chapter 4

The Impact of Charge Breeding on PTMS for Radioactive Ions

The techniques for Penning-trap mass measurements on singly charged radioactive ions [17] and on highly charged stable ions [75] were independently developed and combined for the first time at the TITAN facility. The potential for more than an order of magnitude in precision gain by increasing the charge state of an ion prior to a measurement makes charge breeding an attractive option; however, employing this technique with radioactive ions has additional complications due to the limited yields and inherent losses from radioactive decay. If these losses affect the number of ions that can be measured, the statistical precision will decrease, possibly negating the precision gained by increasing the charge state. As the only collaboration that performs PTMS on highly charged, radioactive ions, TITAN has a unique need to address this concern. For the first time, a quantitative and systematic approach that is based on theory has been established to determine the benefits of charge breeding on PTMS with radioactive ions.

Simulations are a valuable tool in theoretical science as they provide insight into general trends even before experiments can be performed. Charge breeding in an electron beam is well suited to numerical simulations, where numerical integration of the rate equations from Section 2.3.1 provides the evolution of charge states as a function of the different charge-breeding conditions. In this chapter, the output of a charge-breeding simulation is combined with radioactive decay losses

and experimental efficiencies to allow for a comparison of the precision that would be obtained by performing a measurement on highly charged, radioactive ions to one with singly charged ions. This gain factor, which is sensitive to the charge-breeding conditions and specific to PTMS, forms the basis for an optimization procedure that has been designed to provide the optimal charge-breeding conditions for PTMS with highly charged, radioactive ions. The discussion is framed in the context of the charge-state evolution of the exotic nuclide ^{74}Rb, which has a half-life of $t_{1/2} = 65$ ms. This nuclide has been chosen for two reasons: stable Rb, which has the same electronic properties as exotic Rb nuclides, is easily obtained from a surface ionization source for off-line experiments (Chapter 5); and ^{74}Rb lies at the proton drip-line of the nuclear chart and has the shortest half-life of all neutron-deficient Rb isotopes. Hence, ^{74}Rb makes an excellent case study of the effect of charge breeding for PTMS with short-lived exotic nuclides.

4.1 Simulated Evolution of Charge States

4.1.1 Charge Breeding SIMulation (CBSIM)

Understanding the evolution of charge states of ions in an electron beam and the effect of the charge-breeding parameters is central to preparing for a PTMS measurement that will be more precise than one made with singly charged ions. The well-established CBSIM (Charge Breeding SIMulation) [76] is a program that provides the fraction of ions $\eta_{pop}(q)$ in a given charge state q for a specified electron-beam current density J, electron-beam energy E, and charge-breeding time t_{CB}. Featuring electron impact ionization with Lotz cross-sections [53], radiative recombination and charge exchange (Section 2.3.1), loss of ions by Coulomb heating, and integration on a logarithmic time scale, CBSIM performs numerical integration over the coupled rate equations from Section 2.3.1 and provides a graphical representation of the result.

Since the evolution of charge states under electron impact ionization and radiative recombination evolves with the product of J and t_{CB} (Section 2.3.1), the dependent variable in CBSIM is their product, or J-time, in units of A cm^{-2} s. Input parameters include the electron-beam energy E, the electron ionization potentials

$I_p(q+)$ and binding energies $B_e(q+)$ for the nuclide of interest, and the atomic number Z and mass number A of the nuclide. The program also includes the ability to turn processes off and the option to run the simulation with a single ion bunch injected at a fixed time or by adding ions to the electron beam at constant rate. For the purpose of studying the charge evolution at TITAN, the simulation was used with single ion bunch injection. Since charge exchange is not an interaction between the ions and the electron beam and since the vacuum conditions in the TITAN EBIT are better than 10^{-9} Pascals, processes involving charge exchange were omitted from the simulation. The output of the program is the fraction of ions $\eta_{pop}(q, Jt, E)$ in each charge state $q+$, for a range of J-time values, and a given electron-beam energy E.

4.1.2 Charge-State Evolution

An example of the charge-state evolution of Rb ions calculated with CBSIM for an electron-beam energy of $E = 1.30$ keV is shown in Figure 4.1. The initial conditions are chosen such that the ion bunch begins with all of the ions in the 1+ charge state and the electron beam and ion bunch perfectly overlap throughout the evolution. The early transitions out of the low charge states occur relatively quickly, then as the magnitude of the electron impact ionization cross-section decreases with the charge state, the evolution slows down. The result, when plotted on a logarithmic J-time scale, is the nearly equidistant appearance of successive charge states. A vertical line drawn at any given J-time intersects with the charge-state abundances of the corresponding charge-state distribution. For example, at a J-time of 0.1 A cm^{-2} s, the charge-state distribution runs from charge state 5+ to 11+ with the 8+ charge state having the maximum abundance of about 30%. For most values of J-time, the maximum abundance in a single charge state is around 30%, with a notable exception for a J-time greater than 500 A cm^{-2} s. For greater values, the relative composition of the ion bunch is no longer changing. This equilibrium charge-state distribution consists of about 70% of the ions in the 26+ charge state, 20% in the 25+ charge state, and only 10% populating the maximum charge state of 27+.
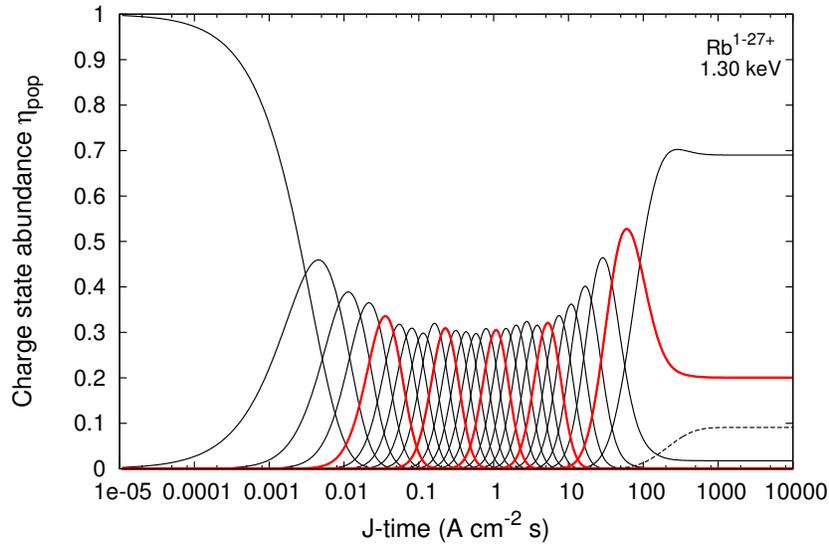
Figure 4.1: Charge-state evolution of Rb^{q+} for $E = 1.30$ keV. A vertical slice at fixed time shows the charge-state distribution of an ion bunch after a given J-time. Every fifth charge state (bold red) and the maximum charge state (dashed black) are emphasized to guide the eye.

4.1.3 Threshold Charge Breeding

A Rb^{27+} ion is in a Ne-like electronic configuration, which forms a closed electronic shell. At closed shells there is a gap in ionization potentials to reach the next charge state: here $I_p(26+) = 1294$ keV and $I_p(27+) = 3129$ keV. This gap allows for a wide range of electron-beam energies to produce Ne-like Rb without ionizing Rb^{27+}. From the discussion in Section 2.3.1, the maximum value of an electron impact ionization cross-section is for an electron-beam energy that is 2-3 times the ionization potential, and the radiative recombination cross-section decreases with energy. Thus, by changing the electron-beam energy within this gap in ionization potentials, the relative abundances of the equilibrium charge states can be changed. Figure 4.2 shows that a change in the electron-beam energy of only 50 eV, from $E = 1.30$ keV to $E = 1.35$ keV, significantly changes the equilibrium charge-state distribution: the fraction of ions in the 27+ charge state has increased to over 50%
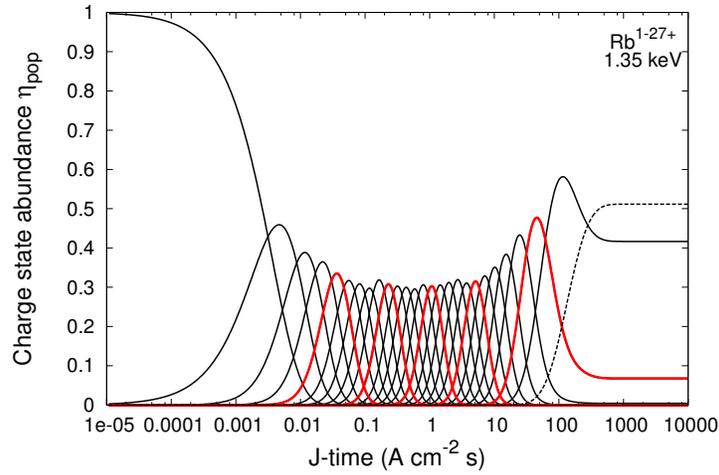
Figure 4.2: Charge-state evolution of Rb^{q+} for $E = 1.35$ keV. As the energy increases from 1.3 keV, the equilibrium begins to favour 27+ over 26+. Every fifth charge state (bold red) and the maximum charge state (dashed black) are emphasized to guide the eye.
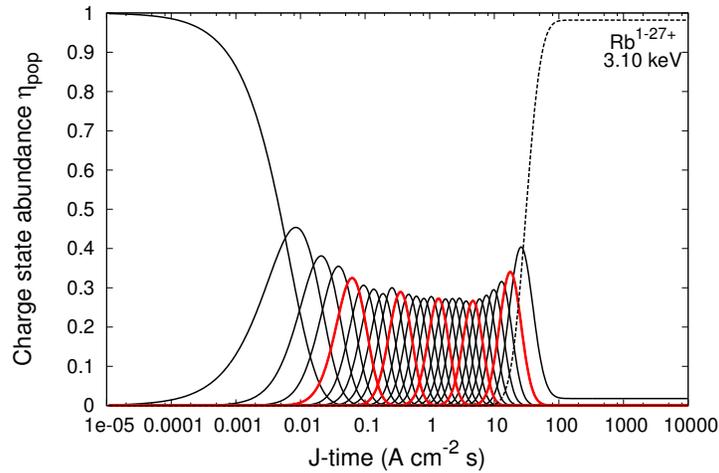
Figure 4.3: Charge-state evolution of Rb^{q+} for threshold charge breeding to the Ne-like configuration at $E = 3.1$ keV. Depletion of the 1+ charge state takes slightly longer than at $E = 1.3$ keV due to the smaller EI cross-section at low charge states, but the equilibrium charge-state distribution greatly favours 27+ by taking advantage of the threshold effect (see text). Every fifth charge state (bold red) and the maximum charge state (dashed black) are emphasized to guide the eye.

from 10% due to the increased ionization cross-section and reduced recombination cross-section. By choosing an electron-beam energy that is just below the threshold for ionizing 27+, as in Figure 4.3, the fraction of ions in a single charge state is maximized, with nearly all the ions in the 27+ charge state and only a small amount in the 26+ charge state.

It is worth mentioning that this so-called threshold charge breeding has another practical application: it can be used to separate isobars (i.e., isotopes with the same mass number A and different proton number Z). For an electron-beam energy that is at the threshold of opening a closed electronic shell, the maximum charge state will be element specific, changing the mass-to-charge ratio of the highly charged isobars. Once the charge breeding is complete, the ions can be extracted and subjected to any number of separation techniques that selects only the desired isotope through its mass-to-charge ratio. At TITAN this is done by taking advantage of the time-of-flight separation and selecting the desired mass-to-charge ratio with a Bradbury-Nielsen gate (Section 3.2). This was successfully demonstrated during a measurement where ^{71}Ge and ^{71}Ga were charge bred to their Ne-like charge states and separated [67].

Threshold charge breeding to a closed electronic shell other than Ne-like (e.g., He-like, Ar-like) is also possible; however, since the number of ions in a single charge state $q+$ is maximized for $2I_p(q-1) < E < 3I_p(q-1)$, only closed shells with a gap in ionization potentials satisfying $2I_p(q-1) < I_p(q)$ offer this advantage. For typical beam energies in the 1 to 6 keV range the Ne-like gap is favourable for all nuclides with $Z = 32$ to 52 [77], and for this reason it is the only case considered herein. The advantages of threshold charge breeding are well-known and have been discussed in Refs. [76, 78, 79].

4.2 The Optimal Charge-Breeding Conditions

4.2.1 Quantifying the Precision Gained (G_{HCI}) in PTMS with Highly Charged, Radioactive Ions

The benefits of threshold charge breeding became apparent in the previous section by studying various equilibrium charge-state distributions produced by CBSIM.

Since threshold charge breeding offers the greatest number of ions in a single charge state, it is likely that it offers the optimal charge breeding when preparing for a Penning-trap mass measurement. In order to verify this and to derive more general and quantitative statements, a variable that is sensitive to the charge-breeding conditions and specific to PTMS is required.

For this purposed, a factor that relates the attainable precision of a mass measurement made on highly charged ions (HCI) to one made without charge breeding on singly charged ions (SCI) is defined:

$$G_{HCI} = \frac{(\delta m/m)_{SCI}}{(\delta m/m)_{HCI}} \quad , \tag{4.1}$$

where the relative mass uncertainty from Equation 2.3:

$$\frac{\delta m}{m} \propto \frac{m}{q \, B_\circ \, T_{RF} \sqrt{N_{det}}} \tag{4.2}$$

is used. Here q is the charge state, $B_\circ$ is the magnetic field strength, T_{RF} is the excitation time, and N_{det} is the number of detected ions. Substituting Equation 4.2 into Equation 4.1 for both HCI and SCI gives:

$$G_{HCI} = q \sqrt{\frac{N_{det}^{HCI}}{N_{det}^{SCI}}} \quad . \tag{4.3}$$

This relative precision gain provides the expected linear increase with charge state while including the important contribution from changes in the statistical factor $\sqrt{N}$. A comprehensive comparison of N_{det}^{HCI} and N_{det}^{SCI} follows.

The number of ions detected in a measurement will depend on the production rate of the isotope of interest and the experimental efficiencies; however, special consideration needs to be made for when the yield at the MPET, denoted by χ, exceeds one ion per cycle. The TOF-ICR technique is best carried out with only a single ion in the trap, therefore losses due to transportation, trapping, and charge breeding will not affect the measurement precision, so long as a single ion is delivered to the MPET each cycle ($\chi \geq 1$). The number of detected ions during a measurement is then the product of the number of measurement cycles N_{cycle} with

the number of ions measured per cycle (i.e., either 1 or χ):

$$N_{det} = \begin{cases} N_{cycle} & \text{if } \chi \geq 1 & \text{(4.4a)} \\ N_{cycle}\,\chi & \text{if } \chi < 1 \ . & \text{(4.4b)} \end{cases}$$

For a measurement with HCI, the number of ions arriving at the MPET is the same as for a measurement made without charge breeding, but scaled by a survival fraction:

$$\xi(q) \equiv 2^{-t_{CB}/t_{1/2}}\,\eta_{pop}(q)\,\varepsilon^q_{HCI}/\varepsilon_{SCI} \ , \tag{4.5}$$

which accounts for additional radioactive decay losses during the time taken to charge breed the ions $2^{-t_{CB}/t_{1/2}}$, the fraction of ions $\eta_{pop}(q)$ in the $q+$ charge state after charge breeding, and the losses due to HCI related efficiencies ε^q_{HCI} (Equation 4.7) as compared to the SCI related efficiencies ε_{SCI} (Equation 4.6). The efficiencies:

$$\varepsilon_{SCI} = \varepsilon_{RFQ}\,\varepsilon_{trans}\,\varepsilon_{PTMS}\,\varepsilon_{det} \ , \tag{4.6}$$

$$\varepsilon^q_{HCI} = \varepsilon_{RFQ}\,\varepsilon^q_{trans}\,\varepsilon^q_{PTMS}\,\varepsilon^q_{det}\,\varepsilon_{inj}\,\varepsilon_{ext} \ , \tag{4.7}$$

describe how well the system is optimized for a charge state q. This includes the efficiency for bunching and cooling in the RFQ ε_{RFQ}, transportation through the respective beam lines (Figure 3.2) ε_{trans}, all efficiencies related to the PTMS process ε_{PTMS}, detection ε_{det}, and the additional HCI efficiencies for injection ε_{inj} into and extraction ε_{ext} from the EBIT. Charge-state dependent efficiencies are marked with a superscript ε^q.

The number of ions arriving at MPET each cycle χ can now be defined in terms of the production yield of ions from ISAC, denoted Y_p in ions per second, the cycle length t_{cycle}, the SCI efficiency ε_{SCI}, and the HCI survival fraction $\xi(q)$ from Equation 4.5:

$$\chi_{SCI} = Y_p\,t_{cycle}\,\varepsilon_{SCI} \tag{4.8a}$$

$$\chi_{HCI}(q) = \chi_{SCI}\,\xi(q) \ . \tag{4.8b}$$

It is worth noting that since $\xi(q) \leq 1$, $\chi_{HCI}(q)$ will always be less than or equal to

χ_{SCI}.

When comparing a measurement made with HCI to a measurement made with SCI, three possible scenarios arise:

- more than one ion per cycle arrives at the MPET: $\chi_{SCI}, \chi_{HCI} \geq 1$
- more than one ion per cycle arrives at the MPET for SCI only: $\chi_{HCI} < 1 \leq \chi_{SCI}$
- less than one ion per cycle arrives at the MPET: $\chi_{SCI}, \chi_{HCI} < 1$

Making the appropriate substitution for the number of detected ions per cycle from Equations 4.4 and 4.8 into Equation 4.3 the complete description of the precision gained is:

$$G_{HCI} = q\sqrt{\frac{N_{det}^{HCI}}{N_{det}^{SCI}}} = \begin{cases} q & \text{if } \chi_{SCI}, \chi_{HCI} \geq 1 & \text{(4.9a)} \\ q\sqrt{Y_p \, t_{cycle} \, \varepsilon_{SCI} \xi(q)} & \text{if } \chi_{HCI} < 1 \leq \chi_{SCI} & \text{(4.9b)} \\ q\sqrt{\xi(q)} & \text{if } \chi_{SCI}, \chi_{HCI} < 1 & \text{(4.9c)} \end{cases}$$

In the first case, all losses in the system with either HCI and SCI are compensated for by a high production yield, allowing the full factor of q to be exploited. This is usually the case with isotopes in a stable beam. In the second case, the production yield is enough for an SCI measurement to have more than one ion at the MPET every cycle, but charge breeding introduces losses after the surplus number of ions from an SCI measurement $Y_p \, t_{cycle} \, \varepsilon_{SCI}$ is depleted. Finally, in the third case, the production yield is too low for one ion per cycle to arrive at the MPET with either SCI or HCI: all additional losses introduced by charge breeding impact the precision gained.

Equation 4.9 fully encompasses all of the independent parameters that affect the benefit of charge breeding for PTMS with radioactive ions. Careful evaluation of G_{HCI} provides a realistic estimate of the precision gained under the given conditions. Many of the relevant terms, like the yield χ_{SCI} and the efficiencies ε_{SCI} and ε_{HCI}, are independent of the actual charge-breeding process and give an indication of how well tuned the experimental apparatus must be in order to perform a precision measurement. The only term that is affected by the charge breeding is the survival fraction $\xi(q)$.

The rest of the chapter discusses how $\xi(q)$ can be maximized with an appropriate choice of charge-breeding conditions. Since Equation 4.9a is trivial, and Equation 4.9b can be obtained by scaling Equation 4.9c by $\sqrt{Y_p \, t_{cycle} \, \varepsilon_{SCI}}$, only Equation 4.9c is discussed. Furthermore, since the efficiencies serve only as a scaling (which can be factored in as needed) and are independent of the charge-breeding conditions, the following discussion assumes negligible losses, and assumes $\varepsilon_{HCI} = \varepsilon_{SCI} = 1$. The resulting expression to be evaluated is:

$$G_{HCI} = q\sqrt{2^{-t_{CB}/t_{1/2}} \, \eta_{pop}(q)} \; . \tag{4.10}$$

The optimization of G_{HCI} in this form balances the seeking of higher charge states with the losses introduced by additional radioactive decays and distributing the ions over many charge states. Once optimized, both the yields and efficiencies can be folded in according to Equations 4.5 and 4.9 to determine the actual precision gain (for an example see Section 4.3).

4.2.2 Evolution of the Precision Gain G_{HCI} with Various Charge-Breeding Parameters

The precision gain, as defined in Equation 4.10, can be calculated for any situation in which the half-life $t_{1/2}$, the charge state q, the charge-breeding time t_{CB}, and the fraction of ions in the given charge state $\eta_{pop}(q)$ are known. Experimentally, t_{CB} and q are choices that result in a particular fraction of ions, which can be determined by performing time-of-flight identification on the extracted ion bunch (Section 3.2). Although it is possible to perform this exercise and calculate G_{HCI} for various charge states and charge-breeding conditions, it is much simpler and equally informative to use the fraction of ions as determined by CBSIM in the calculation of G_{HCI}.

Figure 4.4 displays the evolution of G_{HCI} taken from the data in Figure 4.3 with an electron-beam current density of $J = 50$ A cm^{-2} for ^{74}Rb with a half-life $t_{1/2} = 65$ ms. At these settings, threshold charge breeding has populated the 27+ almost exclusively once equilibrium is reached, yet a mass measurement on charge state 27+ would not offer the optimal precision gain. Rather, the maximum precision gain is $G_{HCI}^{MAX} \approx 7 \neq q$ for a measurement made on the 17+ charge state. This is a
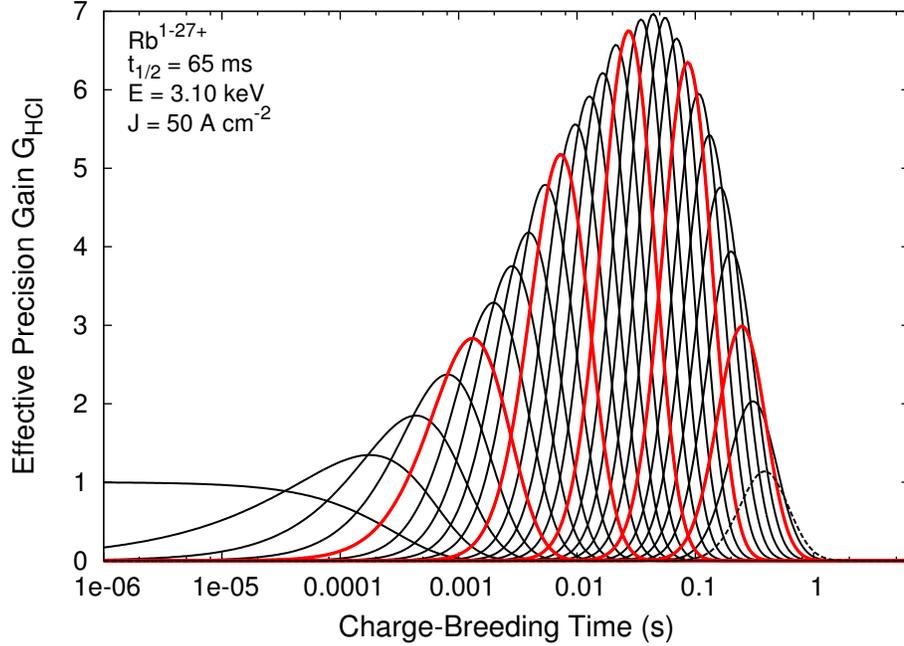
Figure 4.4: Evolution of $G_{HCI}(q, t_{CB}, 50 \text{ A cm}^{-2}, 3.1 \text{ keV})$ for $^{74}\text{Rb}^{q+}$ ($t_{1/2} = 65$ ms). The maximum precision gain occurs in the 17+ charge state for $t_{CB} \approx t_{1/2}$. When the charge-breeding time exceeds the half-life, G_{HCI} falls off due to losses from radioactive decay. Every fifth charge state (bold red) and the maximum charge state (dashed black) are emphasized to guide the eye.

consequence of the amount of time it takes to reach the equilibrium distribution: approximately two seconds or more than 30 half-lives. As a result, a measurement made with the 27+ charge state is comparable to or worse than a measurement made without charge breeding. This maximum precision gain in the 17+ charge state occurs after a charge-breeding time that is just less than one half-life.

Increasing the current density speeds up the charge-state evolution, as seen in Figures 4.5 and 4.6 for $J = 500$ and 5000 A cm^{-2}, so that higher charge states can be reached within a few half-lives. In the first plot, Figure 4.5, the optimal charge state is 27+ after a charge-breeding time of about 100 ms. The maximum precision gain of 15 is a result of the threshold charge breeding and higher current density
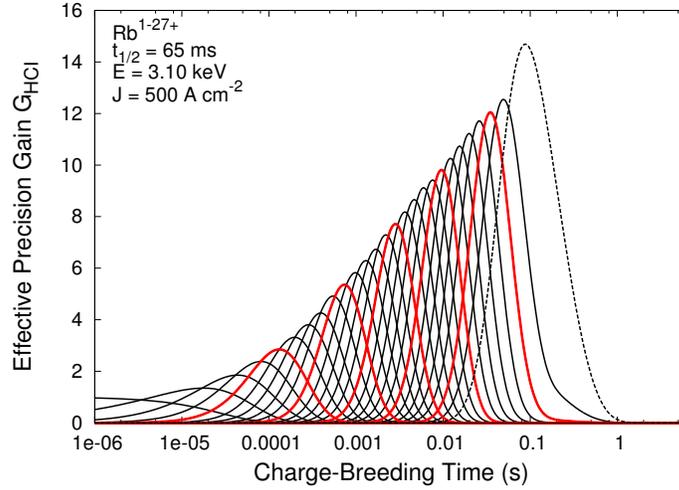
Figure 4.5: Evolution of $G_{HCI}(q, t_{CB}, 500 \text{ A cm}^{-2}, 3.1 \text{ keV})$ for $^{74}\text{Rb}^{q+}$ ($t_{1/2} = 65$ ms). The maximum precision gain occurs in the 27+ charge state since the increased current density makes threshold effects advantageous before radioactive decay-losses diminish G_{HCI}. Every fifth charge state (bold red) and the maximum charge state (dashed black) are emphasized to guide the eye.
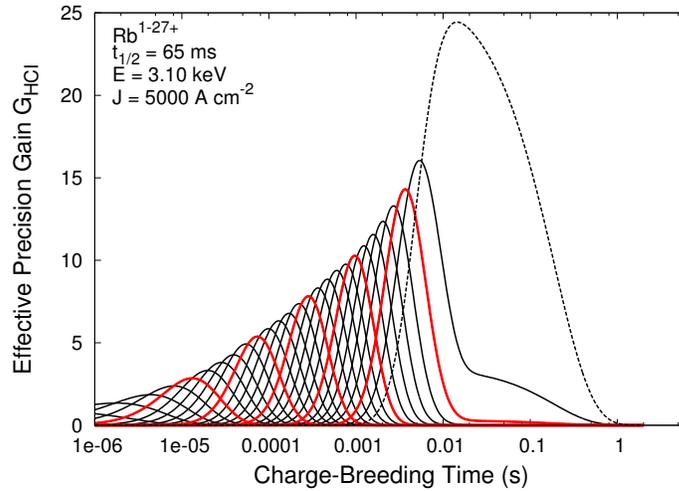
Figure 4.6: Evolution of $G_{HCI}(q, t_{CB}, 5000 \text{ A cm}^{-2}, 3.1 \text{ keV})$ for $^{74}\text{Rb}^{q+}$ ($t_{1/2} = 65$ ms). The maximum precision gain occurs in the 27+ charge state and the full advantage of the threshold effect is available resulting in $G_{HCI} \approx q$. Every fifth charge state (bold red) and the maximum charge state (dashed black) are emphasized to guide the eye.

allowing the Ne-like configuration to be reached without substantial decay losses. In Figure 4.6, the optimal charge state is still 27+, but after a charge breeding time of about 15 ms. This substantial difference in charge-breeding time results in far less radioactive decays during the charge breeding. The full advantage of threshold charge breeding is made possible, resulting in a $G_{HCI} = 24 \approx q$.

4.2.3 Optimization of All Charge-Breeding Parameters

The goal of simulating the precision gained by producing HCI under different charge-breeding conditions is to provide insight into the optimal way to operate the EBIT for PTMS. The effect of charge breeding with different electron-beam energies and current densities can be studied by carrying out simulations for a full set of G_{HCI} versus t_{CB}; however, this task would be tedious due to the number of variables and amount of data to consider. Instead of tracking the trends for all charge states at all charge-breeding times, the problem can be reduced by only considering the maximum $G_{HCI}^{MAX}(J,E)$, the optimum charge state $q_{opt}(J,E)$ and the optimium charge-breeding time $t_{opt}(J,E)$ that result in this gain:

$$G_{HCI}^{MAX}(J,E) = G_{HCI}(q_{opt}, t_{opt}, J, E) \ . \tag{4.11}$$

As a function of only two variables, this information is easily summarized in an intensity plot with the electron-beam energy on the x-axis, the electron-beam current density on the y-axis, and the maximized precision gain represented by a colour gradient. The optimal charge state and charge-breeding time can be superimposed on the intensity plot as contours, fully specifying the ideal charge breeding settings as a function of electron-beam energy and current density. This is shown in Figures 4.7 and 4.8 for contours with q_{opt} and t_{opt} respectively. A practical range of electron-beam energies (1 to 6 keV) and electron-beam current densities (50 to 5000 A cm^{-2}), from the discussion of the TITAN EBIT in Section 3.2, were used to create the intensity plots. A choice of a particular electron-beam energy and current density means that G_{HCI}^{MAX}, q_{opt}, and t_{opt} can be identified. For example, at a current density of 50 A cm^{-2} and energy of 3.1 keV, the optimal charge state is $q = 17+$ after a charge-breeding time between 40 and 60 ms, in agreement with Figure 4.4. At a current density of 500 A cm^{-2} and energy of 3.1 keV, the optimal
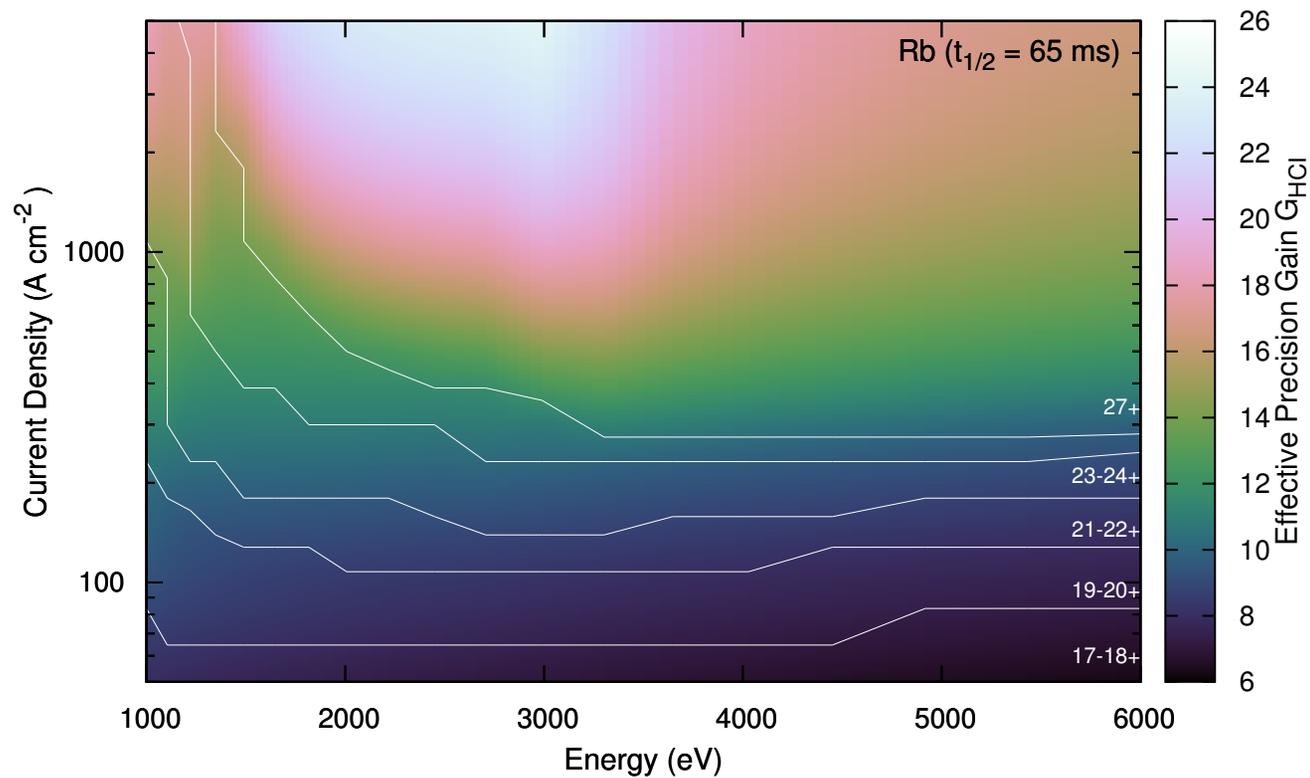
Figure 4.7: Intensity plot of $G_{HCI}(q_{opt}, t_{opt}, J, E)$ for ^{74}Rb$^{q_{opt}+}$ with contours specifying q_{opt}. In this range of typical electron-beam energies and current densities, charge states $q = 17+$ or greater provide the maximum precision gain. As the electron-beam current density increases, so does G_{HCI}^{MAX}, and after a certain critical current density (here about 2000 A cm^{-2}) it becomes possible to take advantage of the threshold effect (Ne-like closed electronic shell and an electron-beam energy of 3.1 keV) to maximize the precision gain reaching $G_{HCI} \approx q = 27+$.
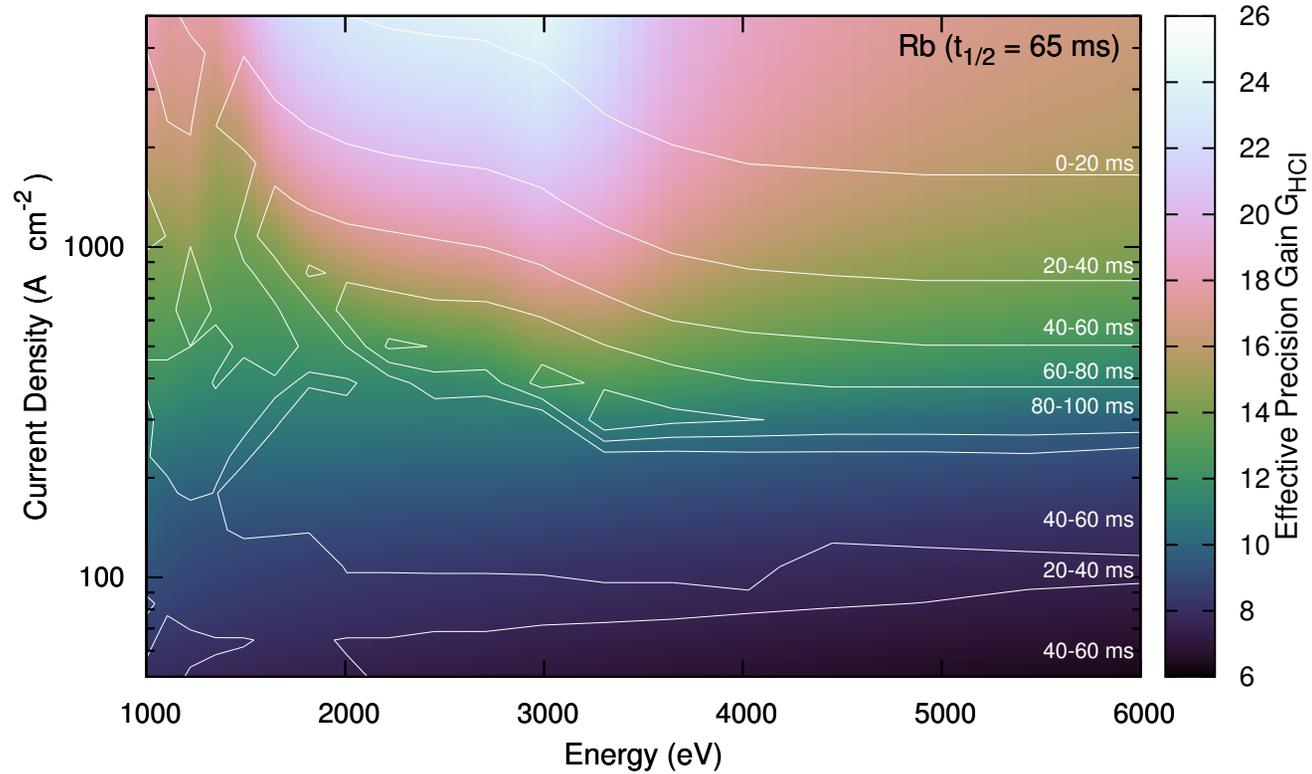
Figure 4.8: Intensity plot of $G_{HCI}(q_{opt}, t_{opt}, J, E)$ for ^{74}Rb$^{q_{opt}+}$ with contours specifying t_{opt}. In this range of typical electron-beam energies and current densities, the optimal charge-breeding time never exceeds two half-lives, with most lying in the range $t_{opt} = \frac{1}{2}t_{1/2}$ to $t_{1/2}$. As the electron-beam current density increases, threshold charge breeding to Ne-like ^{74}Rb^{27+} becomes advantageous and the charge-breeding time decreases.

charge state is $q = $27+ after a charge-breeding time between 80 and 100 ms, which is in agreement with Figure 4.5.

From these intensity plots some general trends for optimizing the charge breeding of ^{74}Rb ($t_{1/2} = 65$ ms) for PTMS are apparent:

1. For any given electron-beam energy in the range shown, G_{HCI}^{max} increases with the current density.

2. At high electron-beam current densities, threshold charge breeding to the Ne-like configuration creates a clear global maximum in G_{HCI}.

3. At lower electron-beam current densities, lower electron-beam energies are favoured.

4. The optimal charge-breeding time does not exceed 2 half-lives.

5. The optimal charge state is always $q \geq 17+$, which corresponds to an empty 3d electronic shell, or Ca-like electronic configuration.

The most important of these trends is that the electron-beam current density is the limiting factor in maximizing the precision gained for PTMS with highly charged, radioactive ions. With the potential to increase the precision gained by more than a factor of four, experimentally this means that the current density should be optimized to be as large as possible. Once this has been accomplished, and the current density is known, the optimal electron-beam energy, charge state, and charge-breeding time can all be determined; fully specifying the optimal conditions for charge breeding and the resulting maximum precision gain.

4.2.4 Trends in the Maximum Precision Gain

Experiments often come with undesired constraints, which may make the optimal conditions, as discussed in the previous section, unattainable. For this reason, it is worth exploring what G_{HCI}^{MAX} are possible subject to certain constraints. For example, once the electron-beam current density has been maximized and determined to be J_{max}, it is no longer necessary to consider the gain that would result from values of J. Instead, a two-dimensional slice can be taken at a constant current density allowing $G_{HCI}^{MAX}(J_{max}, E)$ to be graphed as a function of the electron-beam energy.
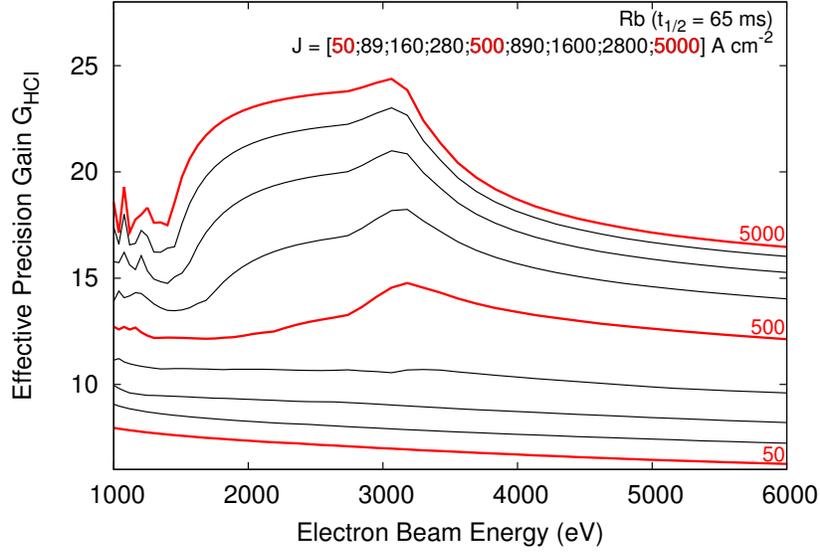
Figure 4.9: Plot of $G_{HCI}(q_{opt}, t_{opt}, J=50$ to 5000 A cm^{-2}, E) for ^{74}Rb$^{q_{opt}+}$ ($t_{1/2} = 65$ ms). Each curve represents a slice from Figure 4.7 at constant electron-beam current density. As J increases so does G_{HCI} and the threshold effect at $E = 3.1$ keV provides a significant advantage over other electron-beam energies. The curves for $J = 50$, 500, and 5000 A cm^{-2} are highlighted (red) to guide the eye.

Figure 4.9 shows a two-dimensional plot of these slices for a set of electron-beam current densities ranging from $J=50$ to 5000 A cm^{-2}.

Another possible experimental constraint is on the charge state. For example, if threshold charge breeding is required to separate the desired isotopes from con-tamination (Section 4.1.3) the charge state must be fixed. Since Figure 4.9 only considers the optimal charge state, the procedure can be extended to identifying $G_{HCI}^{MAX}(q, t,_{CB}J, E)$ for all charge states. Then, $G_{HCI}^{MAX}(q, t_{opt}, J_{max}, E)$ can be plotted against the electron-beam energy for each charge state. For a known electron-beam current density, this type of graph provides the most information as it contains G_{HCI}^{MAX} for all charge states and all energies.

In Figure 4.10, this has been done for $J_{max} = 500$ A cm^{-2}, where the maximum precision gain from this plot represents $G_{HCI}(q_{opt}, t_{opt}, J_{max}, E)$. Starting with
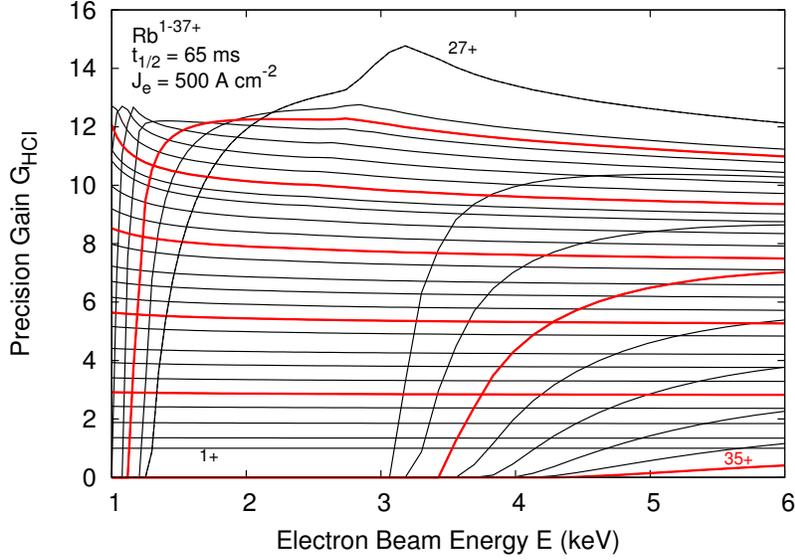
Figure 4.10: Plot of $G_{HCI}(q = 1 - 37+, t_{opt}, J = 500$ A cm$^{-2}, E)$ for ^{74}Rb^{1-37+} ($t_{1/2} = 65$ ms). For a known electron-beam current density, this plot provides the maximum G_{HCI} for every charge state. At all energies, $G_{HCI} = 1$ for $q = 1+$ and as the charge state increases up to $q = 27+$, G_{HCI} also increases. After an electron-beam energy of 3.1 keV is reached higher charge states become accessible, however G_{HCI} begins to decrease with the charge state all the way to zero for $q = 36+$ and 37+ (see text). The curve for every 5th charge state (bold red) is highlighted to guide the eye.

$q = 1+$ and a flat $G_{HCI}^{MAX} \approx 1$, the gain increases with increasing charge state up to 27+. At electron-beam energies greater than 3.1 keV, the Ne-like shell is opened allowing charge states higher than 27+ to be populated; however, the fraction of ions in these charge states is too small to improve G_{HCI}^{MAX}, which starts to decrease with increasing charge states. Finally, G_{HCI}^{MAX} is zero for $q = 36+$ and 37+ since the electron-beam energy does not exceed the ionization potential of $I_p(q = 35+)$ and no ions occupy these charge states. This plot readily provides information on the attainable G_{HCI}^{MAX} if a certain charge state is required for an experiment.
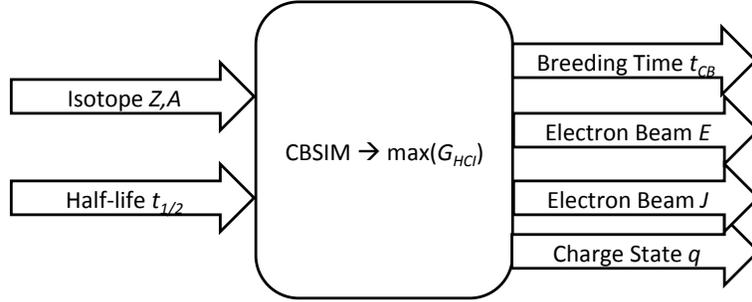
Figure 4.11: Schematic outline of the optimization procedure for G_{HCI}. By specifying the isotope of interest and its half-life, the optimization provides the optimal q, t_{CB}, E, and J, fully specifying the optimal charge-breeding conditions for PTMS with highly charged, radioactive ions.

4.2.5 Schematic Outline of the Optimization Procedure

The numerical optimization procedure (Figure 4.11) using CBSIM to arrive at the intensity plots and all of the intermediary steps is:

1. Populate the precision gain using $\eta_{pop}(q, Jt, E)$ from CBSIM:

$$\implies G_{HCI}(q, t_{CB}, J, E) = \sqrt{2^{-t_{CB}/t_{1/2}} \eta_{pop}(q, Jt, E)}$$

2. For each charge state, electron-beam energy, and electron-beam current density, maximize $G_{HCI}(q, t_{CB}, J, E)$ with respect to time and store the optimal time:

$$\implies G_{HCI}^{MAX}(q, J, E) = G_{HCI}(q, t_{opt}, J, E)$$
$$\implies t_{opt}(q, J, E)$$

3. For each electron-beam energy and current density, maximize $G_{HCI}^{MAX}(q, J, E)$ with respect to the charge state, determine the optimal time that corresponds to the charge state, and store the optimal charge state:

$$\implies G_{HCI}^{MAX}(J, E) = G_{HCI}(q_{opt}, t_{opt}, J, E)$$
$$\implies t_{opt}(J, E) = t_{opt}(q_{opt}, J, E)$$

$$\implies q_{opt}(J, E)$$

Thus, by specifying the isotope of interest and its half-life, performing a transformation to a variable sensitive to the charge-breeding conditions and specific to PTMS, and simulating the precision gained, all of the charge-breeding parameters can be optimized for PTMS with highly charged, radioactive ions. This stage in preparation for an experiment with RIB allows for a theoretical start to the optimization of charge breeding for PTMS and reduces the amount of time required during an experiment. An example of how this procedure can be used for planning an experiment is provided in the following case study.

4.3   A Case Study on ^{74}Rb

The ^{74}Rb nuclide is an extremely neutron-deficient nuclide that lies near the proton drip line of the nuclear chart. With a half-life of only 65 ms, it undergoes superallowed nuclear β-decay to ^{74}Kr. The mass difference, or Q-value, between the mother and daughter nuclides in this reaction plays an important role in discriminating between theoretical models of the isospin symmetry breaking correction δ_c [80]. As a result, the mass of ^{74}Rb has been the subject of a number of investigations [21–24] that have aimed for higher and higher precision. The experimental challenges in making a high precision measurement on ^{74}Rb lie in its short-half life and relatively modest yields. This makes it an excellent candidate for a measurement in high charge states. Despite the number of measurements that have been made thus far, improvements to the precision carry enough importance that the Experiments Evaluation Committee (EEC) at TRIUMF has approved a proposal to measure the masses of both ^{74}Rb and ^{74}Kr to even higher precision by using high charge states at TITAN [81].

When determining which charge state should be used for the measurement, Figures 4.7 and 4.8 provide full details on the optimal precision gain at the corresponding EBIT settings. The current densities of 110 and 2700 A cm^{-2}, which represent extreme values calculated in Section 2.3.2, offer different optimal charge-breeding conditions and precision gains. At an electron-beam current density of 110 A cm^{-2}, the optimal charge breeding for PTMS for low electron-beam energies and charge-breeding times on the order of 0.5 $t_{1/2}$. The optimal charge state

Table 4.1: Expected values used in determining the true precision gain G_{HCI} for a measurement on highly charged ^{74}Rb ions

^{74}**Rb Experiment Variables**	Symbol	Value	Source
Cycle length	t_{cycle}	$3t_{1/2}$	typical
SCI efficiency	ε_{SCI}	0.1	estimated
HCI efficiency	ε_{HCI}	0.0009	[81]
Production yield (ions/s)	Y_p	10^3	[81]
SCI yield at MPET (ions/cycle)	$\chi_{SCI} = Y_p\, t_{cycle}\, \varepsilon_{SCI}$	19.5	calculated
HCI yield at MPET (ions/cycle)	$\chi_{HCI} = \chi_{SCI}\xi(q)$	< 1	calculated
Scaling factor	$\sqrt{\chi_{SCI}\varepsilon_{HCI}/\varepsilon_{SCI}}$	0.42	calculated

is 19+ resulting in $G_{HCI}^{MAX} \approx 9$. In this case, threshold charge breeding does not offer any advantages. At 2700 A cm^{-2}, however, threshold charge breeding to the Ne-like configuration becomes advantageous for an electron-beam energy of 3.1 keV, resulting in $G_{HCI}^{MAX} \approx 21$. In order to take full advantage of the threshold charge breeding and obtain $G_{HCI}^{MAX} \approx q$, an even greater electron-beam current density would be needed.

The actual precision gained from performing this measurement depends on the production yield and expected efficiencies. Expected values at the time of the proposal are found in Table 4.1. Since the expected SCI yield at the MPET $\chi_{SCI} > 1$, and the expected HCI yield at the MPET $\chi_{HCI} < 1$, the true G_{HCI} is given by Equation 4.9b. The calculated values must be scaled by $\sqrt{\chi_{SCI}\varepsilon_{HCI}/\varepsilon_{SCI}} = 0.42$. Taking this into account for the respective current densities, the expected precisions gained are approximately a factor of 4 and 10.

This information reiterates the importance of maximizing the electron-beam current density for experiment. Based on estimates of the effective electron-beam current density at TITAN (see Section 5.3.4 for details), $J \approx 100$ A cm^{-2}. For the proposed measurement, this implies that TITAN is ready to perform the measurements on charge state 19+; however, in order to pursue the full advantages of threshold charge breeding to the 27+ Ne-like shell closure, including maximizing the precision gained while allowing for isobaric separation of possible contaminant

ions, further improvements to the current density are required. Further discussion of the experimental electron-beam current density and possible improvements are discussed in Chapters 5 and 7.

4.4   Summary

Two open concerns in the field of PTMS with highly charged, radioactive ions have been addressed in this chapter for the first time: the first was the lack of a quantitative description of the benefit of charge breeding for PTMS with radioactive ions; and the second was the need of a systematic way to optimize the charge-breeding conditions before receiving radioactive ions for measurement. For the former, the precision gain G_{HCI} was defined to reflect the relative precision gain by using highly charged ions in a measurement instead of singly charged ions. This factor reflected the linear increase with the charge state as well as accounted for all parameters that would affect the statistical precision of a measurement. After separating this precision gain into three different cases that reflected whether the production yield was able to fully, partially, or unable to compensate for efficiency and radioactive decay losses, only the terms that depended on the charge-breeding conditions were extracted to assist in the optimization of G_{HCI}.

Based on the intensity plots of $G_{HCI}(J,E)$ there are two steps in optimizing the charge breeding for any given measurement. Since the maximum precision gain increases with the electron-beam current density at all electron-beam energies, optimal charge breeding will take place for the maximum possible current density. Since practical limitations will impose an upper limit, it is important to maximize and determine the operational current density. Once this has been accomplished the optimal charge-breeding conditions are fully determined from the intensity plots and contours that provide the optimal electron-beam energy, charge-breeding time and charge state.

Chapter 5

Systematic Charge-Breeding Studies

In order to gain a deeper understanding of the charge-breeding process, theoretical descriptions (Section 2.3) and simulations (Chapter 4) have to be complemented with experimental studies. In this chapter the theory that was used in the development of CBSIM is compared to experimental findings. The results will help identify under what conditions the findings from Chapter 4 are applicable and will allow for refinements that improve the compatibility between theory and experiment. Once the theory and simulations accurately represent the experimental conditions, the qualitative and systematic approach that was developed to optimize the charge-breeding conditions for PTMS with highly charged, radioactive ions can be applied experimentally.

The chapter begins with an overview of the theoretical description of charge breeding in an electron beam (Section 2.3.1), the properties of the electron beam (Section 2.3.2), and some testable predictions for producing experimental charge-state distributions. The variables that theoretically have the greatest impact on the charge-breeding conditions are discussed throughout the overview. Based on this discussion, the experimental procedure is defined and described. This is followed by a quantitative way to summarize an experimental charge-state distribution by analyzing time-of-flight distributions, which provides a simple way to compare different charge-breeding conditions. Experimental data were taken with the EBIT

at TITAN under various charge-breeding conditions and compared to expectations. The findings, including deviations from the expected results, are discussed along with possible causes. A comparison of an experimental charge-state distribution with those produced in CBSIM is provided. Finally, additional investigations and improvements are suggested.

5.1 Theoretical Expectations for Charge Breeding in an Electron Beam

In order to define an experimental procedure that can be used to compare experiment and theory, it is necessary to review the theoretical descriptions of charge breeding in an electron beam (Section 2.3) and propose some trends that can be tested experimentally. All of the relevant charge-changing processes and charge-breeding parameters were combined in the set of coupled differential equations (Equation 2.5) that describes the rate of change of the number of ions N_q in the charge state $q+$:

$$\frac{dN_q}{dt} = J \, f_{e;q} \left(\sigma_{q-1}^{EI} \, N_{q-1} - \sigma_q^{EI} \, N_q - \sigma_q^{RR} \, N_q + \sigma_{q+1}^{RR} \, N_{q+1} \right) \ . \qquad (5.1)$$

From this equation, the important charge-breeding parameters were identified: these are the electron-ion overlap factor $f_{e;q}$, the electron-beam current density J, the cross sections $\sigma_q(E)$ which depend on the electron-beam energy E, and the interaction time t (i.e., charge-breeding time t_{CB}).

Each of these parameters is discussed below in the context of their expected effect on an experimentally produced charge-state distribution. Two assumptions that were used in the design of the experimental investigations are discussed. These assumptions are a direct result of comparing CBSIM to experimental conditions and they direct the studies towards specific charge-breeding parameters. The theoretical properties of the charge-breeding parameters of interest are also provided. These are the properties that will be tested experimentally in order to determine the compatibility between theory and experiment. The provided assumptions and properties are combined to give one concise testable prediction which forms the foundation for the experimental studies.

Assumption I: There is perfect overlap between the electron beam and the ions

The electron-ion-overlap factor $f_{e;q}$ depends on the fraction of ions inside the electron beam, which not only depends on the electron-beam properties, but also on the initial conditions of the trapped ions. In an ideal scenario there would be perfect overlap between the electron beam and the ions ($f_{e;q} = 1$). One way to obtain this, regardless of the electron-beam properties, is to deliver a cooled ion bunch to the trapping region on axis with the electron beam with no angular momentum [82]. As CBSIM considers the evolution of charge states for ions in an electron beam and does not account for any time ions might spend outside of the electron beam, $f_{e,q} = 1$ will be assumed for the experimental investigations and the possible consequences of this assumption will be discussed.

Assumption II: The gain factor G_{HCI} is more sensitive to changes in the electron-beam current density than the electron-beam energy

The electron-beam energy E and resulting cross sections $\sigma_q(E)$ couple the rate equations in Equation 5.1. Since the electron-beam energy determines the magnitude of the cross sections, it is responsible for the fraction of ions in a given charge state throughout the evolution. In contrast, the electron-beam current density J is a scaling factor in Equation 5.1, and only changes the rate of evolution. Chapter 4 discussed the effects of changing both J and E on the factor G_{HCI} (Figure 4.9); while changes in the electron-beam current could increase the expected precision gain G_{HCI} by more than a factor of three, the electron-beam energy only provided improvements of up to 50% for threshold charge breeding, and marginal improvements otherwise. As a result, the electron-beam current density is expected to play a more crucial role than the electron-beam energy for improving PTMS with highly charged, radioactive ions. For experimental studies, the energy can be fixed to some reasonable value (e.g., a threshold energy from Section 4.1.3).

Property I: The charge-state evolution scales with the product of the electron-beam current density and the charge-breeding time

Another way to write the rate equations, seen above in Equation 5.1, is by rearranging the scaling factors J and $f_{e;q}$ and grouping them with time in the derivative:

$$\frac{dN_q}{d(J\,f_{e;q}\,t)} = \sigma^{EI}_{q-1}\,N_{q-1} - \sigma^{EI}_q\,N_q - \sigma^{RR}_q\,N_q + \sigma^{RR}_{q+1}\,N_{q+1} \ .$$

This rearrangement emphasizes the property that J, $f_{e;q}$, and t play the same role in the evolution of charge states. Operating under the assumption $f_{e;q} = 1$ (**Assumption I**), the resulting evolution of charge states scales with the product of J and t_{CB}, or J-time.

Property II: The electron-beam current density is proportional to both the electron-beam current and the magnetic field strength in the trapping region

In order to determine how to produce various charge-breeding conditions, the relevant properties of the electron beam from Section 2.3.2 are reintroduced. The electron-beam current density, defined in Equation 2.9:

$$J = \frac{0.8\,I[\mathrm{A}]}{\pi\,r_H[\mathrm{cm}]^2} \ ,$$

depends on the electron-beam current I and the Herrmann radius of the electron beam r_H in a simple proportionality: $J \propto I\,r_H^{-2}$. The Herrmann radius was provided in Equation 2.7:

$$r_H = r_b\sqrt{\frac{1}{2} + \frac{1}{2}\sqrt{1 + 4\left(\frac{8kT_c r_c^2 m_e}{e^2 r_b^4 B^2} + \frac{B_c^2 r_c^4}{B^2 r_b^4}\right)}} \ ,$$

where T_c is the temperature of the cathode; B_c is the residual magnetic field at the cathode; r_c is the cross-sectional radius of the cathode's emitting surface; k is the Boltzmann constant; m_e is the mass of the electron; e is the charge of the electron; and r_B is the Brillouin radius (Equation 2.6):

$$r_b[\mathrm{m}] = \frac{1.5 \times 10^{-4}}{B[\mathrm{T}]}\sqrt{\frac{I_e[\mathrm{A}]}{\sqrt{E[\mathrm{keV}]}}} \ .$$

Since the cathode temperature and radius are fixed, the best way to control the

55

electron-beam radius is with the magnetic field at the cathode or in the trapping region. For typical operation, it is best to minimize the residual magnetic field at the cathode, so the magnetic field strength in the trapping region is a more appropriate variable to change.

The terms in brackets in the Herrmann radius are much larger than unity for the typical values considered (see Section 2.3.2), consequently, the Herrmann radius depends on B according to $r_H \propto \frac{1}{\sqrt{B}}$. Substituting this into the definition of the electron-beam current density gives:

$$J \propto I\,B\ .$$

It is worth noting that a change in the electron-beam current also changes the Brillouin radius, however, this has a negligible effect on the Hermann radius for the typical values discussed in Section 2.3.2. For example, for $T_c = 1470$ K, $r_c = 0.00170$ mm, $B = 4.5$ T, $E = 2.5$ keV, changing the electron-beam current by more than an order of magnitude from $I = 10$ mA to $I = 100$ mA changes the Herrmann radius by less than 2% for all values of B_c.

Result $\Rightarrow$ a unique charge-state distribution is produced for a unique combination of electron-beam current, magnetic field, and charge-breeding time

The above assumptions from CBSIM and expected properties derived from a theoretical description of charge breeding in an electron beam combine to give the following concise statement about charge-state evolution: a unique charge-state distribution is produced for a unique combination of electron-beam current, magnetic field, and charge-breeding time. To determine whether or not this condition is satisfied experimentally, different tests can be performed by producing charge-state distributions under various charge-breeding conditions and comparing the results. Two questions that will be addressed experimentally are the following:

- can a change in the electron-beam current or the magnetic field strength change the resulting charge-state distribution in a predictable way?

- are charge-state distributions that were produced under a constant J-time, or more specifically a constant product $I \cdot B \cdot t_{CB}$, unique?

The experimental procedure for these investigations is described in the following section.

5.2 Experimental Procedure for the Production, Detection, and Analysis of Charge-State Distributions

5.2.1 Production and Detection of Charge-Bred Ions

Stable Rb isotopes were obtained from a surface ion source below the RFQ in the TITAN experimental set-up (Figure 3.2). The ions were accumulated in the RFQ for 100 ms, and were extracted at a beam transport energy of 2.0 keV along the same path as ions delivered from ISAC (Section 3.2). The potentials that were applied to the trap drift tubes were optimized to maximize the capture of ions into the EBIT (i.e., biased to approximately 2 kV). For the capture process, the potential on the first trapping drift tube (Figure 3.3 C1) was raised to create an axial potential barrier once the ions were inside the segmented drift tube (Figure 3.3 S1-8). The trapped ion bunch was radially confined by the electron beam, which had an energy of $E = 3.1$ keV. The electron-beam energy was kept constant for the duration of the experiments. After allowing the charge-state evolution to occur for a certain charge-breeding time t_{CB}, the ions were extracted from the EBIT, directed through the beam line, and analyzed.

The charge-breeding conditions were varied by changing the electron-beam current I, the magnetic field strength in the trapping region B, and the charge-breeding time t_{CB}. The components responsible for changing these parameters were discussed in Section 2.3.1 and are briefly described here. To change the electron-beam current, the bias of the focus electrode was varied to change the number of electrons being extracted from the cathode. To change the magnetic field in the trapping region, the current in the superconducting coils was varied using a power supply. This allowed the adjustment of the magnetic field strength. Finally, the charge-breeding time was changed by adjusting the time interval between injecting and extracting the ion bunch into / out of the EBIT.

After charge breeding, the extracted ions were transported along the beam line

towards the MPET and a micro-channel plate detector was inserted into the bend in the beam line (Figure 3.2). The ions had velocities that depended on their mass-to-charge ratio m/q and this created a separation in the time of flight T of different charge states to reach the detector according to Equation 3.1:

$$T = \sqrt{\left(\frac{m}{q}\right) \frac{d^2}{2U}} \quad,$$

where d is the distance from the EBIT to the detector and U is the potential that was applied to the segmented drift tube in the EBIT. The time of flight was recorded, and time-of-flight spectra, like the ones shown in Section 3.2, were created for various charge-breeding conditions. This allowed for a qualitative description of the charge-state distributions.

A time-of-flight spectrum of charge-bred ^{85,87}Rb ions is shown in Figure 5.1 for an electron-beam current of $I = 100$ mA, a magnetic field of $B = 4.28$ T, and a charge-breeding time of $t_{CB} = 5$ ms. In this spectrum, charge states $q = 4+$ through 14+ are marked from right to left. Since ions with higher charge states move faster through the beam line, they have a shorter time of flight and appear closer to the y-axis. The charge-state distribution peaks for $q = 10+$, and charge states above $q = 14+$ are hidden in peaks resulting from residual gas (i.e., H, C, N, O) ions. These ions have a shorter time of flight due to their lower mass-to-charge ratio. A double-peak structure is present in the data, where each dominant peak has a secondary peak at slightly larger times. This double-peak structure of the ^{85,87}Rb spectrum could have been caused be a number of effects, including time-of-flight separation of the two isotopes, a detector effect caused by too many ions saturating the micro-channel plate, or a signal effect caused by reflections in the cables. These hypotheses were investigated, but none were confirmed experimentally, and no further attempts were made as the double-peak structure is inconsequential for the experimental investigations herein.

Decreasing the charge-breeding time shifts the charge-state distribution to lower charge states and thus appears as a longer time of flight, as seen in Figure 5.2 for $t_{CB} = 3.75$ ms and $t_{CB} = 5$ ms. An envelope, drawn through the peak number of counts in each charge state, assists in comparing the charge-state distributions.
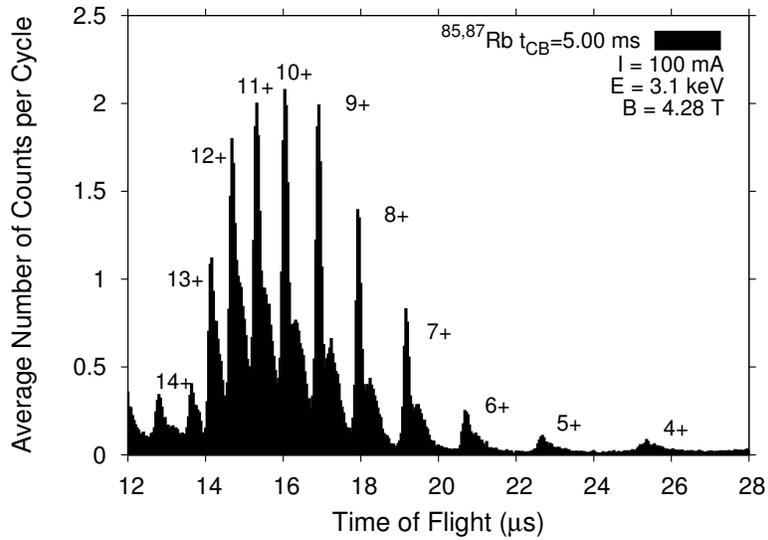
Figure 5.1: Time-of-flight spectrum of charge-bred Rb for $E = 3.1$ keV, $I = 100$ mA, $B = 4.28$ T, and $t_{CB} = 5$ ms. Higher charge states appear at a longer time of flight. The charge states of Rb 4+ to 14+ are labeled.
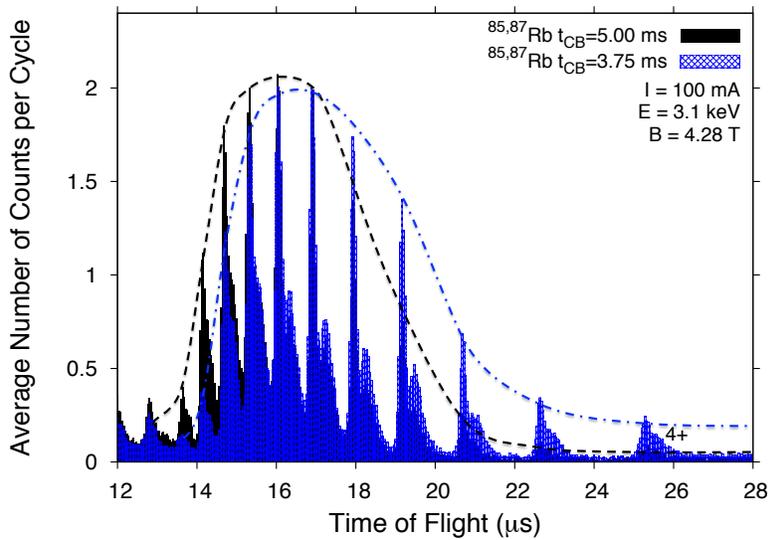
Figure 5.2: Time-of-flight spectra of charge-bred ^{85,87}Rb for $E = 3.1$ keV, $I = 100$ mA, $B = 4.28$ T, and $t_{CB} = 3.75$ ms (shaded blue) and 5 ms (solid black). An envelope passes through the peak number of counts in each charge state to show qualitative differences between the two distributions (details in text). No corrections have been made for background or residual gas ions.

59

After 3.75 ms of charge breeding, lower charge states have become more populated, higher charge states have become less populated, and the general trend in the time-of-flight spectrum is to populate longer times. Superimposing the time-of-flight spectra, as in Figure 5.2, is a useful way to compare qualitative features between charge-state distributions; however, for subtle changes or for comparing many charge-state distributions, a quantitative indicator that summarizes the key features of a charge-state distribution is beneficial to the analysis.

5.2.2 Analysis Method of the Time-of-Flight Spectra

Each experimental charge-state distribution will be analyzed by examining its time of flight T spectrum and by identifying the time of flight $\overline{T}$ of *the average charge state* $\overline{Q}$. Additional information will be obtained by calculating the *range of charge states in the distribution* σ_Q, which leads to asymmetric widths in time of flight $\sigma_T^{\pm}$. This asymmetry is caused by a decreasing separation in time of flight between consecutive charge states as the charge state increases. The time of flight of the average charge state $\overline{T}$ and the width of the charge-state distribution in time of flight $\sigma_T^{\pm}$ was found to provide a complete description of a distribution for comparing various experimental settings in this thesis.

The time of flight of the average charge state is found by first mapping the time-of-flight axis to a continuous spectrum of charges $Q = \kappa/T^2$, where κ is an arbitrary constant. In order for Q to correspond to the charge states marked in Figure 5.1, the constant must be defined as $\kappa = \sqrt{md^2/2U}$ as per Equation 3.1. However, since the procedure is to determine Q and then transform back to time of flight, the transformation does not depend on the value of κ and it can be set to $\kappa = 1$ for simplicity. Then

$$Q_{bin} = \frac{1}{T_{bin}^2} \quad , \tag{5.2}$$

where T_{bin} is the time of flight for a single bin in a time of flight spectrum and Q_{bin} is its corresponding charge. The average charge state $\overline{Q}$ and spread σ_Q is then:

$$\overline{Q} = \frac{\sum N_{bin} Q_{bin}}{\sum N_{bin}} \tag{5.3}$$

and,

$$\sigma_Q = \sqrt{\frac{\sum \left(Q_{bin} - \overline{Q}\right)^2 N_{bin}}{\sum N_{bin}}} \quad . \tag{5.4}$$

Here, N_{bin} is the number of counts in a single bin of the time-of-flight histogram, and Q_{bin} is the charge corresponding to the respective bin. The uncertainty in $\overline{Q}$ is given by:

$$\delta Q = \frac{\sigma_Q}{\sum N_{bin}} \tag{5.5}$$

Finally, converting back to T gives the time of flight of the average charge state $\overline{T}$, its uncertainty δT, and the asymmetric widths σ_T^+ and σ_T^- :

$$\overline{T} = \frac{1}{\sqrt{\overline{Q}}} \quad , \quad \text{and} \quad \delta T = \frac{\delta Q}{2\sqrt{\overline{Q}^3}} \quad , \tag{5.6}$$

$$\sigma_T^+ = \frac{1}{\sqrt{\overline{Q} - \sigma_Q}} \quad , \quad \text{and} \quad \sigma_T^- = \frac{1}{\sqrt{\overline{Q} + \sigma_Q}} \quad . \tag{5.7}$$

Graphically, when $\overline{T}$ is plotted on the time-of-flight spectrum, it overlaps with the average charge state of the distribution. Since δT scales with $1/\sqrt{N}$, the size of the uncertainty in $\overline{T}$ represents the number of counts in the distribution. The width of the distribution is shown by $\sigma_T^\pm$. This value represents how spread out the distribution is in time of flight and how many charge states are in the distribution. Thus all charge-state distributions can be summarized by the quantity:

$$\text{time-of-flight spectrum} \implies \overline{T}(\delta T)_{\sigma_Q^-}^{\sigma_T^+} \quad . \tag{5.8}$$

The charge-state distributions taken for $t_{CB} = 3.75$ ms and 5 ms are shown in Figure 5.3, with $\overline{T}(\delta T)_{\sigma_Q^-}^{\sigma_T^+}$ at the top of the graph. As expected, for $t_{CB} = 5$ ms the distribution is narrower and $\overline{T}$ is smaller than for the distribution resulting from $t_{CB} = 3.75$ ms. Furthermore, the total number of counts in each distribution has reduced the uncertainty on $\overline{T}$ so that the two different charge-state distributions are clearly distinguished by comparing the time of flight of the average charge state for the two spectra. In order to compare the effect of different charge-breeding conditions on the resulting charge-state distributions the quantity $\overline{T}(\delta T)$ is used rather
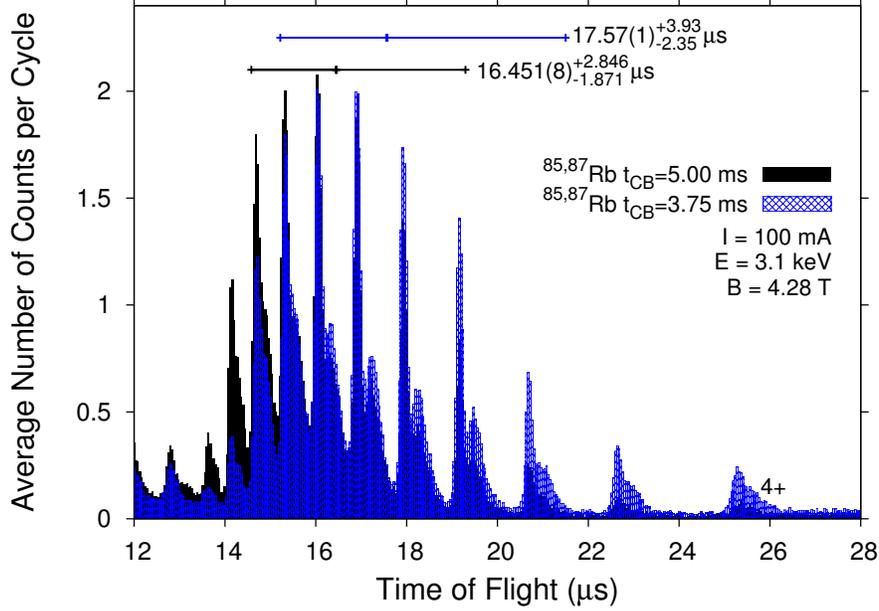
Figure 5.3: Time-of-flight spectra of charge-bred ^{85,87}Rb for $E = 3.1$ keV, $I = 100$ mA, $B = 4.28$ T, and $t_{CB} = 3.75$ ms (shaded blue) and 5 ms (solid black). The time of flight of the average charge state and the asymmetric widths are shown at the top of the graph in the format $\overline{T}(\delta T)\,{}^{\sigma^+}_{\sigma_-}$.

than providing the entire time-of-flight spectrum.

5.3 Results and Discussion

5.3.1 Effect of Varying the Electron-Beam Current

Data were collected for various combinations of electron-beam current and charge-breeding time at a fixed magnetic field strength of $B = 4.28$ T. The different combinations of I and t_{CB} are provided in Table 5.1. For each setting, the resulting charge-state distribution was analyzed using the time-of-flight method described in the previous section. A comparison of all the combinations was made by plotting $\overline{T}(\delta T)$ against the product of I and t_{CB}, as seen in Figure 5.4. Lines connect points taken at the same electron-beam current and labels indicate the charge-breeding

times. This is done to assist in identifying trends and interpreting the results.

Table 5.1: Charge-breeding settings for the production of various charge-state distributions by varying the electron-beam current and the charge-breeding time. Three different values of $I \cdot t_{CB}$ were considered. All experiments were performed with $B = 4.28$ T.

Electron	Charge-breeding time for $I \cdot t_{CB}$		
beam current	375 mA ms	500 mA ms	750 mA ms
100 mA	3.75 ms	5 ms	7.5 ms
75 mA	5 ms	6.67 ms	10 ms
50 mA	7.5 ms	10 ms	15 ms

There are three trends in the time of flight of the average charge state $\overline{T}$ that can be identified from Figure 5.4: changes for constant I; changes for constant t_{CB}; and changes for constant $I \cdot t_{CB}$. For each electron-beam current, $\overline{T}$ gradually decreases with an increase in the charge-breeding time; this is the same result that was seen in the comparison of the charge-state distributions in Figure 5.3: higher charge states are produced after a longer charge-breeding time. A similar trend is noticed for data taken at constant t_{CB}: increasing the electron-beam current density results in a lower $\overline{T}$. This trend supports the statement that increasing the electron-beam current increases the rate of charge-changing interactions and produces higher charge states in otherwise identical conditions.

Increasing either the charge-breeding time or the electron-beam current density results in the production of higher charge states; however if the rate of charge evolution scales with the product $I \cdot t_{CB}$, then $\overline{T}$ should respond in the same way to changes in I as changes in t_{CB}. Three different values of $I \cdot t_{CB}$ are shown in Figure 5.4 and for any one, $\overline{T}$ varies greatly for different combinations of I and t_{CB} despite their constant product. Thus, increasing the electron-beam current will result in higher charge states, as expected; however, charge-state distributions that were produced with a constant product of I and t_{CB} are not unique.

To explore the effect of changing the electron-beam current further, consider the point taken for $I = 50$ mA and $t_{CB} = 7.5$ ms. Doubling the charge-breeding time to $t_{CB} = 15$ ms leads to a shift in $\overline{T}$ of 2.5 μs, confirming that higher charge states
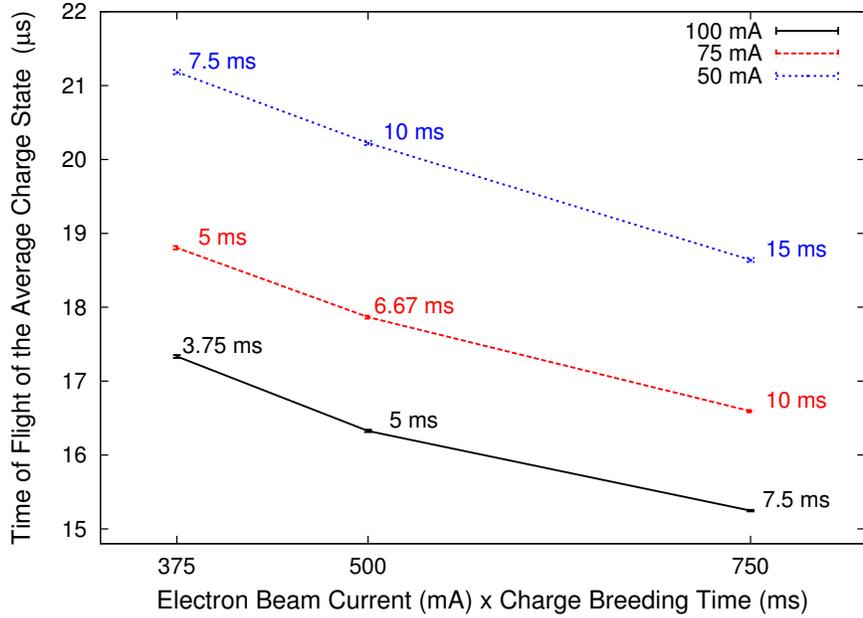
Figure 5.4: Results of changing the electron-beam current and charge-breeding time on the production of charge-state distributions. The $\overline{T}(\delta T)$ from each charge-state distribution is plotted agains the product of I and t_{CB} for the different charge-breeding settings. Lines represent constant electron-beam current (100 mA in solid black, 75 mA in dashed red, 50 mA in dotted blue) and labels indicate the t_{CB}.

are reached. However, if instead the electron-beam current is doubled, the shift in $\overline{T}$ is 5.9 μ. This implies that doubling the electron-beam current results in a shift to higher charge states than when the charge-breeding time was doubled. Similar trends can be identified for other combinations of I and t_{CB}, showing experimentally that increasing the electron-beam current is more favourable than increasing the charge-breeding time for producing higher charge states. Returning to Properties I and II, it was originally suspected that the charge-state evolution would scale with J-time $\propto f_{e;q} I B t_{CB}$. Since the magnetic field was not changed, the deviation from this expectation can be interpreted in the context of the electron-ion-overlap factor, which was assumed to be $f_{e;q} = 1$ (Assumption I). If instead, $f_{e;q}$ was less than one and increased with the electron-beam current, then a change in I could

have changed J-time by more than the equivalent change in t_{CB}.

The electron-beam current could change the overlap between the electrons and trapped ions in two ways: the increased number of negative charges in the trapping regions could have attracted the positive ions outside of the electron beam causing them to spend more time in the electron beam; and the electron-beam radius could have increased with the electron-beam current. A better model of the charge-breeding conditions tested here can be made by comparing charge-state distributions that have the same value of $\overline{T}$. For example, assuming instead that J-time $\propto I^x \cdot t_{CB}$, the points sharing the same $\overline{T}$ can be used to determine the exponent x on the electron-beam current. Here, $I = 75$ mA, $t_{CB} = 5$ ms and $I = 50$ mA, $t_{CB} = 15$ ms produce the most similar charge-state distributions, resulting in

$$x = -\frac{\ln(t_2/t_1)}{\ln(I_2/I_1)} \approx 2.7$$

at the time of these studies. Hence, for a more general model, the assumption $f_{e;q} = 1$ is not valid and moreover, $f_{e;q}$ appears to change with the electron-beam current.

5.3.2 Effect of Varying the Magnetic Field Strength

Data were collected for various combinations of magnetic field strength and charge-breeding time at an electron-beam current of $I = 50$ mA. The different combinations of B and t_{CB} are provided in Table 5.1. For each setting a charge-state distribution was analyzed using the time-of-flight method described in Section 5.2.2. A comparison of all of the combinations was made by plotting $\overline{T}(\delta T)$ against B, as seen in Figure 5.5. Lines connect points taken at the same charge-breeding time and labels indicate the values of $B\, t_{CB}$ in tesla-milliseconds. This is done to assist in identifying trends and interpreting the results.

There are three trends in the time of flight of the average charge state $\overline{T}$ that can be identified from Figure 5.5: changes for constant B; changes for constant t_{CB}; and changes for constant $B \cdot t_{CB}$. For the former, the same trend that was observed in Section 5.3.1 was confirmed: a longer charge-breeding time results in a lower $\overline{T}$ due to a shift to higher charge states over the course of the charge breeding. As for constant values of $B \cdot t_{CB}$, only 64.2 T ms is duplicated, and the two settings

Table 5.2: Charge-breeding settings for the production of various charge-state distributions by varying the magnetic field strength in the trapping region and the charge-breeding time. All data were taken for $I = 50$ mA.

Magnetic field	Charge-breeding time		Respective $B \cdot t_{CB}$	
4.28 T	15 ms	30 ms	64.2 T ms	128.4 T ms
3.03 T	15 ms	30 ms	45.5 T ms	90.9 T ms
2.14 T	15 ms	30 ms	32.1 T ms	64.2 T ms
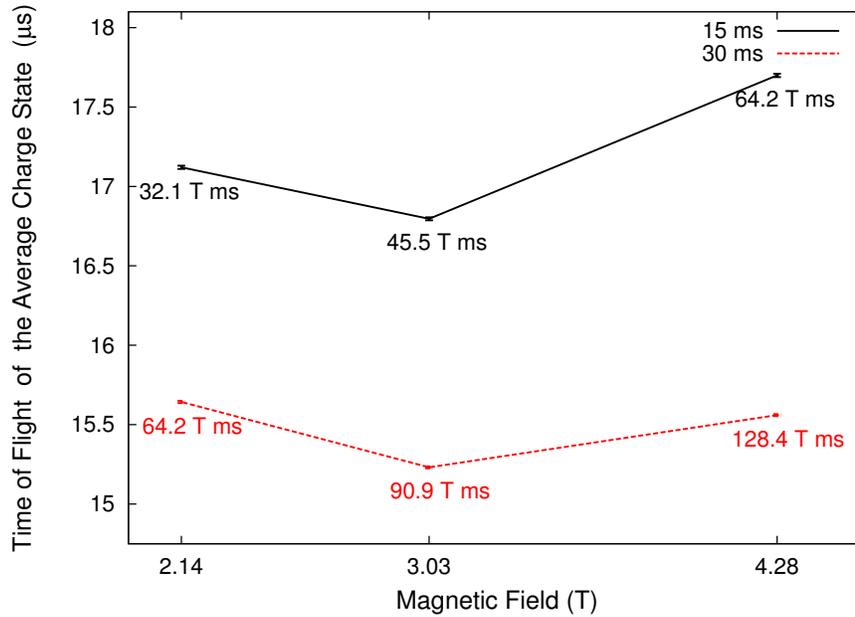
Figure 5.5: Results of changing the magnetic field strength in the trapping region and charge-breeding time on the production of charge-state distributions. The $\overline{T}(\delta T)$ from each charge-state distribution is plotted against the value of B for different charge-breeding settings. Lines connect constant charge-breeding time (15 ms in solid black, 30 ms in dashed red) and labels indicate the product of B and t_{CB}.

produce charge-state distributions that have values of $\overline{T}$ that are different by more than 2 μs. Finally, for a constant charge-breeding time, increasing the magnetic field can cause either a decrease or an increase in $\overline{T}$, which occurs for the transition from 2.14 T to 3.03 T and from 3.03 T to 4.28 T respectively. Since a lower $\overline{T}$ represents higher charge states and more effective charge breeding, this suggests that charge breeding was most effective at 3.03 T. This is despite the fact that the electron beam should be more compressed and thus have a higher current density with the stronger magnetic field at 4.28 T. Thus, increasing the magnetic field in the trapping region does not have a consistent effect on the resulting charge-state distribution. Furthermore, charge-state distributions that were produced under a constant product of B and t_{CB} are not unique.

Since the expected trends are not clearly present in the experimental data, a more complete description of the experimental conditions is needed. A possible explanation for the observed trends could again stem from the idealistic assumption that $f_{e;q} = 1$. The magnetic field in the trapping region is responsible for the compression of the electron beam, as discussed in Section 2.3.2; however, in this section it was also mentioned that the smallest possible electron beam is not necessarily optimal if it lowers the electron-ion-overlap factor. Since the observed charge-state distributions combine the effects of charge breeding with ion injection into and extraction out of the EBIT, the interpretation of these results is more complicated. In the context of Figure 5.5, a possible interpretation is that the charge-breeding conditions were optimal for 3.03 T and that decreasing the magnetic field from 3.03 T results in a loss of electron-beam current density that outweighs a gain in $f_{e;q}$. When increasing the magnetic field from 3.03 T the loss in $f_{e;q}$ possibly outweighs the gain in electron-beam current density. Thus, in order to determine the effect of electron beam compression on the rate of charge evolution, experimental conditions where $f_{e;q} \approx 1$ are needed.

5.3.3 Realignment of the Injection Beam Line and EBIT Components

One of the outcomes of the experimental investigations was the need to determine the potential cause of poor overlap between the electron beam and the trapped ions. Alignment studies were performed as misalignment between the beam line and the

67
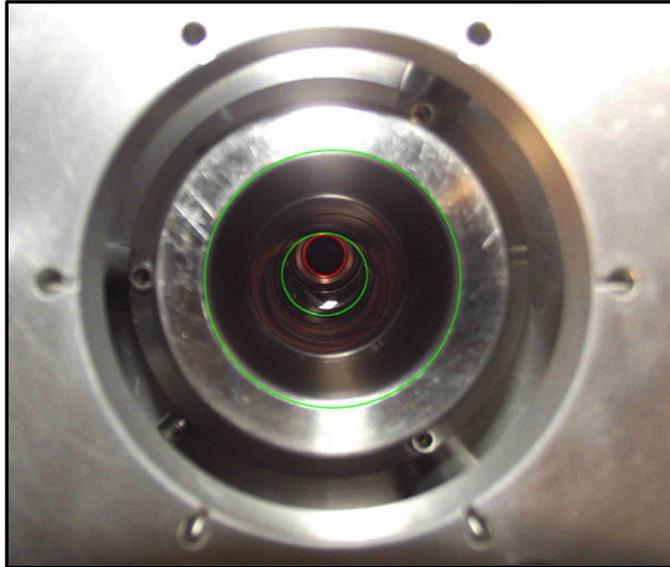
Figure 5.6: Photograph of the collector misalignment looking down the axis of the beam line. The front and back ends of the ion injection optics (green) and the front of the collector assembly (red) are visible. The collector assembly is 7 mm off of the beam line axis.

magnetic field axis could cause asymmetric ion injection conditions, leading to a poor electron-ion-overlap factor. The alignment procedure at TITAN has all components of the beam line aligned to within a millimetre or less. Despite this, it was discovered that there was a misalignment between the electron collector and the beam axis by 7 mm, as shown in Figure 5.6. The electron gun assembly, which was aligned with respect to the cathode assembly, was also misaligned with respect to the magnetic field axis by the same amount as a result. This misalignment could have had two effects on the charge-breeding investigations: one in regards to the ion injection and one in regards to the electron-beam properties. These are discussed below.

In an ideal set-up, the magnetic field axis shares the same axis as the beam line. Careful alignment of the TITAN EBIT magnet chamber was performed to achieve this during its initial commissioning. In this case, ion injection can occur on-axis so that the incoming ion bunch only sees an axial magnetic field gradient. This
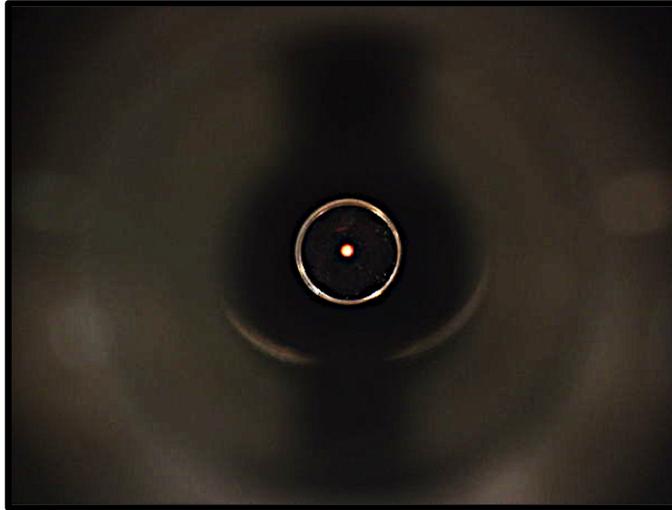
Figure 5.7: Photograph of the realigned collector looking down the axis of the beam line. The cathode is warm and glowing in the centre of the photograph. The collector assembly, illuminated by the cathode, and is on-axis with both the electron gun and the beam line.

on-axis injection minimizes the initial radius of the trapped ions, improving the electron-ion overlap factor, and maximizing the injection efficiency [82]. A collector assembly misalignment of 7 mm has two effects on incoming ions: since the collector is no longer aligned with the beam line, part of the opening is blocked (Figure 5.6), and the injection efficiency decreases; and additional steering is required to bring the ions off-axis and through the collector opening, giving them poor initial conditions and decreasing the electron-ion overlap factor.

As for the electron-beam properties, the theory that describes the electron-beam radius from Section 2.3.2 only applies to an electron beam moving along the magnetic field axis. An electron beam originating off axis suffers from less compression [82], decreasing the current density of the electron beam, and responds less predictably to changes in the magnetic field. As a consequence, the assumption $J \propto B$ is not valid with the misalignment present in the system. In order to restore the system to the desired operating conditions, the electron collector and gun assemblies were realigned with the beam line, as seen in Figure 5.7. With the electron

69

gun, magnetic field, collector assembly, and beam line all sharing the same axis, the electron-ion-overlap factor should be significantly improved and the experimental conditions should be better described by the outlined theory. Experimental investigations are underway to determine the full impact of this realignment on charge breeding; these are, however, outside the scope of this thesis.

5.3.4 Comparison to CBSIM

The systematic studies of charge breeding under controlled conditions have been provided in Sections 5.3.1 through 5.3.3. The experimental findings have demonstrated the importance of the electron-ion-overlap in realizing experimental conditions that agree with theoretical expectations. Since the theory used in developing CBSIM is not compatible with the experimental findings from this work, it is not possible to determine the electron-beam current density based on theoretical calculations for use in the optimization of G_{HCI}. Despite this, however, a direct comparison between an experimental charge-state distribution and the charge-state evolution in CBSIM can be made to determine the electron-beam current density J_{CBSIM} that is in agreement with CBSIM for the specific charge-breeding settings.

To illustrate an example of how this can be done, Figure 4.3 (zoomed in on the x-axis) and Figure 5.1 have been provided here for comparison in Figures 5.8 and 5.9. From the experimental charge-state distribution, after 5 ms of charge breeding, the maximum charge state is 10+ with small amounts in 5+ and 15+ on either end of the time-of-flight distribution. In the spectrum from CBSIM, the 10+ charge state peaks for a J-time of approximately 0.35 A cm^{-2} s, suggesting that the effective electron-beam current density in the trapping regions is approximately $J_{CBSIM} = \frac{\text{J-time}}{t_{CB}} \approx 70$ A cm^{-2}. Since the fraction of ions in 5+ and 15+ in CBSIM is almost zero when the fraction in 10+ reaches a maximum, a more conservative estimate would be to consider when small but non-negligible amounts of 5+ and 15+ are present in the charge-state distribution from CBSIM. Qualitatively, this might correspond to a J-time of 0.2 to 0.6 A cm^{-2} s, an electron-beam current density of $J_{CBSIM} = 40$ to 120 A cm^{-2}, and an electron-beam radius of $r_H = 146$ to 252 μm (Equation 2.9).
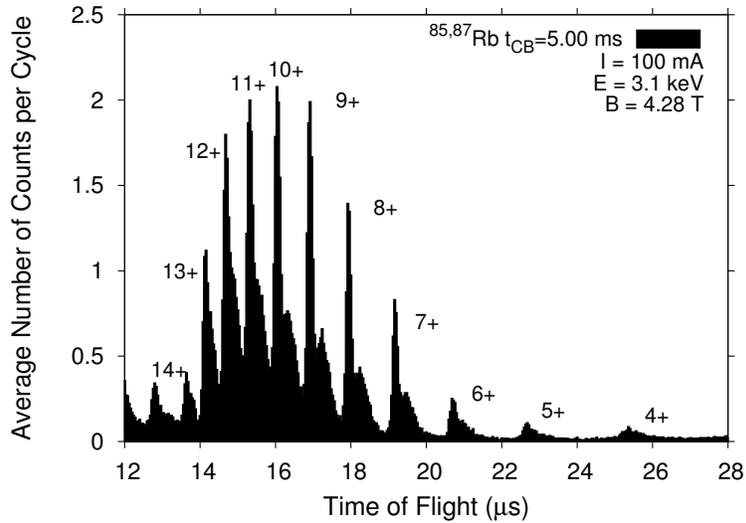
Figure 5.8: Time-of-flight spectrum of charge-bred ^{85,87}Rb for $E = 3.1$ keV, $I = 100$ mA, $B = 4.28$ T, and $t_{CB} = 5$ ms for comparison to CBSIM. The charge-state distribution peaks at $q = 10+$ with a small but non-negligible amounts in the 5+ and 15+ charge states.
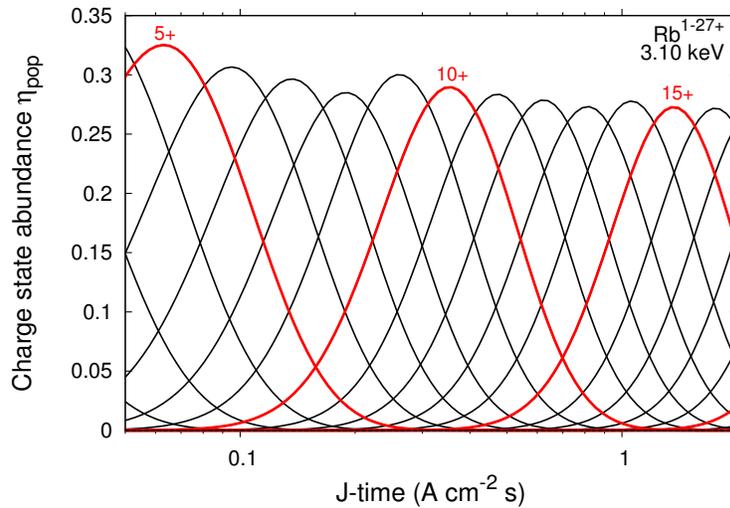
Figure 5.9: Charge-state evolution of ^{85}Rb^{q+} for threshold charge-breeding conditions at $E = 3.1$ keV for comparison to an experimental charge-state distribution. The 10+ charge state peaks for a J-time ≈ 0.35 A cm^{-2} s and there is a near-negligible fraction of ions in the 5+ and 15+ charge states (red) at this value of J-time.

5.4 Recommendation for Future Charge-Breeding Studies

Based on the results of these first systematic experimental studies, a series of future investigations and improvements can be recommended. With the discovery of the electron collector misalignment, it was found that the theoretical descriptions did not accurately represent the experimental conditions. The subsequent repositioning of the electron collector and gun assemblies (Section 5.3.3), will change the ion injection conditions as well as the properties of the electron beam. As such, the extent of the improvement to the charge breeding and compatibility with theory with the realigned system should be investigated. Additional studies could be performed for an enhanced understanding of the charge-breeding conditions. These include:

1. Investigating the role of the bucking coils: in Section 2.3.2 the effect of the residual magnetic field at the cathode on the electron-beam radius was discussed. With possible changes to the electron beam of more than a factor of five (Figure 2.10), significant changes to the electron-beam current density could be made by changing the residual magnetic field at the cathode.

   The effect of changing the residual magnetic field at the cathode on the charge-state evolution could be studied by changing current in the bucking coils. Experimentally this would be similar to changing the magnetic field in the trapping region; however, the opposite effect is expected since an increase in the residual field at the cathode expands the electron beam, effectively slowing down the charge-breeding process. This effect could be studied and quantified.

2. Investigating the role of the electron-beam energy: in Section 2.3.2 the effect of the electron-beam energy on the charge-state abundances was discussed. Since the electron-beam energy determines the magnitude of the cross sections for both electron impact ionization and radiative recombination, changes to the electron-beam energy should change the abundance of ions in a given charge state. This was demonstrated with CBSIM for a closed electronic shell (Section 4.1.3).

72

Experimentally this can be studied by varying the electron-beam energy within the gap of ionization potentials and observing the width of the charge-state distribution ($\sigma_T^{\pm}$). If the width of the distribution begins to shrink without significantly affecting the centre $\overline{T}$, this would indicate that the ions have begun to occupy fewer charge states and are fully populating the threshold charge state.

The results of these improvements and investigations will provide additional information on the operation of the EBIT and provide enhanced performance and predictability of the system.

5.5   Summary

A series of experimental studies were designed to test the applicability of the theory discussed in Section 2.3.2 as well as the assumptions made when simulating the charge breeding of an ion bunch in an electron beam. The properties of the electron-beam current density were the primary focus of the studies due to its potential to improve the precision gained in a PTMS measurement with highly charged, radioactive ions (Section 4.4). It was found that a charge-state distribution theoretically evolves with the product of the electron-beam current density and the charge breeding time, and that current density theoretically follows $J \propto B \cdot I$. Therefore, the primary relationship that was investigated was whether or not I, B, and t_{CB} provided equal contribution to the evolution of charge states.

The studies were carried out independently for the electron-beam current and the magnetic field strength in the trapping region. For the first study, a set of charge-state distributions was produced under various combinations of I and t_{CB}. By analyzing the time of flight of the average charge state, it was found that changing the electron-beam current changed the charge-state distribution in a predictable way. Despite this, the charge-breeding time and electron-beam current were not found to contribute equally to the charge-state evolution as charge-state distributions produced for a constant product of I and t_{CB} were not unique. In the study of the magnetic field in the trapping region, changes in B did not have a predictable effect on the charge-state distributions since an increase in B could either cause a shift to lower or higher charge states for the same charge-breeding time. These

results indicated that the idealistic assumption $f_{e;q} = 1$ is not valid in our studies. It also demonstrated that $f_{e;q}$ also changes with the electron-beam current and magnetic field strength in the trapping region.

A possible explanation for the observed trends was provided: a misaligned electron gun and collector assembly. The electron collector and gun assemblies were found to be 7 mm off from the axis shared by the beam line and the magnetic field. This misalignment could have been responsible for experimental results that did not agree with the the theoretical expectations. Additional studies with the electron gun assembly, magnetic field axis, collector assembly, and beam line all on-axis with one another are recommended to determine the effect of these enhanced charge-breeding conditions. Furthermore, additional tests including varying the residual magnetic field at the cathode and testing the effect of the electron-beam energy on the production of charge-state distributions were recommended.

Chapter 6

Precision Q-value Measurement of the $^{51}\mathrm{Cr}(e^-, \nu_e)^{51}\mathrm{V}$ Reaction

The technical work outlined in this thesis was complemented by a precision measurement [26] of the $^{51}\mathrm{Cr}$ electron-capture Q-value. Both $^{51}\mathrm{Cr}$ and its daughter nucleus $^{51}\mathrm{V}$ were produced at ISAC in August 2012. The simultaneous production of the two isotopes allowed a direct Q-value measurement to be made. The MPET had been prepared for measurements on ions with a mass-to-charge ratio $m/q \sim 10$ as this regime of m/q has been extensively studied at TITAN [63]. To accommodate this setup, the EBIT was optimized to maximize the abundance in the 5+ and 6+ charge states rather than striving for high charge states. The results of this experiment are provided in this chapter.

6.1 Motivation for the Direct Q-value Determination

Precision experiments at radioactive beam facilities [3] have made a significant impact on the field of neutrino physics. With the goal of identifying yet undetermined properties of the neutrino, high-precision measurements of branching ratios, half-lives, and Q-values have guided the construction of next generation experiments and refined theoretical models, advancing the field. Penning-trap mass spectrometry is at the precision frontier for performing direct Q-value measurements [3, 9], providing accurate results that have included shifts from reaction-based measure-

ments of more than five standard deviations (5σ) [83–86]. These measurements have contributed to the search for neutrinoless double-beta decay [87], resonant-enhanced double-electron capture [88], and the determination of the absolute mass scale of the electron neutrino [86, 89]. Such experiments, described in detail in Ref. [90], have affirmed the value of Penning-trap measurements in the broad context of neutrino physics research.

A persistent discrepancy in the field of neutrino physics is the so-called gallium anomaly, which resulted from the calibration measurements that were performed at the solar neutrino experiments SAGE and GALLEX. Both SAGE and GALLEX used the ^{71}Ga(ν_e,e$^-$)^{71}Ge neutrino-capture reaction to detect solar neutrinos. This reaction offered the advantage of being sensitive to the more abundant, lower energy, solar neutrinos produced from the p-p chain [91]. The range of sensitivity for different solar neutrino detectors is shown with the calculated energy spectrum of solar neutrinos in Figure 6.1. The results from the experiments with Ga confirmed the solar-neutrino deficiency [92] that was observed with earlier chlorine detectors [93]. Calibration measurements were performed using terrestrial neutrinos from ^{51}Cr electron-capture at GALLEX and both ^{51}Cr and ^{37}Ar electron-capture at SAGE, which "demonstrated the absence of any significant unexpected systematic errors" [94] in the solar neutrino measurements. Despite this, the observed event rate [95] with these terrestrial sources revealed a 13(5)% deficit when compared to the rate predicted by theory [92]. The results of the four calibration measurements performed at SAGE and GALLEX are summarized in Figure 6.2. This discrepancy between observed and predicted event rate has become known as the gallium anomaly [27].

Missing knowledge of the underlying nuclear structure involved in the calibration reactions is thought to be a possible cause of the discrepancy. Other possible explanations include a statistical fluctuation with 5% probability, miscalculated efficiencies, or physics of unknown origin [95]. A recent white paper [27] explores the gallium anomaly in the context of sterile neutrinos and notes that it could be accounted for by a massive sterile neutrino. Precision measurements have been made on the nuclear structure of the detector materials, confirming the ^{71}Ga(ν_e,e$^-$)^{71}Ge Q-value of 233.5(1.2) keV [67] and re-evaluating the contribution of the ^{71}Ge excited states to the neutrino capture cross-section for a total of $7.2 \pm 2.0\%$ [96].
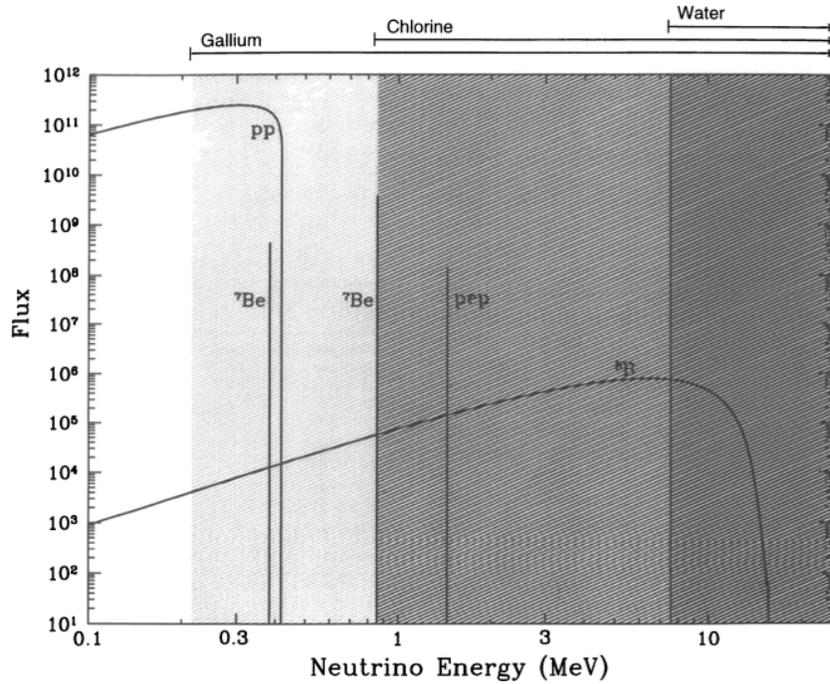
Figure 6.1: Energy spectrum of solar neutrinos and energy thresholds for neutrino detectors. The energy spectrum of the neutrinos from the p-p chain as predicted by the Standard Model is shown. The arrows at the top indicate the energy sensitivity of different neutrino detectors (figure from [91] ©AAS. Reproduced with permission).
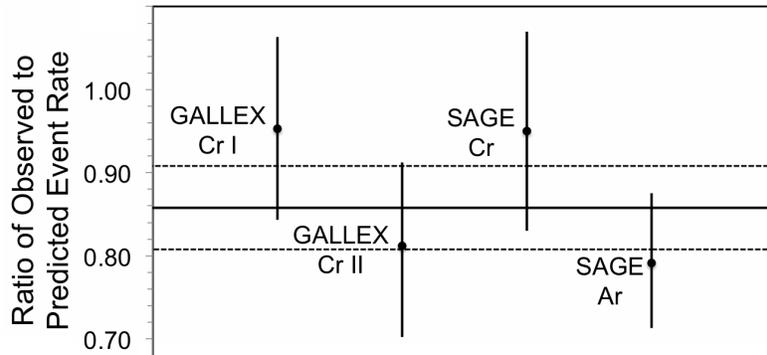

Figure 6.2: Ratio of observed to predicted event rate for the neutrino source experiments at SAGE and GALLEX. The results of the two ^{51}Cr experiments at GALLEX and both the ^{51}Cr and ^{37}Ar experiments from SAGE are shown. The the weighted average (solid) and the its uncertainty (dashed) of the four results (data from Ref. [27]).

These results have eliminated any uncertainty in the nuclear structure of the detector material at the level required to resolve the gallium anomaly. However, uncertainty in the neutrino source material remains. The ^{51}Cr$(e^-,\nu_e)^{51}$V Q-value of 752.63(24) keV, as reported in the Atomic Mass Evaluation 2012 (AME12) [97], is dominated by the result of a single reaction-based measurement [98]. Accurate knowledge of this value is of great importance as it determines the probability that a neutrino will be captured into an excited state in ^{71}Ge. If the value in the AME12 is artificially inflated by 14 keV or more due to an erroneous measurement, then the predicted event rate would have falsely included neutrino capture into the 499.9 keV excited state and been overestimated by $4.5 \pm 0.4\%$ [96]. This potential correction to the gallium anomaly has motivated an independent check of the ^{51}Cr$(e^-,\nu_e)^{51}$V Q-value using the TITAN facility [4].

6.2   Experiment Details

A review of the TITAN experimental setup can be found in Chapter 3. All three ion traps, the RFQ, the EBIT, and the MPET, were used for the ^{51}Cr electron-capture Q-value measurement. The ^{51}Cr and ^{51}V nuclides were produced by impinging a 480 MeV, 10 μA proton beam from the TRIUMF main cyclotron on a UO$_2$ target at ISAC. The beam was ionized by a FEBIAD ion source [61] and extracted from the target station as a 20 keV continuous ion beam.

The ion bunches out of the TITAN RFQ were sent to the EBIT for charge breeding by an electron beam with current $I_e = 89$ mA, and energy $E_e = 2.55$ keV. The magnetic field strength was 4.5 T and charge-breeding times of 2 and 3 ms were used to optimize the number of ions in charge states 5+ and 6+, respectively. The desired charge state was selected by the BNG for injection into the MPET. Additionally, ^{39}K$^+$ ions were delivered from the TITAN off-line ion source intermittently between ^{51}Cr and ^{51}V measurements and measured in the 4+ charge state to obtain a similar m/q-ratio. Resonances were taken with excitation times of $T_{RF} = 60, 66, 160$, and 166 ms, and an example of a ^{51}Cr^{5+} resonance with $T_{RF} = 160$ ms is shown in Figure 6.3. Due to the simultaneous delivery of ^{51}Cr and ^{51}V, dipole cleaning [99] was required to remove the undesired species from the trap before implementing the TOF-ICR excitation. Dipole excitations were ap-
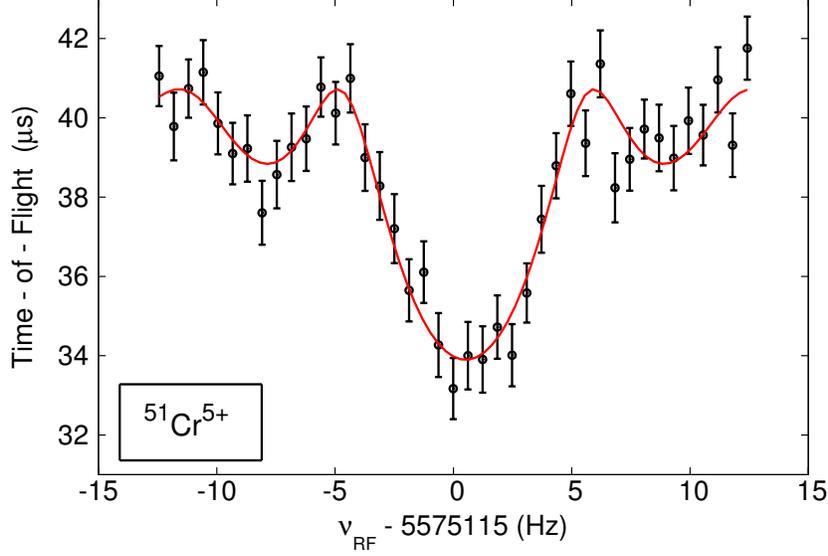
Figure 6.3: A TOF-ICR resonance for $^{51}\text{Cr}^{5+}$ with a $T_{RF} = 160$ ms excitation. The solid line is a fit of the theoretical line shape [42] to the data.

plied for 36 ms on ions in charge state 5+ and 30 ms on ions in charge state 6+.

6.3   Analysis and Results

Frequency measurements on the isotopes of interest, $^{51}\text{Cr}^{5,6+}$, $^{51}\text{V}^{5,6+}$, and $^{39}\text{K}^{4+}$, were performed in alternation. Different reference ion species were chosen for the direct Q-value measurement (^{51}V), and for the mass measurements (^{39}K). The known mass and measured frequency of the reference ion were used in the calculation of either the Q-value or the mass M. The frequency measurements of the reference ion were linearly interpolated to account for first order drifts in the magnetic field [63]. The ratio of this interpolated frequency $\widetilde{\nu}_c$ and the frequency of the ion of interest ν_c is then independent of the MPET magnetic field, and it is the primary result of this experiment. For the direct Q-value measurement:

$$R_Q = \frac{\widetilde{\nu}_c\left(^{51}\text{V}^{q_V+}\right)}{\nu_c\left(^{51}\text{Cr}^{q_{Cr}+}\right)} = \frac{m\left(^{51}\text{Cr}^{q_{Cr}+}\right)}{m\left(^{51}\text{V}^{q_V+}\right)} \frac{q_V}{q_{Cr}} \quad , \tag{6.1}$$

and for the mass measurement:

$$R_M = \frac{\widetilde{\nu}_c(^{39}\mathrm{K}^{q_\mathrm{K}+})}{\nu_c(\mathrm{X})} = \frac{m(\mathrm{X})}{m(^{39}\mathrm{K}^{q_\mathrm{K}+})} \frac{q_\mathrm{K}}{q_\mathrm{X}} \quad , \tag{6.2}$$

where X represents either $^{51}\mathrm{Cr}^{q+}$ or $^{51}\mathrm{V}^{q+}$.

The Q-value and the mass M are calculated directly from the weighted average of all measured ratios $\overline{R}_Q$ or $\overline{R}_M$, respectively:

$$\begin{aligned}
Q =& \left(\overline{R}_Q \tfrac{q_\mathrm{Cr}}{q_\mathrm{V}} - 1\right) M_\mathrm{V} - \left(\overline{R}_Q - 1\right) q_\mathrm{Cr}\, m_e \\
&+ \overline{R}_Q \tfrac{q_\mathrm{Cr}}{q_\mathrm{V}}\, B_e\!\left(^{51}\mathrm{V}^{q_\mathrm{V}+}\right) - B_e\!\left(^{51}\mathrm{Cr}^{q_\mathrm{Cr}+}\right)
\end{aligned} \tag{6.3}$$

$$M_\mathrm{X} = \overline{R}_M \tfrac{q_\mathrm{X}}{q_\mathrm{K}} \left(M_\mathrm{K} - q_\mathrm{K}\, m_e + B_e\!\left(^{39}\mathrm{K}^{q_\mathrm{K}+}\right)\right) + q_\mathrm{X}\, m_e - B_e\!\left(^{51}\mathrm{X}^{q_\mathrm{X}+}\right) \tag{6.4}$$

where M is the atomic mass, m_e is the electron mass, and B_e is the sum of atomic binding energies for all electrons missing from the highly charged ion. The reference masses of $^{51}\mathrm{V}$ and $^{39}\mathrm{K}$ were obtained from the AME12 [100], and the binding energies were taken from Ref. [77], with estimated uncertainties in the 10 eV range. The uncertainty of the Q-value and masses were obtained from propagation of errors, with the primary contribution coming from uncertainty of the measured ratio δR. Since the ratio contains the ionic masses, the analysis was carried out on 5+ and 6+ charge states independently.

In the direct Q-value measurement, the achieved statistical precision for the final ratio was $\delta R_{stat}^{5+} = 12.7$ ppb and $\delta R_{stat}^{6+} = 21.5$ ppb, which was added in quadrature to any uncertainty resulting from systematic effects (discussed below). Many of the m/q-dependent systematic uncertainties common to Penning-trap mass spectrometry, including spatial magnetic field inhomogeneities, harmonic distortions of the electrode structure, misalignment between magnetic field and trap axes, and relativistic effects, became negligible [63] by measuring the ratio in an m/q-doublet (i.e., $^{51}\mathrm{Cr}^{5+}$ with $^{51}\mathrm{V}^{5+}$, and $^{51}\mathrm{Cr}^{6+}$ with $^{51}\mathrm{V}^{6+}$). Along with fluctuations in the trapping potential, these are all sub part-per-billion (ppb) effects, which is significantly smaller than δR_{stat}. Magnetic field drifts, which have been measured at

Table 6.1: Results for the Q-value determination of the ^{51}Cr(e$^-$,ν_e)^{51}V reaction. Both the measured frequency ratio and the resulting Q-value are reported with their total uncertainties.

Ion	Ref.	$R = \widetilde{\nu}_c^{\,V} / \nu_c^{Cr}$	Q-value (keV)
^{51}Cr^{5+}	^{51}V^{5+}	1.000015851(14)	752.14(64)
^{51}Cr^{6+}	^{51}V^{6+}	1.000015827(23)	751.05(108)
		Average Q-value:	751.86(55)

0.04(11) ppb per hour [101], were also neglected as the spacing between reference measurements was only 30 to 90 minutes. The frequency measurements were also analyzed with mixed charge-state pairings (i.e., ^{51}Cr^{5+} with ^{51}V^{6+}, and ^{51}Cr^{6+} with ^{51}V^{5+}), and this variation in m/q produced Q-values all within 1σ agreement. This consistency suggests that there are no m/q-dependent shifts that were unaccounted for in the analysis at the desired level of precision.

Systematic shifts in the measured cyclotron frequency can be caused by the presence of contaminant ions in the MPET [102]. Although dipole cleaning was implemented on either ^{51}Cr or ^{51}V, there was a risk of non-unity efficiency in the dipole cleaning, charge exchange with residual gas, and unidentified contamination. With a typical measurement consisting of 0-2 detected ions per cycle, possible shifts were accounted for by performing a count-class analysis [103] on all data sets. Measurements with only 1-2 detected ions after extraction from the MPET were also analyzed without count-class analysis, and the results were within 1σ agreement. Finally, a small systematic uncertainty of $\delta R_{sys}^{5+} = 4.6$ ppb and $\delta R_{sys}^{6+} = 7.4$ ppb was introduced by neglecting time-correlations [66] between neighbouring ratios. The resulting total uncertainty is thus $\delta R^{5+} = 13.6$ ppb and $\delta R^{6+} = 22.5$ ppb.

The results of all ratio measurements are shown in Figure 6.4 for the two charge states and various excitation times: 61, 66, 160, and 166 ms. The final weighted average of the ratios and the resulting Q-value are summarized in Table 6.1. The resulting Q-value from all data sets is 751.86(55) keV. Furthermore, the absolute masses of ^{51}Cr and ^{51}V were measured using ^{39}K^{4+} as a reference ion (see Table
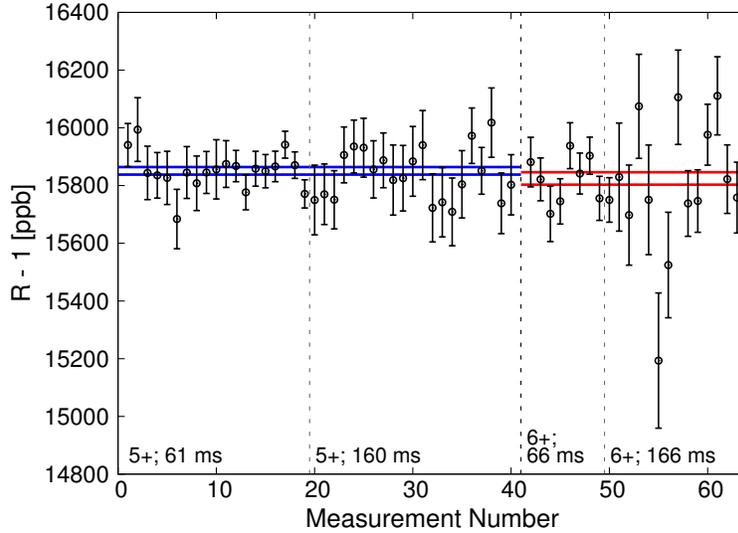
Figure 6.4: Cyclotron frequency ratios between $^{51}V^{q+}$ and $^{51}Cr^{q+}$ for different excitation times and charge states. Each point represents the ratio resulting from a single $^{51}Cr^{q+}$ resonance and its neighbouring $^{51}V^{q+}$ resonances. The blue (left) and red (right) lines show the 1σ error band for all 5+ and 6+ ratio measurements, respectively.

6.2). All results are within 1σ agreement with the AME12 values, and improve the precision in the AME12 by a factor of 1.6 and 1.8 for ^{51}Cr and ^{51}V respectively. The Q-value was also derived from the absolute mass difference and the result agrees with the direct Q-value measurement.

6.4 Summary

The first direct Q-value measurement of the $^{51}Cr(e^-, \nu_e)^{51}V$ reaction was made at TITAN. The result, $Q_{EC} = 751.86(55)$ keV, is in agreement with the reaction-based measurements summarized in the AME12, differing by 1.3σ. The neutrino energy used in the calculations of the predicted event rate for the calibration experiments at SAGE and GALLEX has thus been verified at this level. As a consequence, the accessible states of ^{71}Ge in the neutrino capture reaction will remain unchanged in the calculations, and the predicted event rate from the ^{51}Cr neutrino source has

Table 6.2: Measured cyclotron-frequency ratios and calculated mass excesses of ^{51}Cr and ^{51}V. The ratio $R(q) = \widetilde{v}_c^{\text{ref}}/v_c^{\text{ion}}$ was measured in two charge states and the average mass excess $\overline{ME}$ of the neutral atom is tabulated. The results are compared to the AME12 [97].

Ion	Ref.	$R(q=5)$	$R(q=6)$	$\overline{ME}_{\text{TITAN}}$	ME_{AME}	$\Delta_{\text{TITAN-AME}}$
^{51}Cr^{q+}	^{39}K^{4+}	1.045996804(16)	0.871654613(20)	$-51451.71(61)$	$-51451.05(88)$	$-0.66(107)$
^{51}V^{q+}	^{39}K^{4+}	1.045980222(15)	0.871640810(17)	$-52203.69(54)$	$-52203.69(88)$	$0.00(103)$

not been overestimated as a result of an erroneous ^{51}Cr electron-capture Q-value. When combined with the results of measurements on the ^{71}Ga neutrino capture reaction, these precision measurements have eliminated uncertainty in the nuclear structure that could have been responsible for the gallium anomaly, leaving other possibilities including new physics and the sterile neutrino hypothesis to explore.

Chapter 7

Conclusions and Outlook

Penning-trap mass spectrometry (PTMS) is used for the most precise measurements of atomic masses to date. With measurements on stable nuclides and fundamental particles made to within 1 part in 10^{11}, and with measurements on exotic, short-lived nuclides made to within a few parts in 10^9, PTMS is at the frontier of precision measurements. Performing precision measurements on exotic nuclides is technically challenging, but as the mass is a fundamental property unique to each nuclide, accurate and precise knowledge plays a critical role in the advancement of both theories and applications of nuclear and particle physics. The first PTMS measurement of the mass difference (Q-value) between ^{51}Cr and ^{51}V was provided as a part of this work, along with a novel optimization of charge-breeding techniques for Penning-trap mass measurements on highly charged, radioactive ions.

Neutrinos are a fundamental particle in the Standard Model, and yet long-standing anomalous results pervade the field of neutrino physics [27]. One such example is the gallium anomaly, which arose from measurements made at the solar neutrino experiments SAGE and GALLEX. Despite its successes, the theory that was used to confirm the solar neutrino deficit was found to be incompatible with the results of the calibration measurements. A measurement of possible neutrino energies from the source materials that were used in the calibration was carried out by performing the first direct Q-value measurement of the $^{51}Cr(e^-, \nu_e)^{51}V$ reaction. Measurements were made with highly charged ions in the 5+ and 6+ charge states, and a Q-value of $Q_{EC} =$ 751.86(55) keV was obtained. This result verified the neu-

trino energy used in theoretical calculations at SAGE and GALLEX and was found to be in agreement with previously made reaction-based measurements. Taken together with measurements of the ^{71}Ga neutrino capture Q-value, this measurement has eliminated uncertainty in the nuclear structure that could have been responsible for the gallium anomaly.

The advantage of charge breeding prior for a Penning-trap mass measurement lies in the attainable precision of a measurement: by making use of the time-of-flight ion-cyclotron-resonance (TOF-ICR) technique, the precision scales linearly with the charge state of an ion. In order to take advantage of this potential gain, the TITAN collaboration operates the only Penning-trap at a rare isotope facility that is coupled to an electron beam ion trap (EBIT) charge breeder. This thesis has addressed the concerns raised by implementing an additional stage in beam preparation on low yields of short-lived isotopes and has provided a systematic method of optimization. This optimization will determine which charge state to use, how long the process will take, and whether or not the losses due to radioactive decay and efficiencies will be worth the precision gained for the mass measurement.

The ratio between the attainable precision for a measurement made with highly charged ions to one made without charge breeding was defined. This factor, G_{HCI}, reflects the linear increase with the charge state as well as accounts for all parameters that would affect the statistical precision of a measurement. It was found that for sufficiently high yields (i.e., able to fully compensate for radioactive decay and efficiency losses and still result in one trapped ion each measurement cycle) the full factor of q could be exploited. Otherwise, the additional losses that would occur during the charge breeding would reduce the attainable statistical precision as compared to a measurement without charge breeding. The equations and sample calculations from Chapter 4 fully determine the benefit of charge breeding for PTMS with radioactive ions.

Simulations of the charge-state evolution from CBSIM were used to explore the phase space of charge-breeding conditions and optimize G_{HCI}. The procedure for identifying the optimal electron-beam energy, electron-beam current density, charge-breeding time, and charge state was provided with an example on the exotic nuclide ^{74}Rb ($t_{1/2} = 65$ ms). It was found that the optimal electron-beam energy was for a closed-shell electronic configuration, although variations in the

electron-beam energy did not have a large influence on the maximum attainable precision. The electron-beam current density, however, was found to play a large role in obtaining the maximum precision gain. Since increasing the electron-beam current density increases the rate of interaction between ions and electrons in the beam, it effectively speeds up the charge-breeding process, reducing losses caused by radioactive decay during the charge breeding. As a result, the optimal charge-breeding time was found not to exceed two half-lives.

The theoretical foundations used to develop CBSIM were investigated using the TITAN EBIT. The studies focused on the effect of changing electron-beam current density on charge breeding stable Rb ions by making systematic changes to the electron-beam current and magnetic field in the trapping region. A single testable prediction was defined, which stated that a unique charge-state distribution is produced for a unique combination of electron-beam current, magnetic field strength, and charge-breeding time. Although changes in either the electron-beam current or charge-breeding time changed the resulting charge-state distribution in a predictable fashion, no other expected trends were confirmed with this experimental setup. These results indicate that the idealistic assumption of perfect overlap between the electron beam and the ion bunch is not valid in our studies. Alignment studies revealed an offset between the electron collector assembly and the beam line axis that could have been responsible for the trends that were found to be incompatible with the theory. The electron collector assembly, the electron gun assembly, and the beam line were all realigned with the magnetic field axis, bringing the experimental conditions closer to what can be accurately described by theory. Additional tests with the enhanced charge-breeding setup have been recommended.

Once a reasonable theoretical description of the experiment has been achieved, the systematic optimization of charge breeding for PTMS with highly charged, radioactive ions can be directly applied. This optimization provides the ideal charge-breeding conditions and reduces the amount of experimental effort required to prepare for a high-precision mass measurement. Furthermore, it provides a quantitative estimate of the benefit of charge breeding for PTMS by accounting for all relevant variables in the determination of the attainable precision. This work can be applied to all future mass measurements at TITAN when determining whether or not charge breeding is advantageous for a high-precision mass measurement.

Bibliography

[1] E. Haseltine. The 11 Greatest Unanswered Questions of Physics. *Discover*. 1 February 2002. Print. → pages 1

[2] Y. Blumenfeld, T. Nilsson, and P. Van Duppen. Facilities and methods for radioactive ion beam production. *Physica Scripta*, T152:014023, 2013. → pages 1

[3] K. Blaum, J. Dilling, and W. Nörtershäuser. Precision atomic physics techniques for nuclear physics with radioactive beams. *Physica Scripta*, T152:014017, 2013. → pages 1, 11, 75

[4] J. Dilling, P. Bricault, M. Smith, and H.-J. Kluge. The proposed TITAN facility at ISAC for very precise mass measurements on highly charged short-lived isotopes. *Nuclear Instruments and Methods B*, 204:492 – 496, 2003. → pages 2, 78

[5] J. Dilling and R. Baartman, et al. Mass measurements on highly charged radioactive ions, a new approach to high precision with TITAN. *International Journal of Mass Spectrometry.*, 251:198 – 203, 2006. → pages 2, 25, 29

[6] J. Dilling, I. Tanihata, and D. Frekers. Electron capture branching ratios for the odd-odd intermediate nuclei in double-beta decay using the TITAN ion trap facility. *Canadian Journal of Physics*, 85:57–75, 2007. → pages 2, 25

[7] A. Lennarz and T. Brunner, et al. Electron-capture branching ratio measurements of odd-odd intermediate nuclei in double-beta decay at the TITAN facility. *Hyperfine Interactions*, 255:157–164, 2014. → pages 2, 25

[8] D. Lunney, J. M. Pearson, and C. Thibault. Recent trends in the determination of nuclear masses. *Review of Modern Physics*, 75: 1021–1082, 2003. → pages 2

[9] K. Blaum. High-accuracy mass spectrometry with stored ions. *Physics Reports*, 425:1 – 78, 2006. → pages 2, 10, 75

[10] J. K. Thompson, S. Rainville, and D. E. Pritchard. Cyclotron frequency shifts arising from polarization forces. *Nature*, 430:58–61, 2004. → pages 2, 11

[11] M. Mukherjee and D. Beck, et al. ISOLTRAP: An on-line Penning trap for mass spectrometry on short-lived nuclides. *The European Physical Journal A*, 35:1–29, 2008. → pages 2

[12] S. Schwarz and G. Bollen, et al. The low-energy-beam and ion-trap facility at NSCL/MSU. *Nuclear Instruments and Methods in Physics Research Section B: Beam Interactions with Materials and Atoms*, 204:507 – 511, 2003. → pages 2

[13] M. Redshaw and B. R. Barquest, et al. Technical developments for an upgrade of the LEBIT Penning trap mass spectrometry facility for rare isotopes. *Hyperfine Interactions*, 199:241–249, 2011. → pages 2, 3

[14] T. Eronen and V.S. Kolhinen, et al. JYFLTRAP: a Penning trap for precision mass spectroscopy and isobaric purification. *The European Physical Journal A*, 48:1–21, 2012. → pages 2

[15] G. Sikler and D. Ackermann, et al. First on-line test of SHIPTRAP. *Nuclear Instruments and Methods in Physics Research Section B: Beam Interactions with Materials and Atoms*, 204:482 – 486, 2003. → pages 2

[16] J. Ketelaer and J. Krämer, et al. TRIGA-SPEC: A setup for mass spectrometry and laser spectroscopy at the research reactor TRIGA Mainz. *Nuclear Instruments and Methods in Physics Research Section A: Accelerators, Spectrometers, Detectors and Associated Equipment*, 594: 162 – 177, 2008. → pages 2

[17] G. Bollen. Mass measurements of short-lived nuclides with ion traps. *Nuclear Physics A*, 693:3 – 18, 2001. → pages 2, 12, 30

[18] F. Wenander. Charge breeding techniques. *Nuclear Physics A*, 746:40 – 46, 2004. → pages 3

[19] M. W. Froese. The TITAN Electron Beam Ion Trap: Assembly, Characterization, and First Tests. Master thesis, University of Manitoba, 2006. → pages 3, 20, 27

[20] A. Lapierre and M. Brodeur, et al. The TITAN EBIT charge breeder for mass measurements on highly charged short-lived isotopes – First online operation. *Nuclear Instruments and Methods A*, 624:54 – 64, 2010. → pages 3, 25, 27

[21] S. Ettenauer and M. C. Simon, et al. First Use of High Charge States for Mass Measurements of Short-Lived Nuclides in a Penning Trap. *Physical Review Letters*, 107:272501, 2011. → pages 4, 27, 29, 49

[22] F. Herfurth and A. Kellerbauer, et al. Accurate mass measurements of very short-lived nuclei. *The European Physical Journal A - Hadrons and Nuclei*, 15:17–20, 2002. → pages 4

[23] A. Kellerbauer and G. Audi, et al. Direct Mass Measurements on the Superallowed Emitter ^{74}Rb and Its Daughter ^{74}Kr: Isospin-Symmetry-Breaking Correction for Standard-Model Tests. *Physical Review Letters*, 93:072502, 2004. → pages

[24] A. Kellerbauer and G. Audi, et al. High-precision masses of neutron-deficient rubidium isotopes using a Penning trap mass spectrometer. *Physical Review C*, 76:045504, 2007. → pages 4, 49

[25] V. V. Simon and T. Brunner, et al. Penning-trap mass spectrometry of highly charged, neutron-rich Rb and Sr isotopes in the vicinity of $A \approx 100$. *Physical Review C*, 85:064308, 2012. → pages 4, 27

[26] T. D. Macdonald and B. E. Schultz, et al. Precision penning-trap measurement to investigate the role of the ^{51}Cr$(e^-, \nu_e)^{51}$V Q-value in the gallium anomaly. *Physical Review C*, CK10395. Accepted for Publication in April 2014. → pages 4, 75

[27] K. N. Abazajian and M. A. Acero, et al. Light Sterile Neutrinos: A White Paper. *arxiv.org* arXiv:1204.5379 [hep-ph], 2012. → pages 4, 76, 77, 85

[28] The nobel prize in physics 1989. *Nobelprize.org*. Nobel Media AB 2013. http://www.nobelprize.org/nobel_prizes/physics/laureates/1989/, Web: 2 Apr 2014. → pages 6

[29] K. Blaum, Yu. N. Novikov, and G. Werth. Penning traps as a versatile tool for precise experiments in fundamental physics. *Contemporary Physics*, 51:149–175, 2010. → pages 6, 7, 10

[30] G. Werth. Ion Traps as Frequency Standards. *IEEE Transactions on Instrumentation and Measurement*, 34:238–242, June 1985. → pages 6

[31] S. A. Diddams, J. C. Bergquist, S. R. Jefferts, and C. W. Oates. Standards of Time and Frequency at the Outset of the 21st Century. *Science*, 306: 1318–1324, 2004. → pages 6

[32] D. Hanneke, S. Fogwell, and G. Gabrielse. New Measurement of the Electron Magnetic Moment and the Fine Structure Constant. *Physical Review Letters*, 100:120801, 2008. → pages 6

[33] S. Sturm and F. Köhler, et al. High-precision measurement of the atomic mass of the electron. *Nature*, 506:467 – 470, 2014. → pages 6

[34] W. Paul. Electromagnetic traps for charged and neutral particles. *Reviews of Modern Physics*, 62:531–540, 1990. → pages 7

[35] M. J. Smith. A Square-Wave-Driven Radiofrequency Quadrupole Cooler and Buncher for TITAN. Master thesis, University of British Columbia, 2005. → pages 8

[36] F. Herfurth. Segmented linear RFQ traps for nuclear physics. *Nuclear Instruments and Methods in Physics Research Section B: Beam Interactions with Materials and Atoms*, 204:587 – 591, 2003. → pages 8

[37] T. Brunner and M. J. Smith, et al. TITAN's digital RFQ ion beam cooler and buncher, operation and performance. *Nuclear Instruments and Methods in Physics Research Section A: Accelerators, Spectrometers, Detectors and Associated Equipment*, 676:32 – 43, 2012. → pages 8, 25

[38] M. Brodeur. First direct mass measurement of the two and four neutron halos ^{6}He and ^{8}He using the TITAN Penning trap mass spectrometer. Doctoral thesis, University of British Columbia, 2010. → pages 9, 11, 14

[39] L. S. Brown and G. Gabrielse. Geonium theory: Physics of a single electron or ion in a Penning trap. *Reviews of Modern Physics*, 58:233–311, 1986. → pages 9, 10, 11

[40] G. Gräff, H. Kalinowsky, and J. Traut. A direct determination of the proton electron mass ratio. *Zeitschrift für Physik A Atoms and Nuclei*, 297:35–39, 1980. → pages 10

[41] R. Ringle and G. Bollen, et al. A "Lorentz" steerer for ion injection into a Penning trap. *International Journal of Mass Spectrometry*, 263:38 – 44, 2007. → pages 10

[42] M. König and G. Bollen, et al. Quadrupole excitation of stored ion motion at the true cyclotron frequency. *International Journal of Mass Spectrometry*, 142:95 – 116, 1995. → pages 11, 12, 29, 79

[43] M. B. Comisarow and A. G. Marshall. Fourier transform ion cyclotron resonance spectroscopy. *Chemical Physics Letters*, 25:282 – 283, 1974. → pages 11

[44] C. Weber and K. Blaum, et al. FT-ICR: A non-destructive detection for on-line mass measurements at SHIPTRAP. In *The 4th International Conference on Exotic Nuclei and Atomic Masses*, pages 65–66. Springer Berlin Heidelberg, 2005. → pages 11

[45] F. J. Currell. Electron Beam Ion Traps and their use in the Study of Highly Charged Ions. In *The Physics of Multiply and Highly Charged Ions*, volume 1, chapter 2. Springer, 2003. → pages 13

[46] M. A. Levine and R. E. Marrs, et al. The use of an electron beam ion trap in the study of highly charged ions. *Nuclear Instruments and Methods in Physics Research Section B: Beam Interactions with Materials and Atoms*, 43:431 – 440, 1989. → pages 15

[47] G. V. Brown and C. Beilmann, et al. Studies of highly charged iron ions using electron beam ion traps for interpreting astrophysical spectra. *Physica Scripta*, 2013:014001, 2013. → pages

[48] A. Lennarz and A. Grossheim, et al. In-trap spectroscopy of charge-bred radioactive ions. *Physical Review Letters*. Submitted April 2014. → pages

[49] K. G. Leach and A. Grossheim, et al. In-trap decay spectroscopy with the titan facility at triumf. *Nuclear Instruments and Methods in Physics Research Section A: Accelerators, Spectrometers, Detectors and Associated Equipment*. in preparation April 2014. → pages 15

[50] S. Fritzsche, Th. Stöhlker, and A. Surzhykov. 16th international conference on the physics of highly charged ions. *Physica Scripta*, 2013:010301, 2013. → pages 15

[51] F. Currell and G. Fussmann. Physics of electron beam ion traps and sources. *IEEE Transactions on Plasma Science*, 33:1763–1777, Dec 2005. → pages 15, 16, 19

[52] R. K. Janev, L. P. Presnyakov, and V. P.. Shevelko. *Physics of Highly Charged Ions*, volume 13 of *Springer Series in Electrophysics*. Springer Berlin Heidelberg, 1985. → pages 15

[53] W. Lotz. An empirical formula for the electron-impact ionization cross-section. *Zeitschrift für Physik*, 206:205–211, 1967. → pages 15, 31

[54] R. Eisberg and R. Resnick. *Quantum Physics of Atoms, Molecules, Solids, Nuclei, and Particles*, chapter 11. Wiley, 2nd edition, 1985. → pages 18

[55] L. Brillouin. A Theorem of Larmor and Its Importance for Electrons in Magnetic Fields. *Physical Review*, 67:260–266, 1945. → pages 19

[56] G. Herrmann. Optical Theory of Thermal Velocity Effects in Cylindrical Electron Beams. *Journal of Applied Physics*, 29:127–136, 1958. → pages 19

[57] R. Klawitter (Private Communication, 2014). → pages 20

[58] M. Dombsky and D. Bishop, et al. Commissioning and initial operation of a radioactive beam ion source at ISAC. *Review of Scientific Instruments*, 71:978–980, 2000. → pages 23

[59] P. Van Duppen. Isotope Separation On Line and Post Acceleration. In *The Euroschool Lectures on Physics with Exotic Beams, Vol. II*, volume 700 of *Lecture Notes in Physics*, pages 37–77. Springer Berlin Heidelberg, 2006. → pages 23

[60] J. Lassen and P. Bricault, et al. Solid-State Laser, Resonant Ionization Laser Ion Source (Rilis) and Laser Beam Transport at Radioactive Ion Beam Facilities. *AIP Conference Proceedings*, 1099:769–773, 2009. → pages 23

[61] P. Bricault and F. Ames, et al. An overview on TRIUMF's developments on ion source for radioactive beams (invited). *Review of Scientific Instruments.*, 79:02A908, 2008. → pages 23, 78

[62] S. Raeder and H. Heggen, et al. An ion guide laser ion source for isobar-suppressed rare isotope beams. *Review of Scientific Instruments*, 85: 033309, 2014. → pages 23

[63] M. Brodeur and V. L. Ryjkov, et al. Verifying the accuracy of the TITAN Penning-trap mass spectrometer. *International Journal of Mass Spectrometry*, 310:20 – 31, 2012. → pages 25, 29, 75, 79, 80

[64] M. C. Simon and J. C. Bale, et al. The on-line charge breeding program at TRIUMF's Ion Trap For Atomic and Nuclear Science for precision mass measurements. *Review of Scientific Instruments*, 83:02A912, 2012. → pages 25

[65] G. Sikler and J. R. Crespo López-Urrutia, et al. A high-current EBIT for charge-breeding of radionuclides for the TITAN spectrometer. *The European Physical Journal A - Hadrons and Nuclei*, 25:63–64, 2005. → pages 25

[66] A. T. Gallant and M. Brodeur, et al. Highly charged ions in Penning traps: A new tool for resolving low-lying isomeric states. *Physical Review C*, 85: 044311, 2012. → pages 27, 81

[67] D. Frekers and M. C. Simon, et al. Penning-trap Q-value determination of the ^{71}Ga$(v,e^-)^{71}$Ge reaction using threshold charge breeding of on-line produced isotopes. *Physics Letters B*, 722:233 – 237, 2013. → pages 27, 29, 35, 76

[68] T. Brunner and A. R. Mueller, et al. A large Bradbury Nielsen ion gate with flexible wire spacing based on photo-etched stainless steel grids and its characterization applying symmetric and asymmetric potentials. *International Journal of Mass Spectrometry*, 309:97 – 103, 2012. → pages 28

[69] W. R. Plaß, T. Dickel, and C. Scheidenberger. Multiple-reflection time-of-flight mass spectrometry. *International Journal of Mass Spectrometry*, 349350:134 – 144, 2013. → pages 29

[70] V. L. Ryjkov and L.. Blomeley, et al. TITAN project status report and a proposal for a new cooling method of highly charged ions. *The European Physical Journal A - Hadrons and Nuclei*, 25:53–56, 2005. → pages 29

[71] B. E. Schultz and U. Chowdhury, et al. Cooling of highly-charged, short-lived ions for precision mass spectrometry at TRIUMF's Ion Trap for Atomic and Nuclear Science. *Physica Scripta*, 2013:014097, 2013. → pages 29

[72] M. Brodeur and T. Brunner, et al. First Direct Mass Measurement of the Two-Neutron Halo Nucleus ^{6}He and Improved Mass for the Four-Neutron Halo ^{8}He. *Physical Review Letters*, 108:052504, 2012. → pages 29

[73] M. Smith and M. Brodeur, et al. First Penning-Trap Mass Measurement of the Exotic Halo Nucleus ^{11}Li. *Physical Review Letters*, 101:202501, 2008. → pages 29

[74] R. Ringle and M. Brodeur, et al. High-precision Penning trap mass measurements of ^{9,10}Be and the one-neutron halo nuclide ^{11}Be. *Physics Letters B*, 675:170 – 174, 2009. → pages 29

[75] Sz. Nagy, K. Blaum, and R. Schuch. Highly-charged ions and high-resolution mass spectrometry in a Penning trap. In *Trapped Charged Particles and Fundamental Interactions*, volume 749 of *Lecture Notes in Physics*, pages 1–36. Springer Berlin Heidelberg, 2008. → pages 30

[76] R Becker, O Kester, and Th Stoehlker. Simulation of charge breeding for trapped ions. *Journal of Physics: Conference Series*, 58:443, 2007. → pages 31, 35

[77] G. C. Rodrigues and P. Indelicato, et al. Systematic calculation of total atomic energies of ground state configurations. *Atomic Data and Nuclear Data Tables*, 86:117 – 233, 2004. → pages 35, 80

[78] M. C. Simon and T. D. Macdonald, et al. Charge breeding rare isotopes for high precision mass measurements: challenges and opportunities. *Physica Scripta*, 2013:014098, 2013. → pages 35

[79] S. Ettenauer, M. C. Simon, T. D. Macdonald, and J. Dilling. Advances in precision, resolution, and separation techniques with radioactive, highly charged ions for Penning trap mass measurements. *International Journal of Mass Spectrometry*, 349350:74 – 80, 2013. → pages 35

[80] J. C. Hardy and I. S. Towner. Superallowed $0^+ \rightarrow 0^+$ nuclear β decays: A new survey with precision tests of the conserved vector current hypothesis and the standard model. *Physical Review C*, 79:055502, 2009. → pages 49

[81] T. D. Macdonald and S. Ettenauer. High precision mass measurements for the determination of 74Rb's Q-value. *TITAN EEC Proposal*, 2013. → pages 49, 50

[82] F. J. Currell. The physics of electron beam ion traps. In *Trapping Highly Charged Ions: Fundamentals and Applications*, chapter 1. Nova Science Publishers, Inc. New York, 2001. → pages 54, 69

[83] G. Savard and F. Buchinger, et al. *Q* Value of the Superallowed Decay of ^{46}V and Its Influence on V_{ud} and the Unitarity of the Cabibbo-Kobayashi-Maskawa Matrix. *Physical Review Letters.*, 95: 102501, 2005. → pages 76

[84] T. Eronen and V. Elomaa, et al. *Q* Values of the Superallowed β Emitters ^{26}Al^m, ^{42}Sc, and ^{46}V and Their Impact on V_{ud} and the Unitarity of the Cabibbo-Kobayashi-Maskawa Matrix. *Physical Review Letters*, 97: 232501, 2006. → pages

[85] T. Eronen and V.-V. Elomaa, et al. Q_{EC} Values of the Superallowed β Emitters ^{50}Mn and ^{54}Co. *Physical Review Letters*, 100:132502, 2008. → pages

[86] S. Eliseev and Ch. Böhm, et al. Direct mass measurements of ^{194}Hg and ^{194}Au: A new route to the neutrino mass determination. *Physics Letters B*, 693:426 – 429, 2010. → pages 76

[87] D. L. Lincoln and J. D. Holt, et al. First Direct Double-β Decay *Q*-Value Measurement of ^{82}Se in Support of Understanding the Nature of the Neutrino. *Physical Review Letters*, 110:012501, 2013. → pages 76

[88] C. Droese and K. Blaum, et al. Probing the nuclide ^{180}W for neutrinoless double-electron capture exploration. *Nuclear Physics A*, 875:1 – 7, 2012. → pages 76

[89] C. Diehl and K. Blaum, et al. Progress with the MPIK/UW-PTMS in Heidelberg. *Hyperfine Interactions*, 199:291–300, 2011. → pages 76

[90] S. Eliseev, Yu. N. Novikov, and K. Blaum. Penning-trap mass spectrometry and neutrino physics. *Annalen der Physik*, 525:707–719, 2013. → pages 76

[91] J. N. Bahcall. Solar neutrinos: Where we are, where we are going. *Astrophysical Journal*, 467:475–484, 1996. → pages 76, 77

[92] J. N. Bahcall. Gallium solar neutrino experiments: Absorption cross sections, neutrino spectra, and predicted event rates. *Physical Review C*, 56:3391–3409, 1997. → pages 76

[93] B. T. Cleveland and T. Daily, et al. Measurement of the Solar Electron Neutrino Flux with the Homestake Chlorine Detector. *The Astrophysical Journal*, 496:505, 1998. → pages 76

[94] W. Hampel and G. Heusser, et al. Final results of the ^{51}Cr neutrino source experiments in GALLEX. *Physics Letters B*, 420:114 – 126, 1998. → pages 76

[95] J. N. Abdurashitov and V. N. Gavrin, et al. Measurement of the solar neutrino capture rate with gallium metal. III. Results for the 2002-2007 data-taking period. *Physical Review C*, 80:015807, 2009. → pages 76

[96] D. Frekers and H. Ejiri, et al. The ^{71}Ga(^{3}He,t) reaction and the low-energy neutrino response. *Physics Letters B*, 706:134 – 138, 2011. → pages 76, 78

[97] G. Audi and M. Wang, et al. The Ame2012 atomic mass evaluation. *Chinese Physics C*, 36:1287, 2012. → pages 78, 83

[98] H. Schölermann and R. Böttger. Q-values for (p, n) reactions on ^{65}Cu and ^{51}V. *Nuclear Physics A*, 501:86 – 94, 1989. → pages 78

[99] K. Blaum and D. Beck, et al. Population inversion of nuclear states by a Penning trap mass spectrometer. *Europhysics Letters*, 67:586, 2004. → pages 78

[100] M. Wang and G. Audi, et al. The Ame2012 atomic mass evaluation. *Chinese Physics C*, 36:1603, 2012. → pages 80

[101] M. Brodeur and T. Brunner, et al. New mass measurement of ^{6}Li and ppb-level systematic studies of the Penning trap mass spectrometer TITAN. *Physical Review C*, 80:044318, 2009. → pages 81

[102] G. Bollen and H.-J. Kluge, et al. Resolution of nuclear ground and isomeric states by a Penning trap mass spectrometer. *Physical Review C*, 46:R2140–R2143, 1992. → pages 81

[103] A. Kellerbauer and K. Blaum, et al. From direct to absolute mass measurements: A study of the accuracy of ISOLTRAP. *European Physics Journal D*, 22:53–64, 2003. → pages 81